Integration of Dual-plane co-RASOR MR Imaging into Radiation Therapy Planning

INTEGRATION OF DUAL-PLANE CO-RASOR MR IMAGING INTO RADIATION THERAPY PLANNING

BY

EVAN MCNABB, M.Eng, (Electrical and Computer Engineering)

McMaster University, Hamilton, Canada

A THESIS

SUBMITTED TO THE SCHOOL OF BIOMEDICAL ENGINEERING

AND THE SCHOOL OF GRADUATE STUDIES

OF MCMASTER UNIVERSITY

IN PARTIAL FULFILMENT OF THE REQUIREMENTS

FOR THE DEGREE OF

DOCTOR OF PHILOSOPHY

Doctor of Philospophy (2018) McMaster University

(School of Biomedical Engineering) Hamilton, Ontario, Canada

TITLE:	Integration of Dual-plane co-RASOR MR Imaging into Radiation Therapy Planning
AUTHOR:	Evan McNabb M.Eng, (Electrical and Computer Engineering) McMaster University, Hamilton, Canada
SUPERVISOR:	Dr. Michael D Noseworthy
NUMBER OF PAGES:	xix, 172

Abstract

Radiation therapy has a significant role in the management of cancer patients. Computed tomography (CT) has been at the forefront of radiation therapy planning due to its widespread diagnostic use and its electron density information. Magnetic resonance (MR) imaging is another proven diagnostic modality, which can achieve superior soft tissue contrast and margin delineation, relative to CT. As such it has become a valuable tool for cancer diagnoses and staging.

In this study, a centre-out radial acquisition using an off-resonance reception (co-RASOR) MR sequence, sensitive to magnetic field inhomogeneity, was applied to excite a broader frequency range of spins in the vicinity of metallic seeds. The resultant images display local hyperintensities around metallic markers. These images were then reconstructed with frequency offsets to rewind these hyperintensities to the geometric centre to obtain positive contrast.

The contrast-to-noise ratio (CNR) was measured between a fiducial and its surrounding to compare Fourier and iterative reconstruction methods for undersampled co-RASOR. The motivation was to reduce the sequence acquisition time, while preserving sufficient CNR and resolution. For single slices, acquisition was 2.8 sec and multi-slice acquisition could acquire more than 50 slices in 73 sec, by reducing the acquired data by a factor of 8. This effectively encodes acquisition to 1.4 sec/slice.

The noise present in undersampled images decreased significantly using iterative reconstruction methods, but a total variation based penalty better preserved the edges.

Further extensions to the reconstruction method applied frequency-based filters that could isolate signals from different metallic compounds. The local hyperintensities rewind using opposite signed frequency offsets for diamagnetic and paramagnetic seeds. This allowed individual visualization of a low dose rate (LDR) brachytherapy seed and a gold fiducial marker. Phantom validation showed that each seed contains its maximal CNR in opposing frequency regions. The relative difference between global and local maxima in each frequency band ranged from $1.19 - 3.73$, and a single cut-off frequency was successfully applied for each acquisition plane.

Image guidance systems rely on the position of these fiducial markers to compare daily setup images with CT and MR simulations. Phantom experiments and porcine tissue samples were used to assess the minimum separation of fiducials, geometric accuracy, and random errors associated with using the co-RASOR sequence. co-RASOR images were able to resolve fiducials separated by 0.5 - 1 cm, depending on image resolution. No systematic biases were observed by comparing co-RASOR to CT using rigid body registrations. The standard deviation of the systematic errors were <0.5 mm between MR and CT registrations, and <0.4 mm between MR scans without CT. These values are smaller than the current total systematic uncertainties, which should be limited to <3 mm.

The methods presented here can aid in understanding the trade-offs between acquisition speed and signal properties, differentiating cases where brachytherapy seeds are used in combination with fiducial markers for external beam boost, and aid in co-registration of multimodality imaging.

Acknowledgements

First, I would like to thank my supervisor, Dr. Michael D. Noseworthy, for giving me the guidance and support needed to complete this thesis. Without him, none of this would be possible. I have been very fortunate to have had the opportunity to join his lab and been mentored in this field by a supervisor that has supported my research directions, and pushed me to overcome each challenge along the way. My time as his student has rewarded me with knowledge, growth, and most importantly many great memories and laughs along the way.

I would also like to thank my committee members Dr. Farncombe, Dr. Sirouspour, and Dr. Wong. They have all taken time to meet with me throughout the entirety of my degree, helped me with the methodology, writing, and provided equipment that was essential for this thesis. Dr. Wong also provided clinical experience which set out the goals and direction of the work.

I would like to acknowledge my past labmates Olga Dona, Andrew Davis, Alex Weber, Aravinthan Jegatheesan, Mohammad Warsi, Saurabh Shaw, Alireza Akbari, Michael Behr, David Stillo, Catalina Charles, and current labmates Alejandro Santos, Amy Harrison, Nick Simard, Diana Harasym, and Paul Polak for their support. They have listened to my ideas (and frustrations), given me valuable advice, and made my experience at the lab an enjoyable one.

Also, I'd like to thank Norm Konyer, and the MR technologists at the IRC Cheryl Contant, Julie Lecomte, and Carol Awde who have been invaluable in helping me learn MRI and gain the experience operating the system.

Finally, I couldn't have done any of this without the support of my family and close friends. I am incredibly grateful to my parents for always encouraging me to pursue my dreams. You deserve more praise than I could ever write. Thank you.

Nomenclature

ADC	Apparent Diffusion Coefficient
bSSFP	Balanced Steady State Free Precession
CNR	Contrast-to-Noise Ratio
co-RASOR	Centre-Out Radial Sampling with Off-Resonance Reception
CT	Computed Tomography
CTV	Clinical Target Volume
DCE	Dynamic Contrast Enhanced
DWI	Diffusion Weighted Imaging
EBRT	External Beam Radiation Therapy
EPI	Echo Planar Imaging
FOV	Field of View
FRE	Fiducial Registration Error
GFM	Gold Fiducial Marker

GTV	Gross Tumour Volume
IGRT	Image Guided Radiation Therapy
IMRT	Intensity Modulated Radiation Therapy
LDR	Low Dose Rate
LINAC	Linear Accelerator
MR	Magnetic Resonance
NUFFT	Non-uniform Fast Fourier Transform
PSF	Point Spread Function
PTV	Planning Target Volume
RF	Radiofrequency
ROC	Receiver Operating Characteristic
ROI	Region of Interest
SNR	Signal-to-noise Ratio
SPGR	Spoiled Gradient Recalled
T_1	Spin-Lattice Time Constant
T_2	Spin-spin Time Constant
TE	Echo Time
TGV	Total Generalized Variation

TR	Repetition Time
TRE	Target Registration Error
TV	Total Variation

Contents

List of Tables

List of Figures

Chapter 1

Introduction

Recently, magnetic resonance imaging (MRI) has been finding more use in radiation therapy planning. Its role is mainly secondary to computed tomography (CT). However, more institutions are attempting to contour organs with MR and use CT for its electron density information, and trials are underway for MR-only radiation therapy planning [1]. The use of bony landmarks is challenging in MR, and information-based metrics for image registration are not based on physical locations. The goal of this thesis study was to explore a dedicated pulse sequence to localize implanted fiducial markers using an undersampling acquisition strategy, differentiate between brachytherapy seeds and gold seed fiducial markers with a single MR sequence, and finally, assess the systematic and random uncertainties of MR to CT registration.

In this introduction chapter, a brief review is given in order to introduce concepts of adenocarcinoma, radiation therapy, external radiation therapy systems, and the role of MRI as a diagnostic and therapeutic aid to conventional CT planning. Chapter 2 discusses MRI physics, the implementation details and artifacts of radial acquisition, which were used in each chapter within the body of the thesis. Chapter 3 discusses

the reasons in favour of expanding the current role of MRI in radiation therapy, how the body of the thesis can help address some of the current issues and outlines the objectives and hypothesis of the following research studies. The research studies undertaken in this thesis are chapter 4, "Fiducial Localization using Undersampled co-RASOR MR Imaging", chapter 5, "Differentiating Platinum Coated Brachytherapy Seeds and Gold Fiducial Markers with Varying Off-Resonant Frequency Offsets", and chapter 6, "Resolution and Registration in Dual-Plane co-RASOR". These chapters first outline the context of the paper, the contributions of each author, and finally the study itself. Chapter 7 provides a summary of the major findings of the research, as well as contributions, limitations, and future directions. Finally, the appendix A1 lists the published material this thesis provided, and appendix A2 outlines some specific details regarding the software and source code needed to perform simulations and image reconstructions.

1.1 Adenocarcinoma and Treatment Options

Adenocarcinomas of the lung and bronchus, breast, prostate, and colorectal region account for half of all new cancers in Canada [2] and it's expected that approximately 1 in 2 Canadians will develop cancer in their lifetime. After skin cancers, adenocarcinoma of the prostate is the most common type of human cancer in males in the Western world, affecting approximately one in six men; similarly, adenocarcinoma of the breast affects 1 in 4 worldwide. In Canada, incidence rates have increased significantly from 1970 – 2007; fortunately, mortality rates began to decline in 1995 and 1986 respectively for these two dominant types and the trend has continued [3].

Decreases in mortality rates have been attributed to early detection through screening [4], greater efficacy in chemo- and hormonal therapies as primary or neoadjuvant therapies [5–7], and imaging advances in monitoring tumours and developing surgical options [8–11].

Some of these decreases in prostate cancer have also been shown to correlate with advances in external beam radiation therapy (EBRT). In a retrospective study, Kupelian *et al.* performed a multivariate analysis on 467 cases of adenocarcinoma of the prostate between 1986 - 1999, and found that relapse free survival was significantly higher after 1996, and that radiation therapy year was an independent predictor of outcome, while age, race, T-staging, and androgen deprivation were not independent predictors [12].

There are a variety of treatment options involving radiation therapy for cancer; one-third of patients with breast cancer typically receive neoadjuvant radiation therapy alone and 50% will receive it as part of a combination of therapies. Additionally, 50 - 70% of rectal cancer patients, 20% of leukemia patients, most small cell lung cancer patients, 17 - 20% of non-small cell lung cancer patients, and 25 - 40% of prostate cancer patients receive radiation therapy either alone or as part of a combination of therapies [13, 14].

1.2 Radiation Therapy Treatment Planning

Radiation therapy involves two broad classes, whether the radiation is delivered externally such as in EBRT, or internally using an implanted radiation inside or adjacent to tumour cells. Treatment delivery can be either curative or palliative, or used in combination with other therapies. Additionally, the timing of radiation therapy can

be before surgery to shrink tumours, or after surgery to remove remaining cancer cells and attempt to minimize local recurrence. The choice between these paradigms is determined by many factors including cancer type, tumour size and location, the tissue's sensitivity to radiation, and factors involving the patients themselves (age, health, and contraindications of other therapies).

Conventional radiation therapy treatment planning begins with simulation, where a CT scan is acquired in order to contour three specific volumes: gross tumour volume (GTV), clinical target volume (CTV), and planning target volume (PTV). The GTV defines the area and location of the primary tumour where tumour cell density is highest. However, microscopic extent cannot be seen through imaging techniques alone. Additionally, interobserver variability exists in defining the GTV, thus a secondary CTV, with added margins, is required. Finally, to ensure that the tumour is targeted during treatment, the last volume is the PTV. This is used to account for all system uncertainties to minimize the risk of the tumour moving out of the CTV during fractional treatments, whether due to positional errors, or patient and organ movement [15]. MRI has also been used mainly in generating contrast between the tumour and normal tissue, and is primarily an aid to define the GTV [16], although with better margins, reductions in the CTV may also be feasible. Recently, there has been efforts to use MR-only radiation therapy planning [17–19], where most of the planning is performed on MRI images, and specialized sequences are used to generate pseudo- (or substitute-)CT values [20, 21]. Lastly, MRI-guided radiation therapy systems, such as MR-Linacs or MR systems with cobalt-60 sources on a gantry, provide simultaneous MR imaging and radiation treatment [22–24].

Currently, the delivery of radiation in the MeV range for curative intent is delivered using conformal strategies, combining intensity modulated radiation therapy (IMRT) and image guided radiation therapy (IGRT). In order to improve dose delivery, and also limit the dose to surrounding organs at risk, intensity modulation was designed to create high conformal dose regions by modulating the intensity of each beam through the use of multileaf collimators [25, 26]. This process uses inverse planning starting with the desired dose volume histogram and iteratively solving the beam paths and intensities [27]. The major advantage of this technique is the high roll-off of the dose, such that the dominant lesions can be given a higher dosage compared to standard 3D conformal therapy, while minimizing the potential for toxicity effects. The equipment to deliver the radiation is also the subject of research, as IMRT delivered with a fixed-field linear accelerator (LINAC) can be slow due to required physical changes in the collimator aperture. Other delivery methods to improve the treatment time include tomotherapy, which delivers radiation through a rotating fan beam, and arc therapies where the linear accelerator is placed a rotating gantry [28, 29]. Finally, for specific applications, stereotactic equipment can be used to deliver higher doses in shorter fractions through the use of immobilization and image guidance techniques, such as the Gamma Knife (Elekta, Sweden) and CyberKnife (Accuracy Incorporated, Sunnyvale, CA, USA) systems [30–32].

The image guidance systems that aid in high conformal therapies typically involve the use of cone beam CT, and orthogonal x-ray sources and detectors [33, 34]. The image guidance systems then use the planning images to create a set of digitally reconstructed radiographs that are used to register with the setup and treatment guidance images. Bony landmarks, surgical clips, and implanted metallic fiducial markers

are typically used to perform landmark registration between the two imaging sets. Fiducial registration involves inserting 3 - 6 metallic seeds under ultrasound guidance [35, 36]. Fiducial markers have the benefit of low migration, measured using interseed distances, and allow for motion tracking of the organs. This motion can surpass 3 - 5 mm during patient set up and treatment [37–39]. Fiducial based alignment can reduce setup errors to <3 mm, and outperform soft tissue based registration involving non-rigidt transformations and information based metrics. Once the fiducials are located in three-dimensional space (or backprojected from the orthogonal detectors), a rigid body transformation can be performed between the image guidance set and the planning set. At least three corresponding fiducial locations are required between pre-treatment simulated images, and treatment fraction images to solve for rigid body registration. The centre of mass in the X, Y, and Z-directions estimates the translation vector, and various methods exist to solve for the three rotational parameters [33, 40].

Radiation can also be supplied without the use of a LINAC, where radioactive material (e.g., 60-Co, 125-I, 103-Pd, 192-Ir) is placed into seeds and placed within the tumour itself, a technique known as brachytherapy. The main differences are the treatment duration and dose rate, with low-dose rate (LDR) involving a permanent seed, or a seed placed for several days before removal. Conversely, high-dose rate involves a higher radiation dose from the seed, which is inserted with a robotic arm and remains in place only for the individual treatment sessions [41].

1.3 Assessment of Cancer using MRI

1.3.1 Routine Clinical Imaging

The choice of MR imaging protocols and the multitude of sequence specific parameters require consideration on the type of cancer being assessed, the expected morphological changes, the hardware being used, as well as patient compliance. Some generalities, however, still exist among the sequences, and they are generally classified according to their contrast mechanisms. Contrast is generated by exploiting differences in tissue-dependent time constants, T_1 and T_2 (described in detail in Chapter 2). The proton density (PD) (or spin density) is always present, and MR sequences can control this weighting as well. T_1-weighted sequences tend to highlight tissues with shorter T_1 values, imaged at short echo times (TE) and repetition times (TR), and T_2-weighted sequences tend to highlight longer T_2 values, imaged at longer TE times. MR can also highlight the relative amounts of protons in water and lipids in PD-weighted imaging. As an imperfect rule, fluids tend to have longer T_1 and T_2 values.

These two time contrast mechanisms are used in the assessments of many types of cancers. For example, lower signal intensity in T_1-weighted imaging in brain cancers correspond to necrosis, whereas higher signals display areas associated with the rim of the tumour [42]. T_1-weighted imaging is also used to visualize detailed views of the anatomy, including tumour contouring in liver cancers and viewing the axilla, chest wall and anterior mediastinum in breast imaging [43, 44]. Additionally, T_2-weighted imaging is useful for differentiating normal and pathological tissues and the presence of water and edema. For example, hyperintense signals in T_2-weighted images can view edema and infiltration of brain tumours, view water-containing breast lesions,

detect tumours in the peripheral zone of the prostate [45], as well as view the total extent of tumours in head and neck, and gynecological cancers [46, 47].

1.3.2 Dynamic Contrast Enhanced MRI

Dynamic Contrast Enhanced (DCE) MRI uses exogenous contrast agents, typically low molecular weight gadolinium (Gd) chelates, to model pharmacokinetics of tumour microvasculature from serially acquired MR images. Some tumours display a doubling of the microvascular space in carcinomas compared to benign neoplasia, as well as variable sizes and incomplete lumens of the vascular tissue [48]. This increase in permeability and microvessel density is explored using contrast agents that interact with the extra vascular, extracellular space and shorten T_1 relaxation times.

DCE MRI acquisition involves serial acquisition of 3D T_1-weighted Spoiled Gradient Echo images before and after injection of a contrast medium (0.1 - 0.2 mmol/kg) at 2 - 4 mL/s, followed with a saline flush [49, 50]. 3D sequences are preferred due to a higher signal-to-noise ratio (SNR), and improved sensitivity to changes in T_1-relaxation. The spatiotemporal resolution is a competing relationship where one is typically sacrificed for the other. While no standardization exists for temporal resolution, a consensus review panel agreed it should be no longer than 10 - 15 seconds and continue for 5 - 10 minutes to characterize washout patterns [45, 51]. Improved approximations can be achieved by reducing the temporal sampling time to 4 seconds due to the kinetic models sensitivity to mismatches between arterial input and T_1 measurements [52]. Resolution requirements were also agreed upon, stating that DCE images should be 1 mm at 1.5T and ≤ 1 mm at 3T.

After acquisition, DCE images can be used to generate and display time-intensity

curves for each voxel or a region of interest (ROI). These curves can be analyzed qualitatively according to shape or semi-quantitatively using heuristic methods such as time-to-peak, enhancement slope, and washout slope [53]. Quantitative analysis utilizes compartmental modeling composed of plasma and extracellular spaces, and excretory pathways [54]. Parameters derived from these models are: K^{Trans}, which is the permeability surface area product per unit area and flux from the plasma space to the extracellular space, v_e, which is the fractional volume of the extracellular space, and v_p, the fractional plasma volume.

As an imaging technique on its own, DCE MRI has reported sensitivity and specificity values between 46 - 96% and 74 - 96% respectively in prostate analysis for tumours larger than 0.5 mL and Gleason grade ≥ 6. The sensitivity and specificity has been reported between 89 - 100% and 24 - 88% respectively for invasive breast cancer [49, 50, 55]. Receiver Operating Characteristic curves have shown that DCE imaging outperformed T2-weighted imaging with areas of 0.91 and 0.68 respectively [56, 57].

1.3.3 Diffusion Weighted Imaging

Diffusion Weighted Imaging (DWI) is the term for MR imaging sequences that exploit the attenuation of signals due to thermally driven Brownian motion of water molecules, by employing motion-sensitizing gradients. Stejskal and Tanner first described the use of bi-polar gradients [58], which can be applied with spin echoes or gradient echoes, and with a variety of gradient lobe shapes (e.g. trapezoid, sinusoid, triangular, etc.). Diffusion (i.e. motion) encoding gradients are characterized by their b-value (s/mm^2), which is a mathematical value dependent on the phase accumulation due to the gradient amplitude and duration, and its separation from the echo

time.

Brownian motion of water molecules, in the presence of diffusion encoding gradients cause irreversible phase accumulation and result in a signal attenuation that's factored by the b-value and the diffusion, D (mm^2/s). Each image is weighted exponentially by D, which can be solved using one or more b-values to produce an Apparent Diffusion Coefficient (ADC) map. Since DWI is often performed with rapid imaging techniques such as Echo Planar Imaging (EPI), reduced resolution and susceptibility artifacts obscure the true diffusion coefficient [59]. The choice of b-value can change the interpretation of ADC values. Thus, including multiple b-values provides better correlation with true ADC [60, 61]. A general consensus for the choice of b-value is still uncertain, but it is agreed that the highest value for the calculation of ADC should be in the 800 - 1000 s/mm^2 range [45].

The use of DWI is predicated on the idea that increases in cellularity in tumour regions reduces the extracellular space and restricts the motion of water. ADC values calculated from single-shot EPI experiments using a single non-zero b-value showed significant decreases between tumour ADC values and normal tissue [62]. Most importantly ADC values are significantly negatively correlated to cellularity in lymphoma, glioma, ovarian, lung, uterine, prostate, renal cell, squamous cell, breast, and meningioma cancers [63].

Chapter 2

Radial Magnetic Resonance Imaging and its Applications

Radial magnetic resonance refers to the coverage of k-space where signal readouts are projections or 'rays' through the centre of k-space. Once the original acquisition and reconstruction method[1], this technique has unique advantages compared to Cartesian imaging, and along with advances in gradient linearity and improved static magnetic field homogeneity, radial MR has found widespread use. Perhaps the largest difference is the reconstruction method; as inverse Fourier transformation can no longer be directly applied, different reconstruction methods are required, each with their own benefits, image artifacts, and computational complexities.

This chapter explores the radial MR pulse sequence, and more specifically gradient echo approaches. Various reconstruction methods presented here will be used throughout this thesis. An important benefit of radial MR is the density in the central region of k-space, which allows for data undersampling that differs from conventional

[1]Lauterbur 1973

parallel imaging techniques. The reconstruction of undersampled data is presented here under two broad categories: non-uniform fast Fourier transform (NUFFT) and iterative regularized techniques. Finally, magnetic field inhomogeneity is explored in the context of radial k-space, leading to a modified point spread function that gives rise to certain image qualities that are used as the basis for fiducial localization.

2.1 Basics of the MRI Signal

2.1.1 Nuclear Magnetic Resonance

In order to build up the MR signals used in radial pulse sequences, it is fundamental to understand the basic NMR effect for ^{1}H (or any other non-zero spin quantum number) as these nuclei intrinsically contain angular momentum, or spin, and consequently a magnetic moment, denoted as $\boldsymbol{\mu}$. When placed in an externally applied static magnetic field $\boldsymbol{B_0} = B_0\boldsymbol{z}$, the magnetic moment will align itself with $\boldsymbol{z}$ and precession of the magnetic moment occurs around the z-axis with an angular frequency of:

$$\omega_0 = \gamma B_0. \tag{2.1}$$

This fundamental property, known as Larmor precession, relates the angular momentum of the nuclei to the strength of the applied magnetic field. The proportionality constant γ is the gyromagnetic ratio and depends on fundamental properties of nuclei such as electric charge and mass, which for hydrogen is 2.67 x 10^8 rad/s/T. Larmor precession can be explained through classical mechanics of a torque acting on the magnetic moment due to the applied field, or through a quantum mechanical

description of the difference between quantized energy states matching the energy of an oscillating wave at the Larmor frequency. Both mechanisms are extensively explored in literature.

The equation of motion due to the applied static magnetic field is of great interest in setting up an NMR experiment:

$$\frac{d\boldsymbol{\mu}}{dt} = \gamma \boldsymbol{\mu} \times \boldsymbol{B}. \tag{2.2}$$

This relationship between the magnetic moment and the applied field is not used to describe the motion of a single magnetic moment, which requires a quantum mechanical description, but rather the expected value of the magnetic moment. Furthermore, it ignores the interaction between local fields and the exchange of energy with the surroundings. It's more useful when moving towards imaging ^{1}H to define the bulk magnetization $\boldsymbol{M} = \frac{1}{V}\sum_i \boldsymbol{\mu}_i$ which sums over all of the nuclear magnetic moments in a macroscopic volume. This definition is especially useful in deconstructing the bulk magnetization into components that are parallel and perpendicular to z, i.e., $M_z\boldsymbol{z}$ and $M_{xy} = M_x\boldsymbol{x} + M_y\boldsymbol{y}$. At thermal equilibrium, prior to any NMR experiment, there is a population of spins in two discrete energy states with nearly equal proportions, with a slight preference for the lower energy state. This spin excess follows a Boltzmann distribution:

$$\frac{N_{up}}{N_{down}} = e^{\Delta E/kT} \tag{2.3}$$

where the energy difference is proportional to the strength of the applied static field.

The spin excess determines the maximum amount of signal possible and can be increased with increasing field strength or reducing temperature. Prior to any external pulses, the bulk magnetization is pointing along z as $\boldsymbol{M} = M_0\boldsymbol{z}$ with a maximum possible value of M_0:

$$M_0 = \frac{\rho\gamma^2h^2B_0}{4kT}. \tag{2.4}$$

2.1.2 Excitation and Reception

With the definition of the bulk magnetization described earlier, it's typical to represent precession in Equation 2.2 with $\boldsymbol{M}$, and also to introduce the concept of a rotating frame of reference. If the laboratory frame is rotated at an angular velocity ω that matches the Larmor frequency, then $d\boldsymbol{M}/dt = 0$ and is stationary, which simplifies the analysis that follows.

In order to get an appreciable NMR signal, the transverse component M_{xy} must be nonzero which requires some energy to disturb the magnetization away from the z-axis, and is introduced by a secondary $\boldsymbol{B_1}$ magnetic field. Since the gyromagnetic ratio for ^{1}H is in the MHz range (i.e. 42.576MHz/T), the oscillating wave required to tip a component of $\boldsymbol{M}$ into the transverse plane is in the radio frequency (RF) range, and this $\boldsymbol{B_1}$ pulse is referred to as an RF-pulse. A circularly polarized RF-pulse is used as it is more efficient than a linearly polarized pulse and takes the form:

$$\boldsymbol{B_1}(t) = B_1(t)cos\omega t\boldsymbol{x} - B_1(t)sin\omega t\boldsymbol{y}. \tag{2.5}$$

In the rotating reference frame, once ω is matched to ω_0, the pulse is simply $B_1(t)\boldsymbol{x}$. This is the *resonance condition* which ensures the rotation of the magnetization vector

occurs along an axis orthogonal to z with an angular velocity of γB_1. The shape and duration of $B_1(t)$ have important consequences for imaging, but for now its use is simply to rotate the magnetization vector into the transverse plane such that a voltage will be induced in a tuned RF coil, which can then be sampled.

It is necessary to modify Equation 2.2 to incorporate the interactions protons have with the their environment so that the magnetization vector can return to its equilibrium state. Two such interactions are called the spin-lattice and spin-spin interactions. The spin-lattice interactions result from exchanges of energy from the magnetic moments into the surrounding medium in order to achieve their lowest energy states and point along the applied magnetic field. This applies to the portion of the magnetization parallel to B_0, or M_z. Spin-lattice interactions result in an increase in M_z by a time rate known as the T_1 relaxation time, which is experimentally determined and tissue dependent. Spin-spin interactions are caused by local field variations which change the local precession frequency and the amount of phase accumulation. The summation of all protons, now with local phase deviations causes a loss of phase coherence, known as dephasing. Spin-spin interactions cause an exponential decay in the transverse magnetization by a time rate known as T_2 relaxation time, and eventually reduces M_{xy} to zero. These modifications can be written mathematically into Equation 2.2 as:

$$\frac{d\boldsymbol{M}}{dt} = \gamma \boldsymbol{M} \times \boldsymbol{B} - \frac{M_{xy}}{T_2} - \frac{(M_0 - M_z)}{T_1}. \tag{2.6}$$

This modified Equation 2.6 is known as the Bloch Equation and can be divided into individual Bloch equations for each T_1 and T_2 [64]. Although they are missing higher order and diffusion terms, they represent the equations of motion of the magnetization

vector. The applied magnetic fields $\boldsymbol{B_0}$ and $\boldsymbol{B_1(t)}$ can be included to arrive at solutions that govern most pulsed NMR experiments.

Signal reception through a RF coil, due to voltage induction derived from M_{xy} magnetization, is measured after the $\boldsymbol{B_1}$-field has been applied. A basic signal model that incorporates the solutions to Equation 2.6 is:

$$S(t) = A \int_V M_{xy}(\boldsymbol{r}, 0^+) e^{-j\gamma B_0 t} e^{-t/T_2} dV \tag{2.7}$$

where the system gain A deals with the conversion of the induced electromotive force in the coil, and all other parameters. The relaxation term, and the transverse magnetization after excitation can be combined into the effective spin density for $t \geq 0^+$:

$$S(t) = \int_V \rho(\boldsymbol{r}) e^{-j\gamma B_0 t} dV. \tag{2.8}$$

2.1.3 Signal Localization

In order to perform an imaging experiment using NMR, another set of coils have to be introduced which can alter the externally applied magnetic field as a linear function in space. These are called the gradient coils and allow for $B_0\boldsymbol{z}$ to spatially vary in three orthogonal directions. Of note, the main externally applied field still points along the z-axis, and only its magnitude changes with space. With the application of gradients coils, the external magnetic field can be altered as $\boldsymbol{B_0} = B_0\boldsymbol{z} + \boldsymbol{G} \cdot \boldsymbol{r}$ and Equation 2.8 can be rewritten as:

$$S(t) = \int_V \rho(\mathbf{r}) e^{-j\gamma B_0 t} e^{-j\gamma \int_0^t \mathbf{G}(\tau)\cdot\mathbf{r} d\tau} dV. \tag{2.9}$$

While the gradient vector is a function of time and space, we typically consider the three orthogonal components separately as functions of time, each acting independently on their own axis. This expansion of the dot product into its separable Cartesian components leads to an important formalism called k-space. Specifically, k-space aims to quantify the temporal phase change which depends positionally on the precession frequency. We define the three k-space variables as:

$$k_x = \frac{\gamma}{2\pi}\int_0^t G_x(\tau)d\tau, \quad k_y = \frac{\gamma}{2\pi}\int_0^t G_y(\tau)d\tau, \quad k_z = \frac{\gamma}{2\pi}\int_0^t G_z(\tau)d\tau. \tag{2.10}$$

If we then expand Equation 2.9 with the definitions in 2.10, and also write the signal equation as functions of k instead of time (as k-space itself is a function in time), then we arrive at:

$$S(k_x, k_y, k_z) = \int_x\int_y\int_z \rho(x,y,z) e^{-j\gamma B_0 t} e^{-j2\pi k_x x} e^{-j2\pi k_y y} e^{-j2\pi k_z z} dxdydz \tag{2.11}$$

This leads to an important relationship between the received signal and the effective spin density. If Equation 2.11 is demodulated at the Larmor frequency, the first exponential term is dropped, and each spatial coordinate is encoded by a summation of complex exponential terms, weighted by the k-space variables. This integral relationship is the well known Fourier Transform, where the spatial variables are acquired in their decomposition of spatial frequencies, and Fourier synthesis is able to reconstruct the effective spin density. An MRI experiment must sample enough k-space by applying the magnetic field gradients to create a k-space trajectory. The standard

Cartesian trajectory applies the gradients in one or two axes to encode one or both of the k_y and k_z variables, followed by a temporal readout of the encoded k_x points. Repeating the experiments with different gradient amplitudes leads to further k_y and k_z encoding.

2.2 Radial MRI

As the name suggests, radial MRI acquires k-space points along radial spokes instead of along a Cartesian sampled grid, typically used in conventional MR imaging sequences. This change in the sampling scheme can be formalized beginning with Equation 2.9, where the dot product $\boldsymbol{G} \cdot \boldsymbol{r}$ was originally replaced with three orthogonal gradients G_x, G_y, and G_z. For simplicity, we can consider a 2D example where dot product in radial MRI expands to $Gxcos\theta$ and $Gysin\theta$. respectively. The azimuth angle θ here refers to the k-space domain. By also changing the spatial variables (x, y) into (r, ϕ) (i.e., $x = rcos\phi$ and $y = rsin\phi$), the radial equivalent of the received time signal can be written as:

$$S(t) = \int_{\Delta z} \int_{r} \int_{\phi} \rho(r, \phi) e^{-j\gamma B_0 t} e^{-j\gamma G r(\theta - \phi)t} r dr d\phi. \tag{2.12}$$

Here, a further simplification is assumed, as the time integral within the phase term has also been replaced with t. This is because radial MRI encodes both directions simultaneously within the readout window, so the notion of frequency and phase encoding directions no longer applies. Similarly, the k-space variables from Equation 2.10 can be replaced by the pair (k, θ), where $k = \sqrt{k_x^2 + k_y^2}$ and $\theta = tan^{-1}(k_y/k_x)$. The fundamental Fourier Integral can then be written as:

$$S(k,\theta) = \int_{\Delta z}\int_{r}\int_{\phi} \rho(r,\phi) e^{-j\gamma B_0 t} e^{-j2\pi k r(\theta-\phi)} r dr d\phi. \tag{2.13}$$

2.2.1 Pulse Sequence Design

A basic 2D Radial sequence is shown in Figure 2.1, where the modifications are along the G_x and G_y gradients. Both gradients contribute to the MR signal readout, and their amplitudes are modulated each TR-cycle by $cos\theta$ and $sin\theta$, respectively. The sequence in Figure 2.1 can traverse all of k-space by modulating θ between $[0, \pi)$, since the dephasing gradients ensure both halves of k-space are sampled in a single readout. Conversely, the sequence in Figure 2.2 can only sample a single half of k-space and requires double the amount of spokes. The benefit, however, is the echo-time can be shorter as $k = 0$ is sampled first, instead of half-way through the readout.

In order for the Fourier Transform defined in Equation 2.13 to be invertible, a sufficient number k-space points need to be sampled. The MR pulse sequence is designed to sample enough unique k-space points such that inverse transformation is possible for image reconstruction. The number of points along each readout, and the number of radial spokes, are governed by typical Nyquist sampling requirements. The sampling of k-space will lead to aliasing in the image domain if the spacing between samples along the spoke, Δk, and along the periphery between spokes, $k_{max}\Delta\theta$, are too large. The number of samples that must be acquired along each spoke, N_R, is easiest to solve. To avoid aliasing, the field of view (FOV) must be larger than the length of the object, L. This implies that FOV $\geq$ L, or $N_R\Delta x \geq$ L. Acquiring enough points to satisfy this condition is usually not a problem as the time between each readout is on the order of microseconds. The time-limiting step is the number

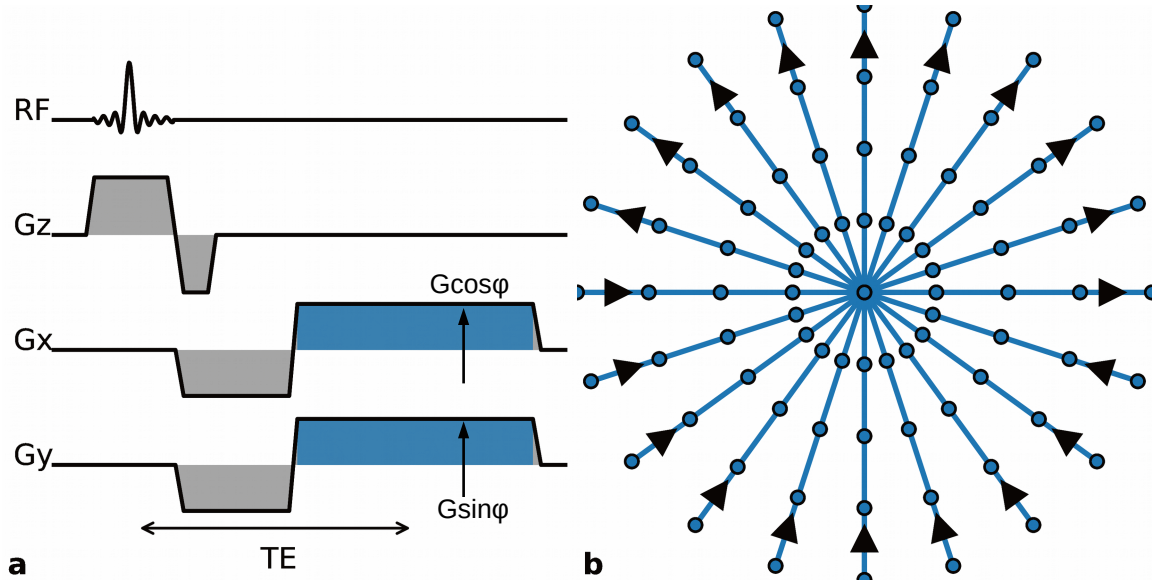

Figure 2.1: Radial Gradient Echo (GRE) pulse sequence timing diagram **(a)** and corresponding 2D k-space **(b)**. Both the G_x and G_y gradient axis are used to encode the readout (shaded in blue). For a radial sequence gradients are incremented as $G_x = G_{FE}cos\theta$ and $G_y = G_{PE}sin\theta$. The direction of the readouts are shown by the black arrows along each spoke. The presence of the dephasing gradients ensures the readout goes from the negative half to positive half of k-space.

of spokes to acquire, N_S, as this requires a TR-cycle for each spoke. The aliasing condition here is $k_{max}\Delta\theta \leq 1/L$, (i.e, the reciprocal definition of FOV $\geq$ L). For the radial GRE sequence, $N_S\Delta\theta = \pi$, which we can then solve for N_S:

$$\begin{aligned} k_{max}\Delta\theta &\leq \frac{1}{L} \\ \frac{\pi \cdot k_{max}}{N_s} &\leq \frac{1}{L} \\ N_S &\geq \pi \cdot k_{max}L. \end{aligned} \tag{2.14}$$

If sampling is done at the Nyquist limit, i.e., FOV = L, then Equation 2.14 can be reduced to $N_S \geq \frac{\pi}{2}N_R$, and radial sampling thus requires, at a minimum, 57% more

spokes than Cartesian sampling. Furthermore, that number of spokes increases by a factor of 2 if centre-out readouts are used in order to traverse the other half of k-space.

Once the number of points and spokes have been determined, the following MR sequence parameters can be solved by considering Fourier conjugate variables. For example, it's typical to start with the desired imaging parameters FOV and spatial resolution Δx. The total imaging extent determines the spacing of k-space as FOV $= 1/\Delta k$; similarly, the image resolution determines the total extent of k-space as $2k_{max} = 1/\Delta x$. The gradients themselves encode k-space, and Equation 2.10 can be used to solve for gradient amplitudes by knowing the maximum k-space values:

$$\frac{\gamma}{2\pi} N_R G \Delta t = k_{max} \tag{2.15}$$

The choice of sampling time, Δt, involves considerations into the acquisition time, noise, and expected chemical shifts. Faster imaging times can be achieved by sampling quicker, but this increases the amount of noise as the receiver bandwidth must also increase. Also, the total amount of area must be preserved, so reducing Δt means the gradient amplitudes must increase proportionally. Furthermore, the sampling time defines the bandwidth per pixel, which must be large enough to reduce spatial distortions from other chemical species (e.g., lipids). The GE MR750 Discovery MRI system that was used in this thesis has a maximum gradient amplitude of 50 mT/m, and a maximum receiver bandwidth of 250 kHz, which means all design parameters must account for these hard limits. The gradient slew rate (the trapezoidal ramps before and after the gradient plateau) is also restricted to < 200 T/m/s, as the fast switching of magnetic field gradients induces electrical fields, and possibly peripheral

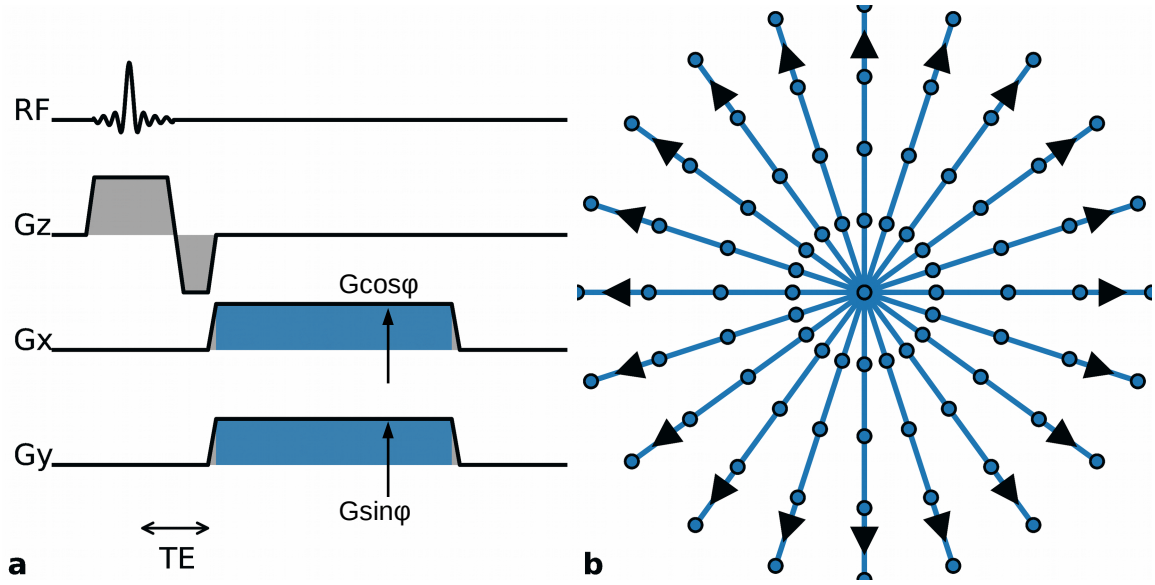

Figure 2.2: Centre-Out Radial Gradient Echo (GRE) pulse sequence timing diagram **(a)** and corresponding 2D k-space **(b)**. For a radial sequence gradients are incremented as $G_x = G_{FE}cos\theta$ and $G_y = G_{PE}sin\theta$. In this case, the absence of dephasing gradients means each readout traverses only a single half of k-space, and θ must encompass $[0, 2\pi)$.

nerve stimulation in patients. Finally, the sequence time is determined by the repetition time, TR, as each spoke requires a TR-cycle. This value is typically on the order to 5 - 500 ms, and here the system also imposes safety limits since the repeated RF-excitation deposits energy into subjects and there must be enough elapsed time for this energy to dissipate or heating (and even burning) can occur.

2.3 Radial Image Reconstruction

The final concept relating to image formation is how to apply the inverse Fourier Transform to radially acquired samples from Equation 2.13, as the standard 2D IFFT

can not be applied to non-Cartesian sampled data. Before discussing individual reconstruction techniques, it's useful to describe a property of radially acquired Fourier data, known as the Projection Slice Theorem. Recall from Equation 2.13 that the MR readout is acquired for a fixed θ in k-space:

$$\begin{aligned} s(k,\theta_{fixed}) &= \int_x \int_y \rho(x,y) e^{-j\pi k(xcos\theta + ysin\theta)} dxdy \\ &= \int_x \int_y \rho(x,y) \left(\int_\ell e^{-j2\pi k\ell} \delta(xcos\theta + ysin\theta - \ell) d\ell \right) dxdy \\ &= \int_\ell \left(\int_x \int_y \rho(x,y) \delta(xcos\theta + ysin\theta - \ell) dxdy \right) e^{-j2\pi k\ell} d\ell \\ &= \mathcal{F} \left(\int_x \int_y \rho(x,y) \delta(xcos\theta + ysin\theta - \ell) dxdy \right) \end{aligned} \tag{2.16}$$

stating that a readout through the centre of k-space at a fixed angle is equivalent to a 1D Fourier Transform of the projection of $\rho(x,y)$ along all parallel lines normal to θ. The consequence of this is that there is a direct relationship between the reconstruction methods for parallel beam CT and radial MRI, namely that the backprojection methods can be used to reconstruct the object spin density given a set of 1D Fourier encoded projections.

2.3.1 Projection Reconstruction

The simplest reconstruction method is to assume that all sets of lines that make up projections $g(\ell,\theta)$ (i.e., 1D IFFT of a radial spoke) contribute equally to the projection value at each distance ℓ. All points along this line are set to the value of $g(\ell,\theta)$ for each θ. Then, by rotating the angle and backprojecting each of the projections, an object can be formed, as shown in Figure 2.3a. The error in this

assumption is that all points in the image space are assigned a value, even if they did not contribute to the original projection, which results in significant blurring. To overcome this issue, the projection slice theorem is applied, understanding there must be a weighting component to the Fourier data prior to reconstruction:

$$\begin{aligned}\hat{\rho}(x,y) &= \mathcal{F}^{-1}\left(s(k,\theta)\right) \\ &= \int_0^{2\pi}\int_k s(k,\theta)e^{j2\pi k(xcos\theta+ysin\theta)}kdkd\theta \\ &= \int_0^{\pi}\int_\theta |k|\cdot s(k,\theta)e^{j2\pi k(xcos\theta+ysin\theta)}kdkd\theta \\ &= \int_0^{\pi}\left[\int_k |k|\cdot s(k,\theta)e^{j2\pi k\ell}dk\right]_{\ell=xcos\theta+ysin\theta}\end{aligned} \tag{2.17}$$

where it is readily seen that each Fourier line is modulated by $|k|$ prior to the back-projection along all parallel lines. This filter is known as the Ram-Lak filter, and the process itself is called filtered backprojection. However, since the value of $|k|$ contains a discontinuity at $k = 0$, a modified version exists where a window is applied that tapers the filter. The end result, however, is that each projection is convolved with the inverse FT of the filter prior to backprojection, and lines can now take on negative values helping to shape the object better, as shown in Figure 2.3b. Alternatively, one can think of weighting each k-space component such that the higher spatial frequencies are weighted higher than the lower spatial frequencies, so image details due to blurring are not lost. However, the expense of reducing this blurring and weighing the higher spatial frequencies higher is greater noise amplification.

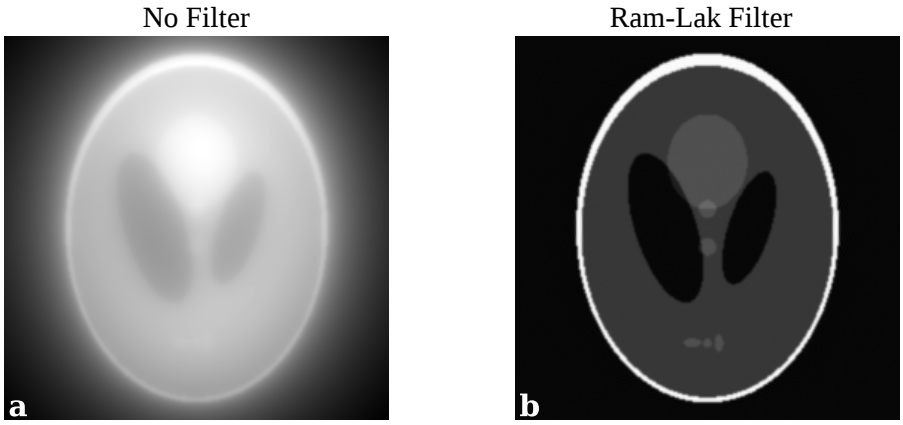

Figure 2.3: Projection reconstruction technique using simple Backprojection **(a)**, and Filtered Backprojection **(b)** with a modified Ram-Lak filter. Significant blurring is observed without the filter as the higher spatial frequencies are weighted too low, and image detail is lost.

2.3.2 Regridded Fourier Reconstruction

One concern with Equation 2.13 is that MR data is sampled discretely, and as such the continuous Fourier transform does not apply. If it did, for example, then simply sampling the data onto a Cartesian grid would be sufficient to faithfully reconstruct any object. The discrete acquisition means that k-space samples must be interpolated onto a Cartesian grid first, known as regridding. The 2D problem can be formulated as:

$$S^R(m\Delta k_x, n\Delta k_y) = \sum_i S(k_{x,i}, k_{y,i}) g_x(m\Delta k_x - k_{x,i}) g_y(n\Delta k_y - k_{y,i}) \Delta k_i \qquad (2.18)$$

where $S^R(m\Delta k_x, n\Delta k_y)$ represents the regridded signal points as a result of the convolution between the original samples, $S(k_{x,i}, k_{y,i})$, and a kernel function, $g(k)$, that has been separated into two 1D kernels for simplicity. If the original data is sampled

beyond the Nyquist limit, and $g(k)$ is a SINC function, then simple 2D IFFT inversion of the S^R samples will reconstruct an image without any aliasing. The last term, Δk_i, represents the density compensation for each point. Radially regridded data has the same density compensation as the projection reconstruction, that is $|k|$.

In practice, convolution using SINC interpolation requires the most computational time, and $g(k)$ is replaced by a compact function. The Kaiser-Bessel (KB) kernel is the most frequently applied regridding kernel [65]. The KB kernel is much more compact, typically with a width of only 4 samples, resulting in much faster convolution times (despite being a very good approximation of the SINC interpolator). The main issue with using a compact kernel however, is that aliasing can no longer be avoided. Convolution in k-space with a SINC interpolator will multiply the image domain by a RECT function, prior to replication caused from resampling. When using a KB kernel, the inverse FT of the kernel will not be compact, but rather slowly decay as a function of position. Once replication occurs from sampling, the aliasing can no longer be avoided. This can be limited by readout oversampling, where double the amount of k-space points per spoke is acquired. This method was employed for the co-RASOR sequence used in the remainder of this thesis, and each image reconstruction was truncated to display the middle of the FOV.

The major difference between regridded Fourier reconstruction and filtered backprojection is the domain where the interpolation step is performed. As just stated, regridding interpolates k-space samples, where filtered backprojection interpolates the angular backprojections in the image domain. The reconstruction times tend to be faster for regridding as the number of convolutions are reduced due to the small compact size of the KB kernel, where filtered backprojection requires convolution over

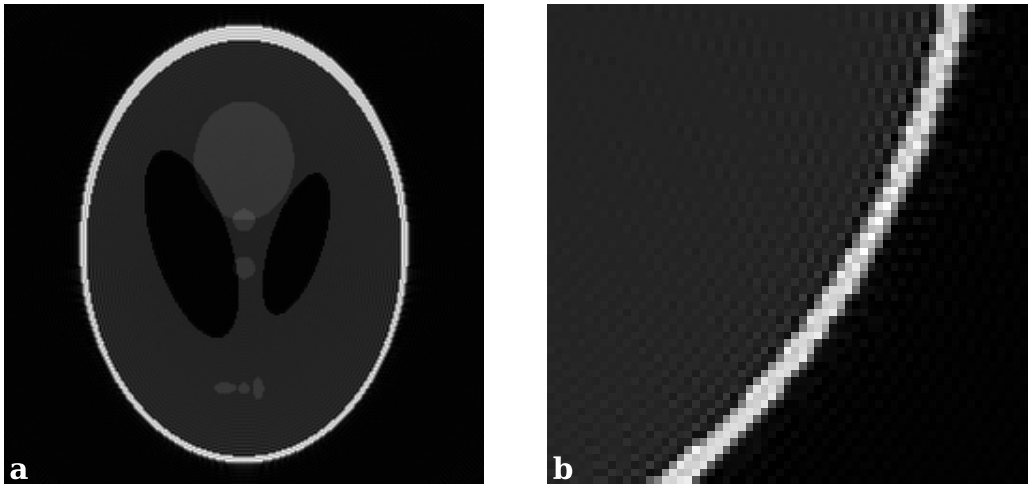

Figure 2.4: Regridded Fourier Reconstruction with Non-Uniform FFT (NUFFT) operator. The NUFFT operator uses the KB kernel with a width of $w = 8$ to perform the convolution step **(a)**. A zoomed in view reveals there is ringing artifacts along the edges, causing spatial oscillations **(b)**.

the entire image for each projection. Other differences are that filtered backprojection does not add aliasing in the same way described in the paragraph above, so long as k-space is sampled at the Nyquist limit; and, that resolution tends to be slightly lower in filtered backprojection due to the window function that's applied to taper $|k|$, described in the subsection above [59].

An example of regridded Fourier reconstruction is shown in Figure 2.4, where ringing artifacts are seen at the edge of the object and can be viewed as moderate signal oscillations along radial lines.

2.3.3 Iterative Reconstruction

An iterative reconstruction algorithm can use multiple receiver coil data and estimate the image, $I[n, m]$ and its k-space through the DFT. If F_s is a linear operator that performs the DFT and samples along the known k-space trajectories, and we have

the coil sensitivity $c_1 ..., c_M$ for M receiver coils, then the problem can be written as a stacked vector:

$$[F_s(I[m,n] \cdot c_1, \ldots, \ F_s(I[m,n] \cdot c_M]^T = \mathbf{S} \tag{2.19}$$

where $\mathbf{S}$ is a stacked vector of all readout signals for each receiver. Directly solving Equation 2.19 is generally not possible, so iterative solutions have been developed that measure the difference between the estimated k-space signals and the measured k-space signals, and attempt to minimize this residual according to:

$$\begin{aligned} \mathbf{F}(I \cdot \mathbf{c}) &= [F_s(I[m,n] \cdot c_1, \ldots, \ F_s(I[m,n] \cdot c_N]^T \\ \underset{I}{argmin} &= \frac{1}{2\lambda} \parallel \mathbf{F}(I \cdot \mathbf{c}) - \mathbf{S}\|_2^2 + \mathbf{R}. \end{aligned} \tag{2.20}$$

The conjugate gradient algorithm is typically employed to solve Equation 2.19 [66]. Regularization terms can also be added using prior information about the image in the form of a penalty function $\mathbf{R}$. One such penalty is Total Variation (TV), or extensions using variable weights and into higher order derivatives such as Total Generalized Variation (TGV), in order to smooth the areas that are oscillating. The assumption is that images are generally piecewise constant, and the best image estimate is the one that minimizes the total variation in the image domain. An example of an iterative solution using the TGV penalty is shown in Figure 2.5, where the ringing artifacts are clearly suppressed in the zoomed figure. An added benefit is that the second order TGV penalty displays better edge preservation, where there is little blurring along the edge of the phantom.

Finally, the iterative process doesn't need to minimize the difference between estimated and measured k-space samples, and can instead attempt to recover the

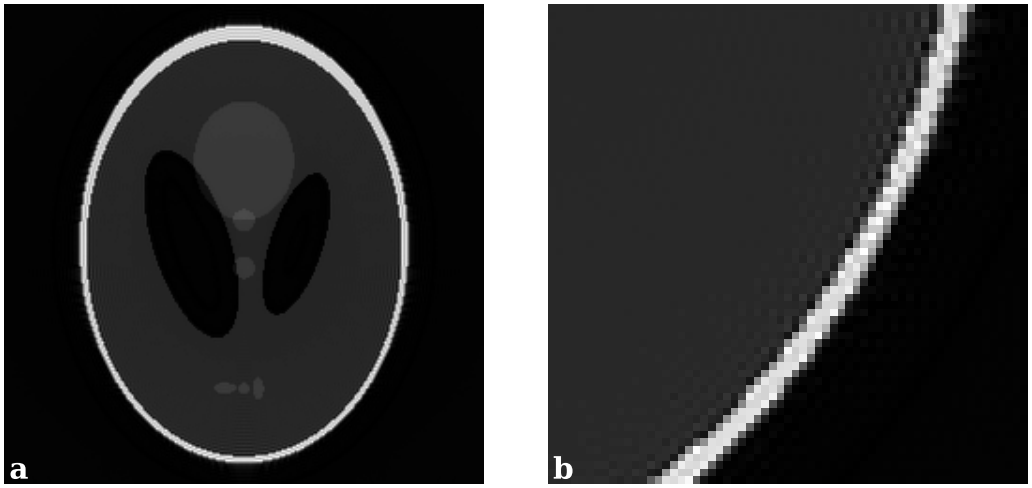

Figure 2.5: Shepp-Logan phantom iterative reconstruction using a second order Total Generalized Variation (TGV) penalty function **(a)**. A zoomed in view reveals the oscillations have been reduced, as the areas of the object are more constant **(b)**.

image by unfolding any aliasing using each coil, similar to a conventional SENSE algorithm in parallel coil MR image reconstruction. An example using the iterative conjugate gradient (CG-)SENSE algorithm is shown in Figure 2.6. CG-SENSE can maximally reduce ringing artifacts, however the result is more spatial smoothing leading to blurring. The noise suppression and blurring characteristics between these two algorithms are further explored in Chapter 4.

2.4 Field Inhomogeneity and Spatial Encoding

2.4.1 Modified Point Spread Function

Consider a spherical object of radius a, placed at the origin, with a magnetic susceptibility difference of $\Delta\chi = \chi_i - \chi_e$. The region enclosed within the sphere ($r \leq a$) does not contribute to the MR signal itself as it has no intrinsic signal. A field perturber with a constant internal susceptibility χ_i will cause a change in the local magnetic

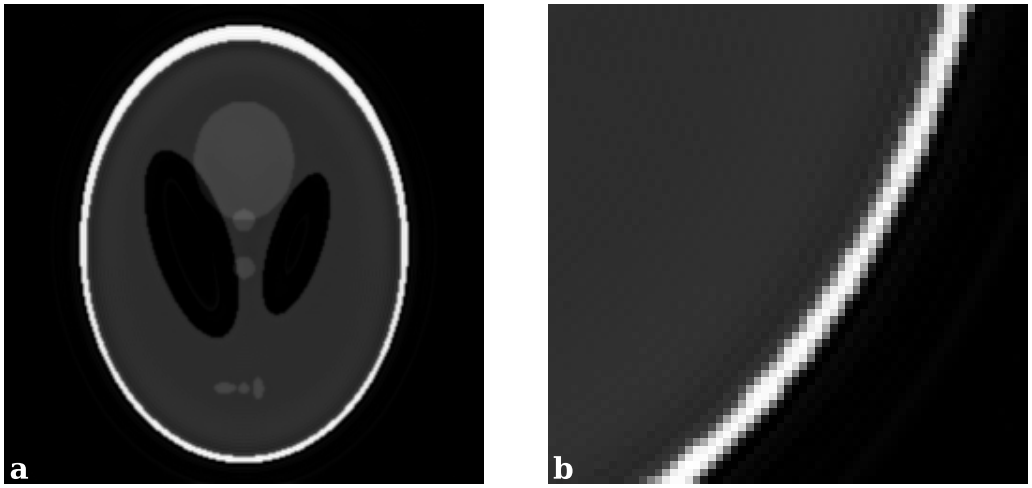

Figure 2.6: Shepp-Logan phantom iterative reconstruction using preconditioned conjugate gradient (CG-)SENSE **(a)**. The zoomed in view also reduces the oscillations, however this is at the expense of the edge of the object **(b)**.

field which can be expressed in polar coordinates as:

$$\Delta B_z(r,\phi,\theta) = \frac{\Delta\chi B_0}{3}\left(\frac{a}{r}\right)^3\left(3\cos^2\theta - 1\right) \tag{2.21}$$

where ΔB_z is dependent on the polar angle when placed parallel to B_0, and is radially symmetric about the origin traverse to B_0 (Figure 2.7). This field inhomogeneity is important in MR as a spatially varying magnetic field, $B(\mathbf{r}) = B_0 + \mathbf{G}\cdot\mathbf{r}$, is used to Fourier encode the spin density. For rectilinear k-space sampling, the point spread function (PSF) $h_{cartesian}(x,y)$ of a two-dimensional impulse $\delta(x-x_0)\delta(y-y_o)$ in the presence of field inhomogeneity is:

$$h_{cartesian}(x,y) = \delta\left(x - x_0 - \frac{\Delta B_z(x_0,y_0)}{G_x}\right)\delta(y-y_0). \tag{2.22}$$

Any resultant image, when convolved with $h_{cartesian}(x,y)$, causes the spin density to be shifted in the frequency encoding direction where the distance from the origin

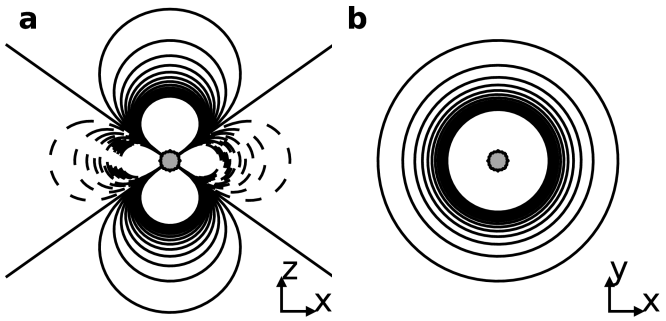

Figure 2.7: Contour lines of a 1 mm spherical field perturber (gray shaded region) placed at the origin with constant internal magnetic susceptibility ($\Delta\chi = 4000$ ppm; FOV = 32 mm). When oriented parallel to B_0 **(a)**, the field lines have both positive (solid lines) and negative (dashed lines) contour levels, dependent on the polar angle, θ. However, when oriented transverse to B_0 **(b)**, the contour levels are radially symmetric about the origin.

depends on both the field inhomogeneity and the read gradient strength, G_x [67]. The PSF for radial k-space sampling differs from the rectilinear case; its response can be considered the 2D Fourier Transform of the distortion term in the signal equation resulting in the zero-order Hankel Transform:

$$\begin{aligned} h_{radial}(r,\phi) &= \mathcal{F}^{-1}\left\{e^{-j2\pi k\Delta B_z(x_0,y_0)/G}\right\} \\ &= 2\pi\int_0^\infty e^{-j2\pi k\Delta B_z(x_0,y_0)/G} J_0(2\pi kr). \end{aligned} \tag{2.23}$$

This impulse response presents as radial blurring as h_{radial} is circularly symmetric about the origin with a radial distance proportional to $\Delta B_z(x_0, y_0)$.

2.4.2 Signal Pileups

The non-stationary PSFs can be used to estimate the MR images of a spherical field perturber. Modelled examples, using both rectilinear and radial trajectories in

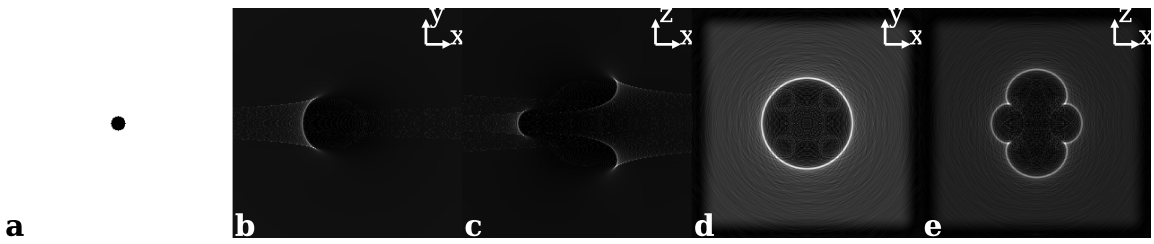

Figure 2.8: Digital phantom of a spherical object at the origin of an imaging plane ($a = 1$ mm; $\Delta\chi = 4000$ ppm; FOV = 32 mm) imaged in the absence of field inhomogeneity, i.e., $\Delta B_z = 0$ **(a)**; Rectilinear sampling ($G_x = 24$ mT/m) parallel to B_0 **(b)**; transverse to B_0 **(c)** showing signal pileup artifacts that occur only along readout direction; centre-out radial imaging over 2π rad ($G = G_z$) parallel to B_0 **(d)**; transverse to B_0 **(e)** showing signal pileups that occur in the radial direction dependent on the polar angle of ΔB_z.

varying orientations with respect to the B_0-field, are shown in Figure 2.8 where a spherical field perturber is placed in a medium of uniform spin density (asumming no relaxation processes). If a positive read gradient G_x is used for frequency encoding an entire line of k-space, the spin density left of the origin is misregistered further away as ΔB_z is increasing, however on the right side of the origin where ΔB_z is decreasing the spin density is misregistered to similar spatial locations causing signal pileups. These artifacts are dependent on orientation and occur in lines along the frequency encoding direction, with each line having unequal intensities and locations of blurring or pileups. (Fig. 2.8b-c). For centre-out radial sampling, the readout direction varies depending on the azimuth angle and uses both positive and negative gradients to sample opposite sides of k-space. The result is that the ΔB_z increases radially for both gradients and spatial misregistration causing pileups on both sides of the origin (Fig. 2.8d-e). These pileups are also dependent on the orientation of the scanning plane causing signal pileups to occur at unequal distances from the origin, but their shape corresponds to the field line patterns.

Chapter 3

Overview of Study

3.1 Rationale for MR Integration into Radiation Therapy Planning

MR integration into radiation therapy planning can be performed through multi-modality imaging, where use of CT and MRI together add complementary information. This has proven successful in, for example in prostate cancer, where CT provides electron density information and preserves geometric shapes and locations, while MRI gives superior soft tissue contrast and functional information. Alternatively, there is increased interest in MR-only simulation, where MR images are the sole modality for contouring the dominant lesions, organs at risk, and generating 'electron density' values for planning.

The primary benefit of MR integration is the enhanced delineation of both dominant lesions and organs at risk from bystandard effects of radiation. The use of

combined T2-weighted, DCE, and DWI has been reported to have improved diagnostic accuracy. For example, studies comparing the use of T2-weighted, T2w+DWI, and T2w+DWI+DCE to biopsy proven prostate cancer found the area under the ROC curve was significantly greater in regions where T2w+DWI+DCE were used. The ROC AUC values ranged from 0.89 - 0.96, with sensitivity and specificity ranging from 91.7 - 95.7% and 74 - 95.5%, respectively [68–70]. By comparison, a meta-analysis of using T2-weighted MRI only for local staging found reduced sensitivity and specificity values of 71% and 82%, respectively [16].

The secondary benefit, in the case of MR-only planning, is the elimination of uncertainties in the registration step between MR and CT, which can be systematic and up to 2 mm [71–73]. Prostate volume, for example, showed increased uncertainties and was higher when using CT due to higher interobserver variability [71, 74]. Furthermore, positional errors occur using CT defining the margins at the apex and base of the prostate, and more variability is seen determining the anterior rectal wall (up to 3 cm) [71, 75]. The consequence of these positional errors is that an additional margin is needed to be sure the CTV is covered during treatment. There are numerous methods for calculating the required margins for the PTV, though approximate margin values are between 1.3 - 2.5 times the standard deviation of the systematic errors and 0.5 - 0.7 times the standard deviation of the random errors to ensure that the 95% of the CTV is covered in 90% of a patient group [76, 77].

3.2 Hypothesis

Image guidance during treatment delivery is associated with reduced CTV margins due to the ability to track interfraction motion and deformation [78]. The improved

margins in combination with daily corrections results in improved prostate tumour control and lower late urinary toxicity scores [79]. Implanted metallic fiducial markers also serve as a surrogate for the position of an organ. These exhibit increased accuracy relative to external markers or bony landmarks, as they also describe rotational movements, which may be independent of translational movements [80]. The intermarker distance is relatively stable over the treatment length, ranging from 0.3 to 1.2 mm migrations [81–83].

In order to take advantage of image guidance in MR integrated delivery, the fiducial markers must also be visible on the MR images during simulation, whether they are used for co-registration with CT or used in MR-only simulation. Visualization is currently based on optimizing negative contrast sequences to display a signal void artifact caused by the fiducials. These artifacts are larger than the seeds themselves, and even larger still when using gradient echo imaging [16, 84]. Balancing the amount of negative contrast and size of the artifact are usually competing demands, and visualization is performed over multiple sequences. Dedicated sequences that try to balance this include 3D bSSFP sequences, which use T1/T2 contrast, and have become common for localization [17–19, 85]. However, the use of negative contrast is non-specific as signal voids can be caused by sources other than metallic seeds. Some groups have addressed this with machine learning to create unique, localized masks [85–87]. Despite these advances, even the MR-only simulation still uses a small FOV CT image for fiducial localization and differentiation between gold fiducials and brachytherapy seeds [18].

Positive contrast sequences have been developed for stronger field perturbers, such as paramagnetic brachytherapy seeds, needles, and super-paramagnetic iron oxide

particles [88]. Although they require pulse sequence modifications or new reconstruction pipelines, they are able to visualize implanted devices with highly localized positive contrast, thereby increasing specificity. One technique that addresses this problem is the centre-out radial sampling with off-resonance reception (co-RASOR) technique [89, 90]. In co-RASOR imaging, centre-out readouts use only a positive or negative gradient to encode positive and negative k-space locations respectively, to create signal pileups or hyperintensities around the objects (Figure 2.8).

We hypothesize the co-RASOR sequence can also be used for MR therapy integration to visualize gold fiducial markers. Additionally, since the radial sequence can be implemented in 2D and undersampled, this may be a quicker acquisition technique than other dedicated sequences. Furthermore, information regarding the magnetic susceptibility differences of varying seed compositions are encoded into the acquired signal, and different off-resonant frequencies can in principle rewind the hyperintensities at unique frequency offsets. The signal differentiation based on off-resonant frequencies can allow for specific visualization of different implanted devices, aiding in situations where LDR brachytherapy is used in addition to external beam radiation. Finally, as the signal pileups are approximately symmetric, the use of a single reconstruction parameter (i.e., off-resonant frequency offset) should localize to the geometric centre of the seed, which can alleviate concerns over geometric accuracy of MR localization methods.

3.3 Methods

A dual-plane co-RASOR sequence was implemented by modifying the General Electric Healthcare MRI source code of a 2D fast GRE sequence using the Environment for

Pulse Programming in C (EPIC). The sequence implements the gradient timing, as shown in Figure 2.2, using a centre-out radial sampling trajectory. The modifications remove the conventional phase encoded gradient, and apply a 2D rotation matrix between each TR-cycle to rotate the frequency encoding axis.

The implementation uses a minimum echo time, which reduces the dephasing gradient to four sampling points, compared to half the number of readout points. The gradient system timings are never perfect, and there are typically delays between the requested time and the actual gradient switching; sampling some points along a quick dephasing section ensures that the $k = 0$ echo point is sampled, which contains the bulk image contrast. Readout oversampling was performed, where the sequence overrides and doubles the receiver signal bandwidth prior to imaging. As all other parameters remain the same, the final FOV is also doubled, and limits the aliasing artifacts due to regridding to the furthest edges. The reconstructed image is then cropped to display the centre image at the nominal FOV. Finally, the dimensionless time-bandwidth product of the transmit RF pulse was increased by a factor of 2 in order to reduce the pulse duration time. This increases the $B_1(t)$ amplitude and reduces slice homogeneity, but allows for a higher transmit bandwidth which will selectively excite more off-resonant protons into the received signal, as well as reduce the echo time to avoid intravoxel dephasing. The minimum achievable time through testing was approximately 900 μs, reduced from a nominal value of 3.2 ms.

Simulations were performed in each of the research papers to test the reconstruction techniques presented. In-house software was written to create these simulated environments, as well as a general software package to read/write and filter the data, and link to reconstruction toolkits (see. Appendix A2). The simulations performed

were either spherical field perturbers, whose field inhomogeneity patterns are well described in literature, and written in Equation 2.21 in order to investigate the effects of resolution, clustering, signal dephasing, and undersampling. To simulate fiducial seeds of arbitrary lengths, a superposition of these spherical models on a high density grid at each point the seed would occupy, was applied. This approach was used to simplify the simulations, as there is generally no analytical solution to the field inhomogeneity beyond simple shapes, and helped preserve the sharp boundary along the fiducial length. Assuming each seed was an ellipse would mean an absence of sharp boundaries, which is not physically accurate. Likewise, a full numerical analysis would require intensive computation of the magnetic field at each point in space, unsuitable for the purposes of testing reconstruction methods. Our approach was validated by creating a very long fiducial relative to its diameter, and comparing to the analytical solution of an infinitely long cylinder.

Gel phantoms were constructed for the various experiments, which consisted of a 3% agar mixture into water and careful pouring into containers to avoid air bubbles. It would be impractical to remove all air bubbles, however we don't consider these to be a problem in the experiments as they typically exist only on the surface. Tissue samples were also utilized, involving a pork hock from the local supermarket, wrapped in plastic wrap, and placed in plastic containers that were selected to fit the size. This helped to ensure no motion confounding between imaging sessions.

Finally, various equipment was used in the following experiments. The imaging systems were a 3T GE Discovery MR750 (General Electric Healthcare, Milwaukee, WI), and a Siemens Biograph 16 PET/CT scanner (Siemens, Erlangen, Germany). MR signal reception was performed using a 32-channel head coil. Implanted metallic

seeds were either gold fiducial markers (IZI Medical Products, MD, USA) or LDR brachytherapy seeds (DraxImage Model LS-1, Quebec, Canada). Most of the imaging phantoms were developed in-house, with the exception of a MR-compatible Lego phantom (ONDRI, Ontario, Canada).

3.4 Experimental Design

The first study focused on three reconstruction techniques which were applied to undersampled co-RASOR data. Reconstruction is typically performed using Fourier inversion, and for the case of multiple receiver coils, a sum of squares addition is performed from the reconstructed image of each coil. The incoherent noise decreases with more coil elements, whereas undersampling artifacts present themselves as coherent noise patterns. We hypothesized that non-linear iterative reconstruction with an edge preserving penalty may reduce the coherent noise patterns while preserving the localized signal contrast. We measured the contrast-to-noise of a fiducial in different orientations with respect to the B_0-field, the FWHM area surrounding each the fiducial, and noise in the vicinity of the fiducial for three different reconstruction methods.

The second involved further evaluation of the co-RASOR reconstruction method by applying a range of frequency offsets to explore how different metallic compositions encode their magnetic field susceptibility into the received signal pileups. It was hypothesized that a paramagnetic LDR brachytherapy seed and a diamagnetic gold fiducial marker could be reconstructed individually as their signal maxima would depend on the sign of the off-resonant frequency. Numerical simulations were performed, followed by an imaging phantom study of two different seeds inserted into a

porcine tissue sample.

The third study examined how the spatial distribution of gold fiducial markers influences the observed hyperintensities, and whether the off-resonant reconstruction could localize the fiducials, even under circumstances where their signal pileups merged together. Furthermore, the geometric accuracy was assessed using a MR-compatible Lego phantom, and tissue samples with inserted seeds. We hypothesized that compared to CT, a set of target registration errors would be zero mean with an experimentally determined standard deviation that can serve as an estimate of the fiducial localization error.

Each of the following chapters are written as manuscripts that detail the implementation details of these experiments, as well as results and discussion points.

Chapter 4

Fiducial Localization using Undersampled co-RASOR MR Imaging

Evan McNabb, Raimond Wong, Michael D. Noseworthy

https://doi.org/10.1016/j.mri.2017.12.009

4.1 Context of Paper

In this study, we simulated and acquired undersampled 2D dual-plane co-RASOR images of a paramagnetic fiducial marker and measured contrast and full width half maxima in order to assess localization with different image reconstruction methods. Using a 2D sequence and undersampling the number of radial spokes will lead to increased temporal efficiency at the expense of global signal-to-noise. We hypothesized that the choice of reconstruction method, namely iterative reconstruction techniques

with a penalty function that preserves edges by strongly penalizing oscillations, will increase the local contrast-to-noise (CNR) of the marker compared to its adjacent surrounding with respect to standard non-Cartesian image reconstruction.

After implementing methodology using three reconstruction methods, we found that CNR was generally higher using CG-SENSE, followed by TGV2 and NUFFT. However, CNR is offset by the FWHM area which grows much quicker with CG-SENSE compared to the other two methods, lowering the resolution of the fiducial. An analysis of the noise showed that CG-SENSE significantly smooths the noise and resulted in more voxels being above the 50% threshold of image intensity. The edge-preserving TGV2 penalty had comparably high CNR, above the limits of detectability, and increased resolution. We concluded that as undersampling grows to levels that diminish the signal, CNR can be increased with an edge-preserving penalty without sacrificing resolution compared to other reconstruction methods.

4.2 Declaration Statement

Evan McNabb acquired the data, performed the data analysis, interpreted results, and drafted the manuscript text. Additionally, he created the manuscript figures, and tables. The contributions by Evan McNabb warranted his name as first author.

Dr. Michael Noseworthy, as corresponding author, designed this project as multi-disciplinary biomedical engineering project as part of his years of expertise in the field of Magnetic Resonance as well as developing engineering applications to serve clinical needs. He provided critical analysis of the methodology, interpretation of results, and manuscript revisions of the final article that he submitted for publication. Finally, he provided thorough guidance and helped secure funding resources.

Dr. Raimond Wong conceptualized the clinical rationale for this project based on his expertise as an interventional oncologist. He provided the clinical materials used for research, provided guidance in tailoring the engineering principles to clinical outcomes. Finally, he also secured funding resources.

This paper was submitted to *Magnetic Resonance Imaging* on November 22, 2017 and was accepted for publication without revisions December 3, 2017.

4.3 Paper

Localizing Implanted Fiducial Markers using Undersampled co-RASOR MR Imaging

Evan McNabb[a], Raimond Wong[b,c,d], Michael D. Noseworthy[a,e,f,g,*]

[a]McMaster School of Biomedical Engineering, McMaster University, Hamilton, Canada
[b]Juravinski Cancer Centre, Hamilton, Canada
[c]Department of Oncology, McMaster University, Hamilton, Canada
[d]Department of Medicine, McMaster University, Hamilton, Canada
[e]Imaging Research Centre, St. Joseph's Healthcare, Hamilton, Canada
[f]Department of Electrical and Computer Engineering, McMaster University, Hamilton, Canada
[g]Department of Radiology, McMaster University, Hamilton, Canada
[*]Corresponding author at: Department of Electrical and Computer Engineering, McMaster University, Engineering Technology Building, ETB-406, 1280 Main St. W, Hamilton, Ontario, Canada, L8S 4K1. Email: nosewor@mcmaster.ca

Abstract

The goal of this work was to use an undersampled, dual-plane centre-out radial sampling acquisition pulse sequence, with off-resonance reception, to localize fiducial markers with reduced acquisition time. Two iterative reconstruction techniques,

conjugate gradient CG-SENSE and the variational penalty Total Generalized Variation (TGV), were investigated to minimize the undersampling artifacts in off-resonant radial imaging. Simulations of a field perturber were performed at sub-millimeter resolution and reconstructed to display signal pileups that can be radially compressed towards the geometric center of the perturber for high contrast visualization, but contrast is non-recoverable as the echo time increases. A cylindrical platinum fiducial marker, placed in a phantom parallel and perpendicular to the B_0-field was imaged with a short-TE half-echo readout. Contrast-to-Noise (CNR) between the signal of the fiducial its adjacent surrounding shell and half-maximum area were used to compare reconstruction methods and undersampling factors. For single slice acquisitions centered about the fiducial, each slice can be performed in as little as 2.8 s. The total acquisition time to localize the fiducial marker in a phantom was reduced to 73 s by undersampling (R=8) 37 axial and 15 coronal slices, effectively encoding 1.4 sec/slice. The noise present in undersampled images, for both scan planes and fiducial orientations, decreased significantly using TGV and CG-SENSE reconstructions, with TGV displaying better spatial resolution from reduced half-maximum area.

Keywords: positive contrast, total generalized variation, fiducial localization, accelerated radial imaging

4.3.1 Introduction

The use of image-guided radiation therapy (IGRT) in the treatment of tumours located in areas of the body undergoing motion, has greatly increased the efficacy in dose delivery to selected target volumes [29]. Usually, bony landmarks, surgical clips or implanted metallic fiducial markers are used to co-register the treatment planning images with the images acquired during therapy. Fiducial markers have the benefit of low migration and can be used in rigid body transformations without relying on the orientation of organs with respect to bony landmarks which are subject to deformable motion [82].

The use of MR in radiation therapy planning continues to increase, due to its superior soft tissue contrast in delineating the clinical target volume (CTV), and the ability to better differentiate organs at risk [24]. Recent studies have compared the dosimetric accuracy of MR-alone plans with assigned electron density values [20, 91, 92]. Attempts have been made to define the full role of MR in radiation therapy planning, including the use of MR simulators, standardized equipment, e.g., RF coils, immobilization devices, as well as patient setup and acquisition protocols specific to planning [93, 94]. One challenge in using MRI for treatment planning is that implanted metallic fiducial markers do not produce contrast, and are visualized as hypointense signal voids with distortions along their interfaces. The lack of positive contrast has resulted in non-standardized approaches for fiducial localization and image registration. MR imaging sequences have been modified to visualize implanted devices with positive contrast due to local deviations in the magnetic field surrounding a field perturber that cause shifts in k-space [95]. Other techniques rely on the changes in precession frequency and selectively excite or suppress protons in specific

spectral regions, or, rely on the error in phase accumulation between echoes in SSFP and multi-echo acquisitions [88]. An ongoing issue visualizing interventional devices is that spatial encoding relies on a known, spatially varying magnetic field. This assumption is violated in the presence of field inhomogeneity and causes spins to be mis-registered.

One technique that addresses this problem is the centre-out radial sampling with off-resonance reception (co-RASOR) technique [89, 90]. In co-RASOR imaging, centre-out readouts use only a positive or negative gradient to encode positive and negative k-space locations respectively. The resultant spin density is symmetrically mis-registered to similar spatial locations causing signal pileups that can be radially shifted centrally by acquiring the data off-resonance, or modulating each readout with a linear phase ramp during reconstruction, so the signal pileups occur at the geometric centre of the field perturber.

Here we presents an approach for reducing the clinical scan time required for viewing fiducial markers with positive contrast. The most significant limitation in scan time is the number of unique lines in k-space that must be sampled. Typically, 3D radial imaging is acquired with both isotropic resolution and field-of-views, where the scan time is proportional to square of the number of readout points. This has the potential for temporal inefficiencies. For example, in prostate treatment planning, the FOV may need to be expanded to a range of 20-22 cm while preserving sub-millimetre resolution, consequently requiring multiple minutes to acquire. A dual-plane 2D co-RASOR sequence, previously shown to localize high-dose brachytherapy seeds with increased temporal efficiency [96], is proposed here for fiducial localization. To further reduce scan time, we exploit the advantageous properties of undersampled radial

acquisition: as the central region of k-space is oversampled, the bulk image contrast is preserved. However, due to the increased spacing in the peripheral regions of k-space, noise is present in the reconstructed image which appears as streaking artifacts along radial lines [97]. The use of undersampled acquisitions comes with a cost of reduced contrast-to-noise (CNR) which will impact the ability to localize a fiducial. Advances in reconstruction algorithms now employ regularized, iterative solutions to attenuate the incoherent noise patterns in radial reconstructions. Some regularization examples include penalizing the L2-norm, Total Variation (TV), or more recently Total Generalized Variation (TGV) which relaxes the assumptions made requiring images to be piecewise constant used in the TV penalty, while still preserving edges [98–100].

The objective of this study was to demonstrate that iterative regularized reconstruction techniques can be used to successfully denoise undersampled co-RASOR images acquired from multichannel coils that have been degraded by undersampling artifacts and intravoxel dephasing at non-zero echo times. A secondary goal is to evaluate how much undersampling can be performed in which a singular hyperintense structure is the focus.

4.3.2 Materials and methods

4.3.2.1 Simulating co-RASOR images

The demodulated MR signal at time $t' = (t - T_E)$ that is centre-out radially sampled in the presence of field inhomogeneity is:

$$S(k,\theta) = \int_0^{2\pi} r d\phi \int_0^{\infty} dr \rho(r,\phi) e^{-j2\pi k r cos(\phi-\theta)} \times e^{-j\gamma \Delta B_z(r,\phi)t} \tag{4.1}$$

The presence of $\Delta B_z(r,\phi)$ causes scaling of the k-variable in the directions parallel to the applied gradient, causing geometric distortions in the reconstructed image. Point symmetric hyperintense signal pileups around the field perturber are observed when using centre-out readouts over a 2π range. In the co-RASOR method, an off-resonant reception frequency of δf causes an additional linear phase ramp argument to be present, as $e^{-j2\pi\delta f t}$. If the image is acquired using a gradient strength G, and k is substituted as $k = \frac{\gamma}{2\pi} G t'$, then the Equation 4.1 can be rearranged as:

$$S_{CR}(k,\theta) = \int_0^{2\pi} r d\phi \int_0^{\infty} dr \rho(r,\phi) \times e^{-j\gamma(Grcos(\theta-\phi)+\Delta B_z(r,\phi)+2\pi\delta f/\gamma)t'} \times e^{-j\gamma(\Delta B_z(r,\phi)+2\pi\delta f/\gamma)T_E} \tag{4.2}$$

This signal equation can be split into the distortion of spatial encoding due to the first exponential term, and the intravoxel dephasing which occurs due to the second exponential term. The extra arguments in the first exponential resemble a Fourier

shift and since it only applies to the readout time t', it influences k and has no angular dependence on θ during the image reconstruction, and must be circularly symmetric. Setting an appropriate value of δf can radially shift the signal pileups toward the origin of their respective field perturbers.

The intravoxel dephasing term does not influence the spatial encoding or amount of shifting, but influences signal intensities. While this term can generally be neglected for UTE sequences as it disappears at $T_E = 0$, the lowest T_E in 2D imaging is determined by the length of the slice-selective RF and gradient pulses, on the order of a millisecond, and results in local shifts in k-space leading to varying phase dispersion for each voxel during reconstruction.

Two-dimensional Fourier encoded datasets were simulated by discretizing Equation 4.1 to estimate centre-out acquired data around a paramagnetic spherical fiducial marker ($a = 1$ mm) when placed in an external magnetic field of 3T. The internal and external susceptibility values are constant and the field inhomogeneity is caused by a susceptibility difference of $\Delta\chi = 4000$ ppm. Axial and coronal plane images with a FOV = 32 mm were simulated to generate sub-millimetre resolution. A total of 32 elliptical coil sensitivity profiles were simulated and the image is modulated by each unique profile resulting in 32-channel data. The total number of centre-out radial spokes was reduced, increasing the k-space azimuth angle by $\Delta\theta = R \cdot \frac{2\pi}{N}$, using undersampling factors of R = 1, 2, 4, 8, 12, and 16 from 804 centre-out projections with 256 readout points to investigate the coherent noise in the reconstructed images. Two different echo times of 0 ms and 4 ms were used to create datasets representing an ideal case with no intravoxel dephasing and a more realistic case with some elapsed time due to the slice-select gradient, with the intravoxel dephasing term present from

Equation 4.1.

4.3.2.2 Accelerated co-RASOR imaging

For isotropic resolution and FOV, 3D centre-out radial acquisitions require πN^2 unique readouts, where N is the number of readout points used in Cartesian sampling. Reducing scan time can be achieved by dual-plane 2D sampling, which requires $2\pi N \cdot N_{slices}$ readouts, where N_{slices} can be considerably lower than N in regions that do not require isotropic coverage, as well as the use of thicker slices. Additional time savings can be achieved by reducing the total number of readouts by increasing the angle between readouts. Radial trajectories oversample the centre region of k-space which results in two beneficial properties for accelerated imaging: undersampling can still adequately sample this centre region and estimate the bulk of the Fourier encoded k-space, and undersampling artifacts are most prevalent on the periphery of the image domain causing coherent noise in the form of radial streaking. The reduction in data also reduces the signal-to-noise (SNR), commonly formulated as:

$$SNR_{under} = \frac{SNR_{optimal}}{g\sqrt{R}} \tag{4.3}$$

in SENSE reconstruction, with the g-factor being a spatially dependent term proportional to the noise amplification. Similar to parallel imaging techniques which use lines through the centre of k-space to form auto-calibrated signal regions [101, 102], radial readouts always sample lines through $k = 0$ and can also be used to estimate coil sensitivity profiles without additional calibration scans.

Regularization terms can be added using prior information about the image in the form of a penalty function applied to each iteration. Such penalties should address

the structure of the noise that is expected by reconstructing radial data, and total variation or total generalized variation are two such penalties that penalize areas of the image that have strong first and second order spatial derivatives respectfully. In the case of co-RASOR data where a frequency offset is applied, the entire image domain is severely distorted with the exception of the geometric centres of the fiducial markers, which creates some violation in the assumptions of piece-wise smooth images. TGV makes less assumptions about the characteristics of the final image and may be better at preserving the well-localized hyperintense areas.

4.3.2.3 Image reconstruction

Each simulated dataset was reconstructed using three techniques: the non-uniform DFT (NUFFT) and two iterative methods using the TGV regularization penalty and conjugate gradient (CG-) SENSE, to investigate the noise reduction and edge preservation qualities. Each method was performed from software packages written in MATLAB R2014b (The Mathworks Inc, Natick, MA) to implement the NUFFT operator [103], the iterative regularized Gauss-Newton reconstruction using a first-order primal-dual algorithm and TGV regularization [99], henceforth referred to as the TGV method for the remainder of this article, and CG-SENSE [104]. The TGV penalty uses min-max optimization to determine the regularization penalty as a function of space. The regularization penalty selects the second-order spatial derivative in areas of the image that are locally smooth, and are relatively less expensive than edges, resulting in edge-preservation and a reduction in patchiness.

The latter two require coil sensitivity estimation which was performed identically prior to each iterative reconstruction method using a H1-regularization followed by

spatial smoothing [98]. All images were reconstructed to matrix sizes of 256 x 256 at $\Delta x_{sim} = 0.125$ mm. Parameter selection was done according to the methods of the two iterative software packages, where in each case, the weightings were chosen such that they reduced the residual with NUFFT when fully sampled. In this case, TGV regularization weighting was reduced to $\lambda = 2.5\text{x}10^{-1}$ and 500 iterations and CG-SENSE reduction factor was reduced to 2.0 with 15 iterations. Finally, in order to highlight the localization of the spherical fiducial marker from 2D co-RASOR imaging, an offset of $\delta f = -3.6$ kHz was chosen as the optimal frequency value to radially rewind the hyperintense signal pileups to the geometrical centre of the image in both axial and coronal planes. This optimal offset was determined empirically by selecting the the offset that maximized the central fiducial signal in the off-resonant images.

4.3.2.4 MR Phantom Imaging

Platinum seed fiducial markers (IZI Medical Products, Owings Mills, MD, USA) that are cylindrical shaped with 3 mm long axis and 1 mm diameter were placed in a 3% agarose gel phantom with the longitudinal axis parallel to the B_0-field. The phantom was constructed with a layer of gel that was allowed to cool prior to setting the fiducial marker in the centre of the container, followed by a second layer of gel. The separation of the two layers can be visually identified in all localizer images in order to aid the slice prescription containing the fiducial. MR imaging was performed using a 3T GE Discovery MR750 (General Electric Healthcare, Milwaukee, WI) with a maximum gradient strength of 50 mT/m, a slew rate of 200 T/m/s, and a 32-channel head coil. An in-house sequence was developed, modifying a 2D SSFP pulse sequence, acquiring

centre-out radial readouts over 2π rad of k-space, oversampled in the readout direction by a factor of 2. Fully sampled axial and coronal slices were acquired of the fiducial lying parallel to B_0 (TE/TR = 2.8; FOV = 16.0 cm; thickness= 3.0 mm; acquisition matrix = 256 x 804; receive bandwidth ˜ 250 Hz/pixel). Slice selection was performed with a one-cycle SINC pulse (transmit bandwidth = 4.5 kHz; time-bandwidth = 4). For a single slice containing the fiducial, a TR of 25 ms was used with flip angle $\alpha = 12°$. For the entire phantom volume, the TR was increased to 100 ms for interleaved acquisition and a flip angle $\alpha = 30°$.

The fully sampled axial and coronal datasets were retrospectively undersampled up to R=16, analogous to the simulations, and reconstructed using NUFFT, TGV, and CG-SENSE methods onto a 512 x 512 matrix and then cropped to show the centre 256 x 256 image. Secondly, an undersampled (R=8) dataset was acquired with identical imaging parameters, but with a reduced number of acquired readout spokes with an acquisition matrix of 256 x 102. Since the fiducial marker is cylindrical, the orientation of the phantom was rotated such that the longitudinal axis was pointing perpendicular to B_0 in order to alter the field inhomogeneity and the subsequent hyperintense artifacts. All acquired data was repeated twice in order to perform ROI-based signal and noise calculations of the summation and difference images respectively [105]. Reconstructions were performed using an Intel Core i7 860 and took 8.06, 465, and 242 s for NUFFT, TGV, and CG-SENSE respectively for the undersampled data.

4.3.2.5 Data Analysis

Contrast values of simulated co-RASOR images off-resonance by an ideal frequency offset δf were quantified based on difference between the fiducial signal, which was measured as the mean voxel intensity inside the circular region $r \leq 2\Delta x_{sim}$ and comprised of 5 voxels, to its immediate surrounding, which was measured as the shell of voxels in the range $2\Delta x_{sim} \leq r \leq 1$ mm and comprised of 184 voxels. Each reconstruction method normalized the signal intensity values to the R=1 image.

Acquired co-RASOR images of the fiducial marker were reconstructed with a single frequency offset dependent on the scan plane. Positive contrast was generated by multiplying each readout line by a linear phase ramp according to Equation 4.2. The frequency offsets used when the long axis of the fiducial is parallel to the B_0-field were $\delta f = -1$ kHz in the axial plane and -850 Hz in the coronal plane. When the phantom is rotated, such that the long axis is perpendicular to B_0, the frequency offsets were -1 kHz in the axial plane and -900 Hz in the coronal coronal plane. Fiducial visualization was performed by voxel-wise subtraction of a co-RASOR image off-resonance with its on-resonant image, followed by a threshold of 50% of the maximum intensity. Contrast-to-noise (CNR) measurements were performed using a three-step procedure involving two repeated scans: first, the center-of-mass of a fully sampled co-RASOR threshold image using NUFFT reconstruction was used to define the centre of the fiducial for all subsequent measurements. Secondly, contrast was measured as the mean voxel intensity enclosed by the fiducial subtracted by the surrounding 3 mm shell. The fiducial signals measured were dependent on the known alignment and geometry with respect to the B_0-field. When imaged cross-sectionally, a 1 mm signal region was used that corresponded to a 2x2 voxel area of the image; when

imaged lengthwise, the 5 mm length corresponded to a 6x2 voxel area of the image. Finally, due to the use of phased array coils, the 3 mm circular area relative to the centre of the fiducial was used as the ROI to calculate the standard deviation of the noise by subtracting two repeated scans and calculating the standard deviation within the ROI, σ_{ROI}.[105] CNR was then $\frac{1}{\sqrt{2}}\frac{(c_1+c_2)}{\sigma_{ROI}}$ where c_1 and c_2 were the two contrast measurements of two repeated scans. To reduce the importance of choosing the correct centre voxel, the regions are shifted in each direction of the eight adjacent voxels and averaged together.

The noise measurements around the fiducial of the all difference images (i.e., two acquisition planes and two fiducial orientations with respect to B_0-field) were combined together into six groups, one for each of the reconstruction methods, and one for the undersampling factors of R=1 and R=8. Each image was normalized to account for intensity differences in the reconstruction method. A statistical analysis using Levene's test of equality of variances was performed in order to assess whether the choice of reconstruction method significantly amplifies the noise [106].

4.3.3 Results

4.3.3.1 Simulations

Simulations results for a 1 mm spherical fiducial marker that has been Fourier encoded according to a zero T_E, centre-out radial trajectory are shown in Figure 4.1. The imaging planes are defined relative to B_0, chosen in the z-direction, thus the top two rows in Figure 4.1 are imaged perpendicular to B_0 and represent an axial plane, whereas the bottom two rows are imaged in the coronal plane. The on-resonant images show signal voids enclosing the fiducial along with the hyperintensities from the

signal pile-ups in the characteristic orientation-dependent pattern [107]. As the undersampling factor increases to R=12, radially streaking artifacts are most pronounced using NUFFT reconstruction. TGV and CG-SENSE reconstruction, in the absence of additive noise and signal dephasing, clearly reduce the effect of these streaking artifacts, though the images display appreciable incomplete artifact suppression as well as spatial smoothing. In the axial plane, a global frequency offset shows that the hyperintensities have been radially moved to the geometric centre of the fiducial, and maximal signal intensities occur in the space occupied by the fiducial as desired. In the coronal plane, off-resonant images apply a radial shift globally resulting in positive contrast locally in the centre of the marker, but non-specific elsewhere in the image.

The effect of off-resonance contrast is further explored in Figure 4.2. There is little deviation in contrast for NUFFT and TGV reconstructions as a function of R, whereas contrast in CG-SENSE decreases in the axial plane. Contrast is influenced more by echo time than by the degree of undersampling, as $T_E = 0$ ms has contrast values above 20% maximal image intensity for both reconstruction methods. At $T_E = 4$ ms, contrast is reduced to below 10% maximal image intensity and CG-SENSE is seen to display no positive contrast beyond R=4 in both planes.

4.3.3.2 Phantom experiments

The imaged phantom displays a single platinum fiducial marker, imaged using a dual-plane 2D co-RASOR pulse sequence, in Figure 4.3. A clear signal void and its surrounding hyperintensities are evident in both scan planes and consistent with the

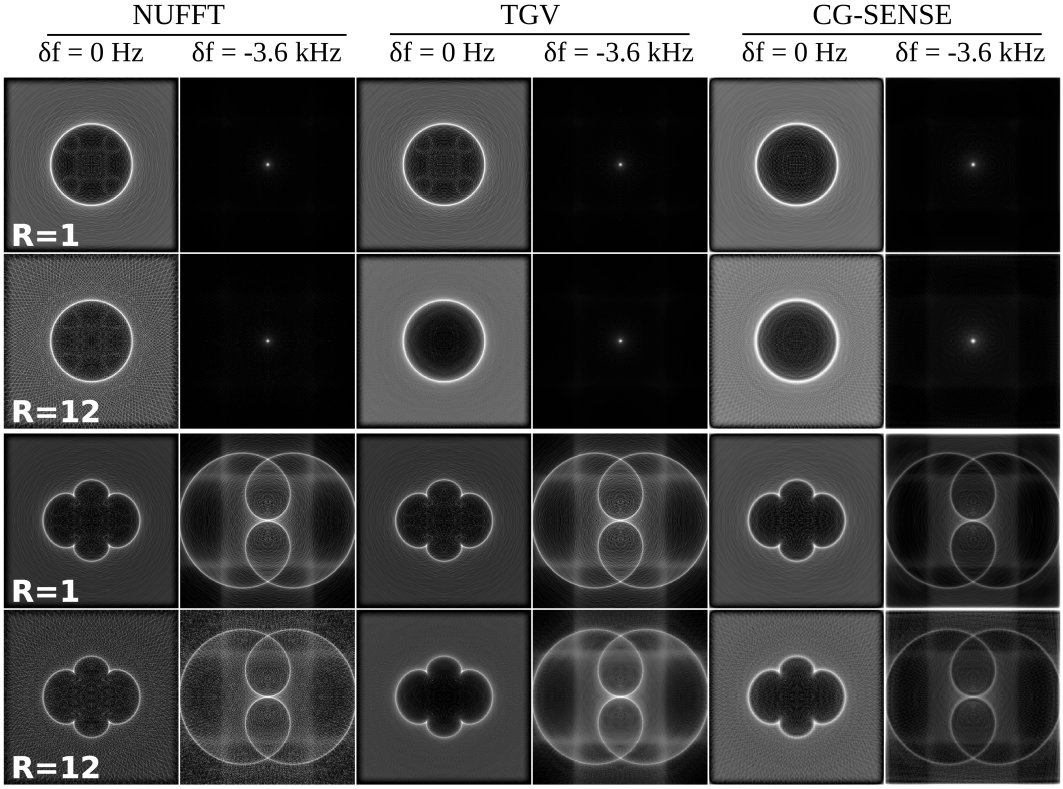

Figure 4.1: Simulated co-RASOR reconstructions at $T_E = 0$ ms of a paramagnetic spherical marker ($a = 1$ mm; $\Delta\chi = -4000$ ppm) imaged in the axial plane (top-half) and coronal plane (bottom-half) with respect to the B_0-field. Data is shown fully sampled and retrospectively undersampled by R=12 for 96 spokes. The first two columns were reconstructed using NUFFT, both on-resonance and off-resonance by $\delta f = -3.6$ kHz; the next two columns use iterative TGV reconstruction with the same frequency offsets, followed by CG-SENSE. In the absence of additive noise and signal dephasing, the radially symmetric signal hyperintensities and uniform background in the on-resonant cases even at higher levels of undersampling.

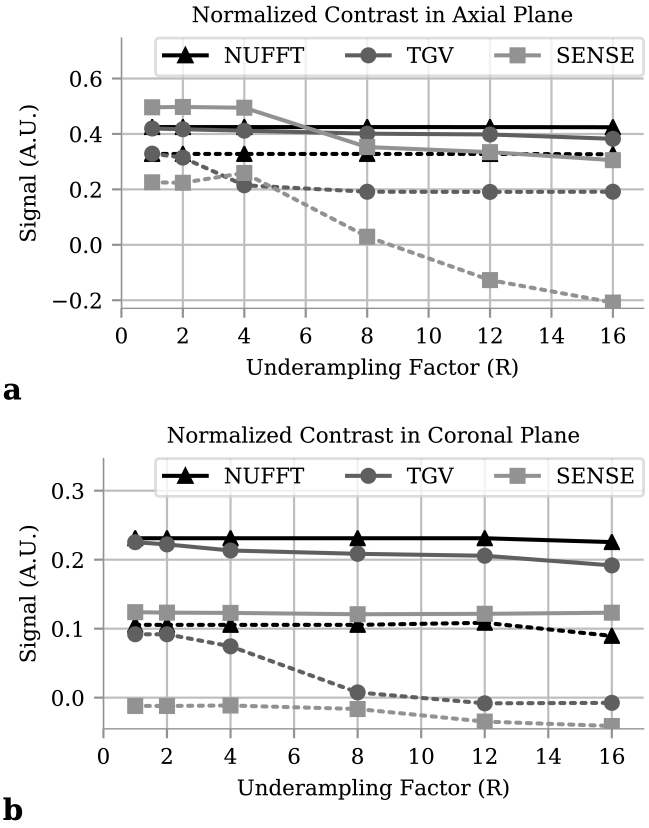

Figure 4.2: Normalized contrast measurements of the simulated off-resonance co-RASOR imagesin the axial **(a)** and coronal **(b)** planes as percentages of the maximal signal at R=1. Solid lines represent simulations taken at $T_E = 0$ ms and dashed lines at $T_E = 4$ ms. The reduction in contrast is influenced mainly by increased echo time compared to the degree of undersampling. Beyond R=4, CG-SENSE reconstruction results reduced positive contrast in for each factor and echo time.

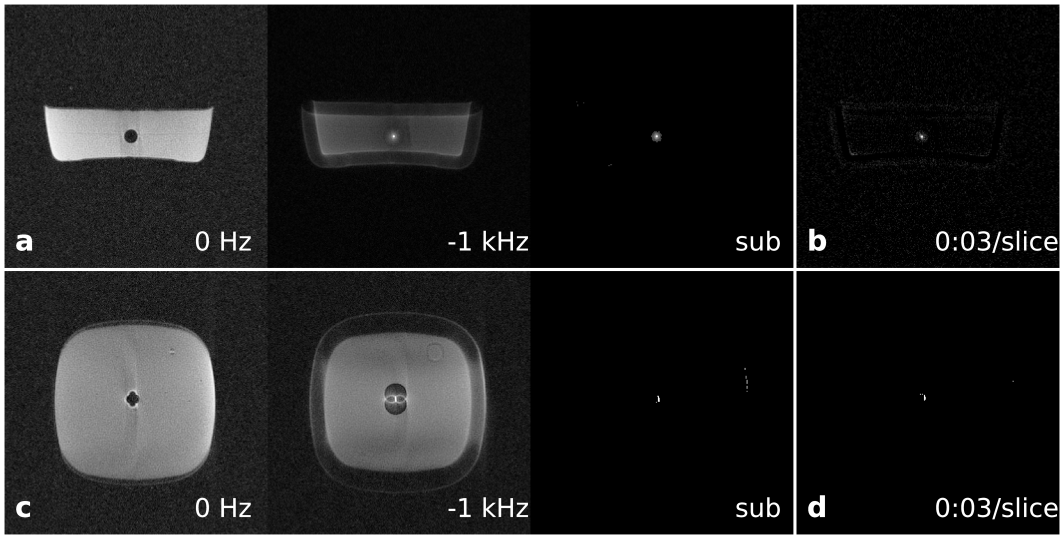

Figure 4.3: A phantom containing a single 3 mm long fiducial marker parallel to the B_0-field in a gel phantom highlighting the co-RASOR reconstruction process. Axial images **(a)** were reconstructed using NUFFT both on-resonance and off-resonance by -1 kHz showing the positive contrast of the fiducial marker. A subtraction image (denoted sub) is also shown with an applied pixel threshold of 50% maximal intensity. An undersampled (R=8) subtraction image **(b)** maintains the fiducial hyperintensity, though imaged in 3 sec/slice. Coronal images **(c)** used a similar frequency offset to the axial case. The undersampled coronal subtraction image **(d)** highlights the lengthwise fiducial marker.

circularly symmetric and dipole patterns seen in the previous simulations. When reconstructed off-resonance by -1 kHz localized positive contrast is observed. To remove as much of the background signal as possible, the off-resonant co-RASOR images are subtracted by on-resonant images and an intensity threshold is used to mask out pixel values lower than 50% of the maximal signal. Accelerated subtraction images of both planes by R=8 are shown in Figures 4.3b,d respectively, taking approximately 2.8 s to acquire a single slice.

The 2D co-RASOR data of the phantom was retrospectively undersampled and CNR measurements about the centre of the fiducial marker are shown in Figure 4.4

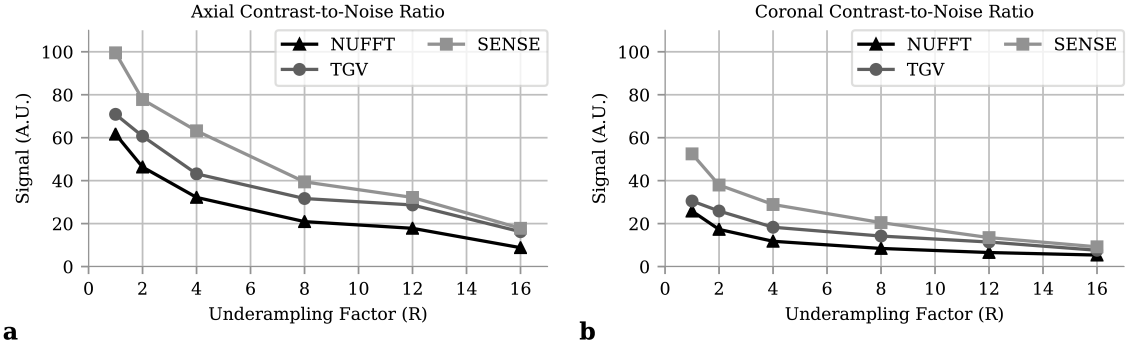

Figure 4.4: Contrast to Noise values for axial **(a)** and coronal **(b)** images of a fiducial marker lying parallel to the B_0-field, retrospectively undersampled starting from 804 projections by factors up to R=16. Contrast, measured from the 2x2 pixel region with respect to a 3 mm surrounding shell, monotonically decreases by approximately $\sqrt{R}$ for each of the reconstruction methods. The contrast is highest in CG-SENSE, followed by TGV, and finally NUFFT for each factor of R.

for the axial and coronal planes respectively. Each curve indicates that the measured CNR values of the fiducial, with respect to its surrounding, is monotonically decreasing in both planes and reconstruction method, with CG-SENSE being the highest in both planes, followed by TGV, and lastly NUFFT. Additionally, the half-maximum area curves are shown for the same undersampling factors in Figure 4.5. For comparison, the solid black lines shown in Figure 4.5a&b represent the true area of the fiducial at 1.4 mm^2 and 4.4 mm^2 imaged in the axial and coronal plane. The area remains consistent for NUFFT and TGV in the axial plane, where CG-SENSE grows past R=4 up to approximately 20 and 40 mm^2 in its respective plane. Magnified views of the fiducial are shown in Figure 4.6 where the increase in the number of voxels encompassing half of the signal maximum is visually apparent for CG-SENSE despite having a higher CNR. The magnified views show the trade-off between resolution of the fiducial and CNR.

An undersampled 2D co-RASOR acquisition was acquired with a single reduction

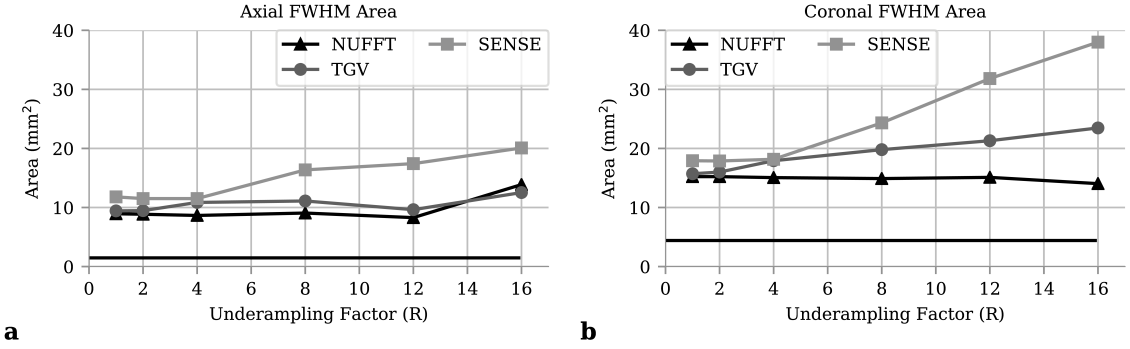

Figure 4.5: Half maximum area values for axial **(a)** and coronal **(b)** images of a fiducial marker lying parallel to the B_0-field, retrospectively undersampled starting from 804 projections by factors up to R=16. The area contains all voxels excluding the central 2x2 fiducial location that are within half of fiducial signal intensity. The solid black line indicates a reference constant fiducial area. The area grows quickest in CG-SENSE as a function of R, especially in the coronal plane.

factor of R=8, shown in Figure 4.7. When the fiducial axis is parallel to B_0, the hyperintense signals are well localized when applying a single frequency offset and subtracting the on-resonance image, followed by a threshold of 50% maximal intensity (first column). The magnified views of these images are also presented (second column). Both acquisition planes in this fiducial orientation show the correct view of the fiducial: the axial plane showing the cross-section and coronal plane showing the long axis. A second set of undersampled 2D co-RASOR images were acquired with the phantom re-positioned such that the fiducial axis is perpendicular to B_0 and lengthwise in the AP-direction. Note that in this orientation, the axial images of the perpendicular columns should have the fiducial lengthwise in space, however the hyperintensities when reconstructed off-resonance incorrectly show a similar pattern to the axial images of the parallel orientation. Conversely, the coronal images should image the fiducial cross-section, however the hyperintensities incorrectly show a similar pattern to the coronal images of the parallel orientation. This implies that

	Parallel to B_0		Perpendicular to B_0	
	Axial	Coronal	Axial	Coronal
Fully Sampled				
NUFFT	109 / 8.94	68.9 / 14.2	51.9 / 13.7	19.3 / 19.8
Undersampled (R=8)				
NUFFT	34.9 / 8.97	19.8 / 15.2	28.4 / 11.9	6.23 / 17.7
TGV	54.2 / 11.5	36.4 / 18.7	59.6 / 14.6	28.8 / 22.9
CG-SENSE	95.2 / 16.2	69.9 / 23.5	73.8 / 18.1	12.0 / 30.9

Table 4.1: Contrast-to-noise / area measurements (mm^2) of acquired undersampled (R=8) fiducial parallel and perpendicular to the B_0-field.

the hyperintense patterns observed are dominated by the initial field inhomogeneity pattern, rather than the intrinsic orientation of the fiducial itself. The contrast values and areas of the respective images are summarized in Table 4.1. While not shown visually, the NUFFT measurements are reported for the fully sampled images followed by the acquired undersampled images as a baseline.

All normalized difference images of both imaging planes and fiducial orientation were combined into six groups for each reconstruction method, and for R=1 and R=8 undersampling factors (Figure 4.8). The noise distributions are zero-mean with standard deviations that are predictably the lowest without undersampling (left group) and increase by factors of 2.38, 1.51, and 0.87 when undersampled and reconstructed with NUFFT, TGV and CG-SENSE respectively. A statistical analysis showed significant ($p < 0.05$) differences among the variances and post hoc pairwise groups were compared with each of the six groups significantly differing from each other ($p < 0.001$).

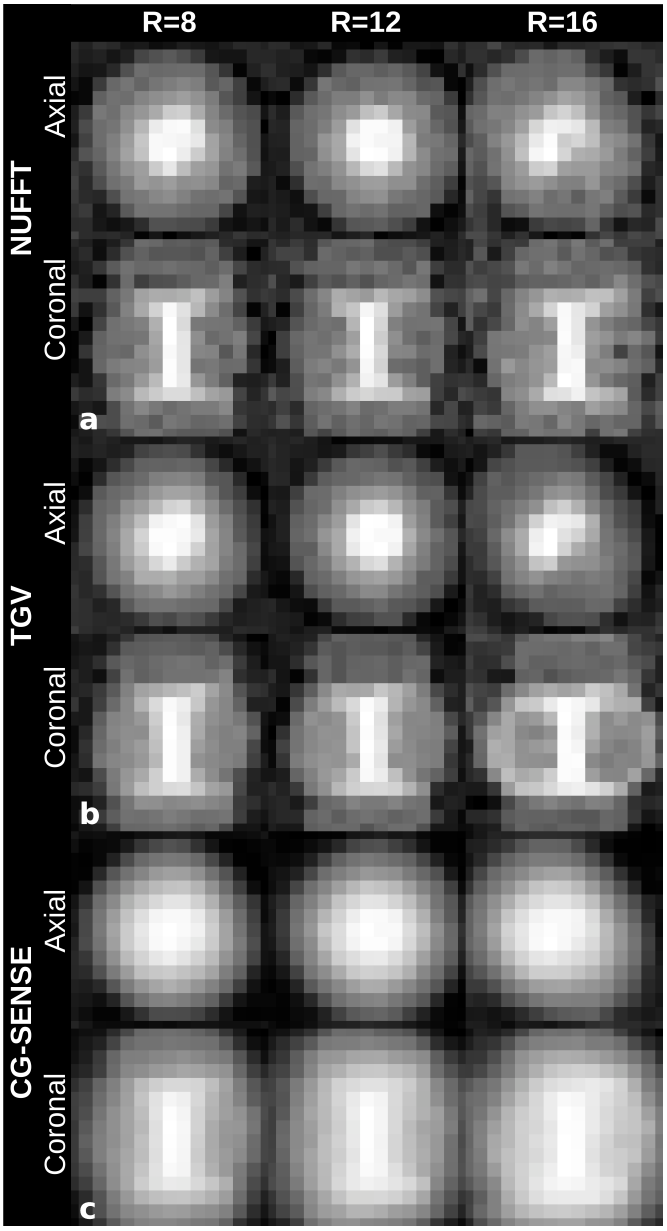

Figure 4.6: Magnified (50x) images interpolated to 256x256 of NUFFT **(a)**, TGV **(b)**, and CG-SENSE **(c)** reconstructions for retrospectively undersampled dual-plane co-RASOR images of a single fiducial lying lying parallel to the B_0-field.

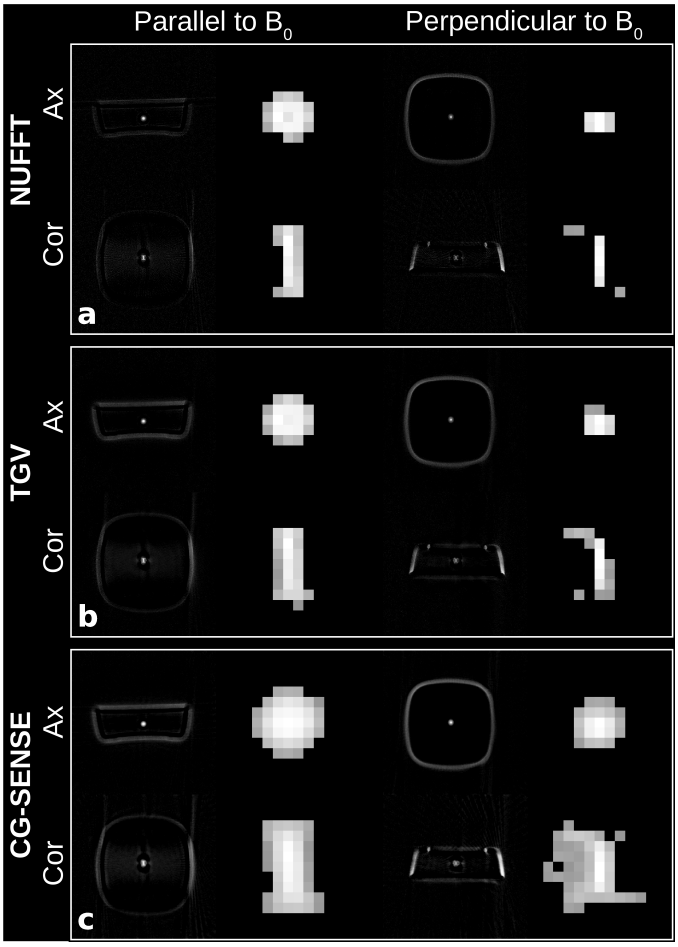

Figure 4.7: Acquired undersampled images at R=8 (102 centre-out spokes) when the long axis of the fiducial is parallel (left columns) and then perpendicular (right columns) to the B_0-field. Dual-plane axial and coronal views are shown alongside a magnified image of the fiducial centre for NUFFT **(a)**, TGV **(b)**, and CG-SENSE **(c)** reconstructions. Off-resonant frequency offsets used for each image ranged from -800 Hz to -1 kHz.

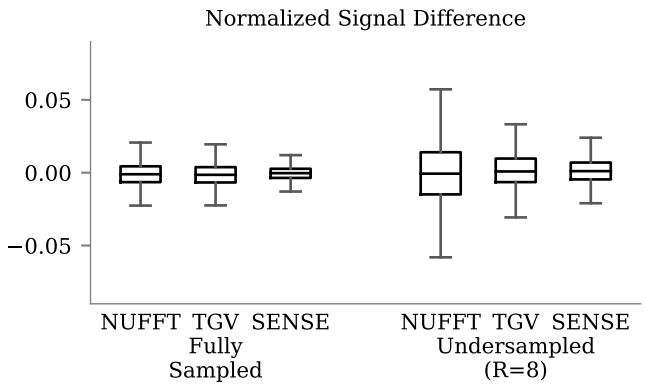

Figure 4.8: Normalized signal differences about the 5 mm region surrounding the fiducial centre of the fully sampled and acquired undersampled (R=8) images. Both fiducial orientations and scan planes are grouped according to the reconstruction method and undersampling to create six groups. Zero-mean normalized differences are observed for fully sampled (left-group) and undersampled at R=8 (right-group).

4.3.4 Discussion

This study utilized a 2D, dual-plane dedicated MR pulse sequence to localize paramagnetic fiducial markers, implanted for radiation therapy planning and co-registration, with positive contrast using centre-out radial sampling with off-resonance reception (co-RASOR). Using a reduction factor of 8 allowed single slice acquisition to be performed in 2.8 s per slice, requiring two planes for a total of ˜6 s. Full phantom coverage using an interleaved and undersampled acquisition required 37 axial slices (3.0 mm thick), imaged in 47 s. When imaged in the coronal plane, the time for 15 slices (3.0 mm thick) was 27 s. Thus, the total acquisition time for the dual-plane undersampled co-RASOR imaging with a total imaging extent of 11.0 cm^2 x 4.5 cm was 73 s, effectively encoding slices at 1.4 s/slice. The imaging planes intersect about the fiducial centre, so that each acquisition uses in-plane localization, and two perpendicular planes can localize the fiducial in three dimensions.

Acquisition speed using 2D imaging has previously been shown to give acceptable images for high-dose brachytherapy seeds [96] and in the presence of metal implants [108]. The 2D sequence used in this study has also shown promise in generating positive contrast in 3D imaging. Seevinck et al [89] first used an off-resonance 3D UTE dual-echo sequence to reduce the background and suppress long T_2^*-components to visualize simulated field perturbers, brachytherapy seeds with similar dimensions, and interventional needles. Their 3D acquisition was undersampled by a factor of $\pi/2$ taking 2 min 43 s to achieve 1 mm resolution at 128 mm^3 coverage. This study exceeds the temporal resolution while imaging at higher resolutions at the expense of total coverage. Additionally, our effective slice encoding time differs from the original dual-plane method which had a temporal resolution of 4.7 s with shorter TE and TR values and used thicker 5 mm slices [96]. This study also expands on the simulations by providing an extra imaging dimension of a spherical perturber and improved in-plane resolution at 0.125 mm (a factor of 8 increase), otherwise all conditions were equal in terms of its size and susceptibility difference. The imaging plane visually influences the hyperintensities in the on-resonance reconstructions as ΔB_z has an angular dependence with respect to the azimuth. Our simulated results show the the differences when reconstructing on-resonance images for each plane. When the azimuth angle is 90°, the hyperintensities become circularly symmetric which can easily be rewinded to the fiducial centre, otherwise only a portion of the hyperintensities can be localized to the fiducial centre while others radially expanded outward. There is some reduction in relative contrast, however the intravoxel dephasing term due to the higher echo times has a much larger influence as contrast is reduced in all cases using $T_E = 4$ ms. Undersampling with co-RASOR has been shown at reduction

factors of R=16 [109] though no contrast values were reported. Other studies using co-RASOR included Diwoky et al. [110], which used a balanced SSFP approach for positive contrast of SPIO-labelled cells at sub-millimetre voxel sizes of 200-400 μm, lower than our in-plane resolution of 0.625 mm and 1 mm slice separation, but at the expense of a long acquisition time of 19 min 48 s. In vitro CNR was also comparable between the paramagnetic fiducial while undersampled, ranging from 19.8 to 95.2 when the fiducial axis is parallel to B_0 and 6.23-73.8 when perpendicular to B_0. Using their reported threshold of a CNR > 5, all of our CNR measurements would meet the defined threshold.

Simulations in the absence of background noise revealed the ability to localize the centre of the field perturber, demonstrated here using 67 centre-out spokes (R=12), despite increased streaking artifacts (Figure 4.1). TGV and CG-SENSE clearly reduce streaking artifacts in the on-resonant images, as the R=12 case both have less streaking artifacts at lower intensity compared to their NUFFT counterpart, which are visible only at the periphery of the images. The normalized contrast values showed that the degree of undersampling has smaller effect than increased echo time as well as imaging in the coronal plane. The coronal plane showed a 10% reduction in contrast which can best be explained that the hyperintensities in the dipole pattern cannot be uniformly rewinded to the centre when reconstructed off-resonance since they are not circularly symmetric compared to the axial plane. Due to intravoxel dephasing, there is signal that cannot be recovered and reconstructed off-resonance for positive contrast, which is exacerbated with CG-SENSE as it displays negative contrast in both planes for most undersampling factors at the increased echo time.

One finding in this study was the increased contrast in vitro of a phantom with

a 3 mm fiducial marker lying parallel to the B_0-field when using the CG-SENSE and TGV reconstruction methods (Figures 4.4-4.5). CNR curves in both planes are plotted for undersampling factors up to R=16. Both TGV and CG-SENSE outperform NUFFT, while TGV has the higher contrast only at R=16 in both planes. However, the increase in CNR of CG-SENSE is offset by its half-maximum area which is worst in both planes and quickly diverges away from NUFFT and TGV past R=4. The algorithm for iterative reconstruction using variational penalties used by Knoll et al. [99], uses a set parameters to control regularization weighting that this study reduced to prevent over-smoothing of the off-resonance images. The simulation results visually demonstrated the denoising properties of TGV, especially in the case of on-resonant reconstruction where the spin density is constant in the areas past the signal hyperintensities. The edges around the longitudinal hyperintensities are accentuated when reconstructed off-resonance with TGV since the undersampling streaking artifacts overlap most in these regions creating strong signal oscillations compared to the periphery where the streaks are individually evident. Variational penalties minimize the signal oscillations and preserve the edge. The number of voxels defining the edge is unchanged and no blurring is experienced, and the signal areas immediately adjacent are more smooth, lowering the standard deviation of the background noise. Conversely, the edges are less defined using CG-SENSE (Figure 4.6) where the magnified images presented show that not only has the half-maximum area increased dramatically, but also the roll-off between the fiducial and its surrounding appears smoother. These reconstructions were once again applied to an acquired undersampled image, shown in Figure 4.7 and summarized in Table 4.1. The area is visually larger using CG-SENSE, with the worst case measuring up to 30 mm^2, while TGV has less area

for all measured undersampled images and outperforms in contrast when the fiducial axis is perpendicular to the B_0-field.

The CNR results in this study of retrospectively undersampled data used Equation 4.3 to predict the CNR decrease, which is used for Cartesian SENSE reconstruction in parallel imaging [111]. The g-factor in this equation represents a pixel-wise evaluation of the noise enhancement beyond the theoretical increase with $\sqrt{R}$. In addition to SENSE, other parallel reconstruction techniques such as GRAPPA have accurately generalized g-factor calculations to create quantitative pixel-wise maps [112], as well as extensions to non-Cartesian trajectories [113]. These extensions, however, do not exceed R=4 for radial undersampling and require prior calibration, thus our study restricted the reconstruction techniques to NUFFT and the iterative TGV method, while comparing to CG-SENSE using the same coil sensitivity estimates as the TGV to demonstrate only the differences between the two iterative algorithms. In our analysis, we made the assumptions that the g-factor does not spatially vary over a 5 mm radius and the noise within a the region surrounding the fiducial is zero-mean with a single standard deviation. This was tested by combining the noise measurements in the ROIs from the dual-plane images in both fiducial orientations and grouped according to reconstruction method and undersampling. Significant differences among the all variances were observed (Figure 4.8) as the standard deviation of the noise for the grouped TGV values were lower by a factor of 1.58, and the grouped CG-SENSE values were lower by a factor of 2.65 compared to NUFFT when undersampling at R=8. The analysis of the noise is also important in order to put the CNR values into context: while increases in CNR can be observed using CG-SENSE, the signal difference between the fiducial centre and its surroundings is lower than the benefits

gained from the reduction of noise. It seems appropriate for the context of fiducial localization to sacrifice some CNR, due to an increase in the global noise level of the entire region, if there is a sharper distinction between fiducial and surrounding, so long as the CNR is above some operator tolerance.

One limitation of using a 2D dual-plane sequence is transmit bandwidth selecting a smaller region of off-resonant spins to be included in the hyperintensities. We attempted to minimize this by choosing the minimum possible T_E and RF-excitation time, which would increase the bandwidth. However, at slice thickness of 3 mm, the maximum transmit bandwidth possible is approximately 4 kHz, differing from the 3D sequence of 40 kHz. The simulations do adequately address this as they assume an infinite transmit bandwidth meaning that all frequency deviations from the Larmor frequency are included when encoding k-space. Differences in the reconstruction method included reconstructing offline using a single frequency offset, compared to de Leeuw [90], where a range of frequency offsets from -8 kHz to +8 kHz in 100 Hz steps were used to create a maximum intensity projection, such that a single optimal frequent offset would not need to be known. In our experience, only a handful of values need be used in order to radially shift the hyperintensities by 1-2 pixels to the centre. Their method requires 160 unique reconstructions, which is far too long when using iterative methods without GPU acceleration. This limitation means all contrast measurements are dependent on a single frequency offset, though it is noted that positive contrast was successfully generated in all imaging planes and fiducial orientation. Using a single offset frequency has an advantage in the measured noise characteristics, as the same offset is used for the fully sampled and undersampled cases, and for each reconstruction technique. The fiducial background region used to

measure CNR is dependent on the strength of the offset frequency and will introduce structured noise because the offset frequency is applied globally to create image domain shifts. The noise suppression seen in the TGV2 and CG-SENSE reconstructions then result from the iterative techniques themselves. The longer reconstruction time with TGV also differs from Knoll [99, 100] in that we used all 32-channels without coil compression down to 8-channels and no CUDA acceleration. The majority of our reconstruction time comes from applying TGV penalty over 500 iterations and took 465 s. Their work, however, showed that with hardware acceleration, a full 32-channel acquisition can be reconstructed offline in the range of 100 s. Quicker reconstructions would be beneficial, as the fiducials should be localized visually and then accepted prior to moving on to the next scan or ending the patient's examination.

4.3.5 Conclusions

This study presents a methodology and critical analysis of using a dedicated dual-plane 2D co-RASOR pulse sequence, while employing the use of undersampling the number of acquired lines in k-space. The total acquisition time to localize a fiducial marker in vitro was reduced to 73 s when imaging 37 axial and 15 coronal slices. The choice of reconstruction method alters contrast and area in acquired undersampled data in both fiducial orientations and scan planes. Using an iterative reconstruction method with variational penalties has a reduced fiducial area with acceptable contrast, but its use must be balanced against an increased reconstruction time.

Acknowledgments

This project is based upon work supported by the Ontario Graduate Scholarship (OGS). The authors also thank the financial contributions by Robert Dunsmore.

Chapter 5

Differentiating Platinum Coated Brachytherapy Seeds and Gold Fiducial Markers with Varying Off-Resonant Frequency Offsets

5.1 Context of Paper

In this study, we utilized the off-resonant frequency information in dual-plane 2D co-RASOR images, which were reconstructed with a large range of frequency offsets, in order to differentiate between a single low-dose rate brachytherapy seed and a gold fiducial marker. In typical co-RASOR imaging, seeds with strong field inhomogeneities should display with positive contrast by rewinding to appropriate frequency offsets. The physical properties of each seed have opposite polarities in their magnetic

susceptibilities, and thus rewind to frequency offsets with opposite signs, where the application of two frequency offset filters can separate the signal contribution from each seed.

The methodology was implemented by modifying the reconstruction method to create a new pipeline which displays two superimposed maximum intensity projections from only negative filtered and positive filtered offsets. For all acquired imaging planes, and seed orientations with respect to the main magnetic field, each seed global maximum was separated to opposing frequency regions, and displayed a higher relative difference between all other local maxima. This was tested in simulation, and validated in both a gel phantom and porcine tissue. It was concluded that selective positive contrast is achievable and colour-coded masks can be overlaid onto co-RASOR images display unique seeds.

5.2 Declaration Statement

Evan McNabb acquired the data, performed the data analysis, interpreted results, and drafted the manuscript text. Additionally, he created the manuscript figures, and tables. The contributions by Evan McNabb warranted his name as first author.

Dr. Michael Noseworthy, as corresponding author, designed this project as multi-disciplinary biomedical engineering project as part of his years of expertise in the field of Magnetic Resonance as well as developing engineering applications to serve clinical needs. He provided critical analysis of the methodology, interpretation of results, and manuscript revisions of the final article that he submitted for publication. Finally, he provided thorough guidance and helped secure funding resources.

Dr. Raimond Wong conceptualized the clinical rationale for this project based

on his expertise as an interventional oncologist. He provided the clinical materials used for research, provided guidance in tailoring the engineering principles to clinical outcomes. Finally, he also secured funding resources.

This paper was submitted to Magnetic Resonance Imaging April 26, 2018.

5.3 Paper

Differentiating Platinum Coated Brachytherapy Seeds and Gold Fiducial Markers with Varying Off-Resonant Frequency Offsets

Evan McNabb[a], Raimond Wong[b,c,d], Michael D. Noseworthy[a,e,f,g,*]

[a]McMaster School of Biomedical Engineering, McMaster University, Hamilton, Canada
[b]Juravinski Cancer Centre, Hamilton, Canada
[c]Department of Oncology, McMaster University, Hamilton, Canada
[d]Department of Medicine, McMaster University, Hamilton, Canada
[e]Imaging Research Centre, St. Joseph's Healthcare, Hamilton, Canada
[f]Department of Electrical and Computer Engineering, McMaster University, Hamilton, Canada
[g]Department of Radiology, McMaster University, Hamilton, Canada
[*]Corresponding author at: Department of Electrical and Computer Engineering, McMaster University, Engineering Technology Building, ETB-406, 1280 Main St. W, Hamilton, Ontario, Canada, L8S 4K1. Email: nosewor@mcmaster.ca

Abstract

Purpose: To develop an off-resonant frequency filtered method to selectively differentiate between implanted gold fiducial markers and platinum coated brachytherapy seeds.

Methods: The magnetic susceptibilities for gold fiducial markers and brachytherapy seeds differ in magnitude and also in their signs, resulting in B_0-field inhomogeneity

patterns with opposite main lobes. A pulse sequence used to localize brachytherapy seeds with positive contrast, centre-out radial sampling with off-resonance reception (co-RASOR), was used to reconstruct images with a range of off-resonant frequency offsets. The proposed method utilizes two frequency filters to selectively reconstruct maximum intensity projections through band-pass regions where each seed has its maximal localized hyperintensity. Seeds were simulated and then placed in gel and tissue phantoms to validate the technique using orthogonal 2D slices with seeds both parallel and perpendicular to the B_0-field.

Results: Dual-plane 2D co-RASOR sequences were reconstructed off-resonance with applied frequency filters to create two projections displaying each seed, which were then colour-coded to negative and positive frequencies. Phantom validation showed that each seed contains its maximal CNR in opposing frequency regions as predicted. Local maxima can also appear in both negative and positive frequency regions. The relative difference between the signal of each seed and these local maxima ranged from 1.19 – 3.73, and an image threshold was determined in all cases. Tissue validation showed the technique differentiates seeds correctly in at least one-plane for both orientations, and is limited by the hyperintensity patterns observed in the co-RASOR method.

Conclusion: Dual-plane co-RASOR offers sub-millimetre positive contrast from implanted seeds that contain unique off-resonant frequency maxima, with which frequency filters can selectively differentiate.

Key Words: co-RASOR, contrast, gold fiducial marker, platinum, brachytherapy, visualization

5.3.1 Introduction

Magnetic resonance (MR) imaging has seen continued use for management of prostate image guided radiation therapy (IGRT) due to superior soft tissue contrast compared to computed tomography (CT), thus leading to reduced clinical target volumes and interobserver variability [74, 114]. The dosimetric and geometric accuracy of MR-only based treatment procedures have been recently reported with acceptable differences in doses <2% [19, 21, 115, 116]. MR adoption has been aided through the use of MR simulators that use flat-top benches in therapy position, procedures to standardize immobilization, and dosimetric calculations from MR-only data [1, 117, 118].

Two current issues in MR-only workflows are (i) identification of implanted gold fiducial markers (GFMs) with positive contrast, and (ii) differentiating GFMs from brachytherapy seeds in patients undergoing radiosurgical external beam radiation therapy for regional recurrent disease. The latter requires a small FOV CT scan that adds to pre-treatment acquisition time in sites attempting MR-only workflows [18]. Identifying paramagnetic SPIOs with positive contrast has been reviewed for a number of 3D sequences [88, 119–121], susceptibility approaches [122], template matching algorithms [85, 87, 123] and machine learning from multi-parametric MR [124], all taking advantage of signal void artifacts to build models and improve detection rates of GFMs over standard negative contrast imaging. However, differentiating GFMs and therapy seeds directly with the same pulse sequence remains insufficient. An MR pulse sequence, developed for visualizing low-dose rate brachytherapy seeds with positive contrast, centre-out radial sampling with off-resonance reception (co-RASOR), has shown promise by radially rewinding hyperintense signal pileups towards the centre artifact by reconstructing offline using a projection of off-resonant frequency

offsets [89, 90]. Furthermore, it can be implemented as a fast dual-plane 2D acquisition improving imaging times over 3D approaches [96].

Here we propose to differentiate the two seeds based on their magnetic susceptibilities, with gold being diamagnetic ($\chi_m < 0$) and the platinum layer of the brachytherapy seed being paramagnetic ($\chi_m > 0$). This alters the B_0-magnetic field inhomogeneity patterns observed using the co-RASOR signal model as the signs of ΔB_z are opposite for each seed for similar orientations. Each seed can then be reconstructed using a smaller subset of off-resonant frequency ranges and individually identified with positive contrast from a dual-plane sequence.

5.3.2 Methods

The reconstruction modifications to the co-RASOR sequence with the off-resonant frequency regions used for calculating maximum intensity projections (MIPs) are shown in Figure 5.1. The in-plane B_0-field homogeneity distortions from two spherical field perturbers create hyperintense signal pileups that can be reconstructed off-resonance for a range of offsets. The existing co-RASOR reconstructions use iterative techniques, applying a range of off-resonant reconstructions, followed by a maximum intensity threshold over the frequency offsets, to find the offset that maximizes the image domain intensity. The image is then reconstructed at this optimal offset. By removing this frequency from the set and repeating the process a final superimposed image of all thresholded seeds are found. The proposed method utilizes the fact that signal pileups are maximal for alternating signs, and are centred at distinct frequency offsets at smaller bandwidths (light and dark shaded regions in Fig. 1 denoted as Δf_1 and Δf_2 respectively). A MIP can be used to mask each perturber that can be

superimposed and colour-coded to visualize each individually.

All MR images were acquired using a 3T GE Discovery MR750 (General Electric Healthcare, Milwaukee, WI) with maximum gradients of 50 mT/m and 200 T/m/s slew rate, using a 32-channel head coil. The gold seeds were diamagnetic GFM (IZI Medical Products, MD, USA) with diameter 1.2 mm and length 3.0 mm. The brachytherapy seeds were paramagnetic 125-I LDR (DraxImage Model LS-1, Quebec, Canada) with diameter 0.8 mm and length 4.3 mm, containing a 10% platinum outer layer. All image reconstruction was done using a non-uniform Fast Fourier Transform (NUFFT) [103] implemented in MATLAB R2014b (The Mathworks Inc, Natick, MA). Two fully sampled pulse sequences were used to identify the seeds: 3D bSSFP and dual-plane co-RASOR (described below for each experiment) without the use of acceleration.

To selectively differentiate GFMs and LDR brachytherapy seeds, we first demonstrated the proposed method in a numerical simulation using cylindrical objects with magnetic susceptibility differences $\Delta\chi_m$ = -25 ppm and $\Delta\chi_m$ = +50 ppm to approximately match those of GFMs and brachytherapy seeds respectively [125]. The differences in size and field inhomogeneity are shown in Figures 5.2a-b). The simulated phantom was sampled onto centre-out k-space (FOV = 4 cm; 10 slices, thickness = 4 mm, 128^2 matrix). The GFM and brachytherapy seeds were visually identified as colour-coded masks (Fig. 5.2c-d) in the following manner. First, reconstructions of k-space, off-resonant by a range of frequency offsets δf_i (-4 kHz to +4 kHz in step sizes of 80 Hz) were performed, resulting in a series of i-images. The on-resonant image is subtracted to suppress the bulk background signals. Next, a frequency filter was used to isolate the hyperintense signals from each seed since positive contrast

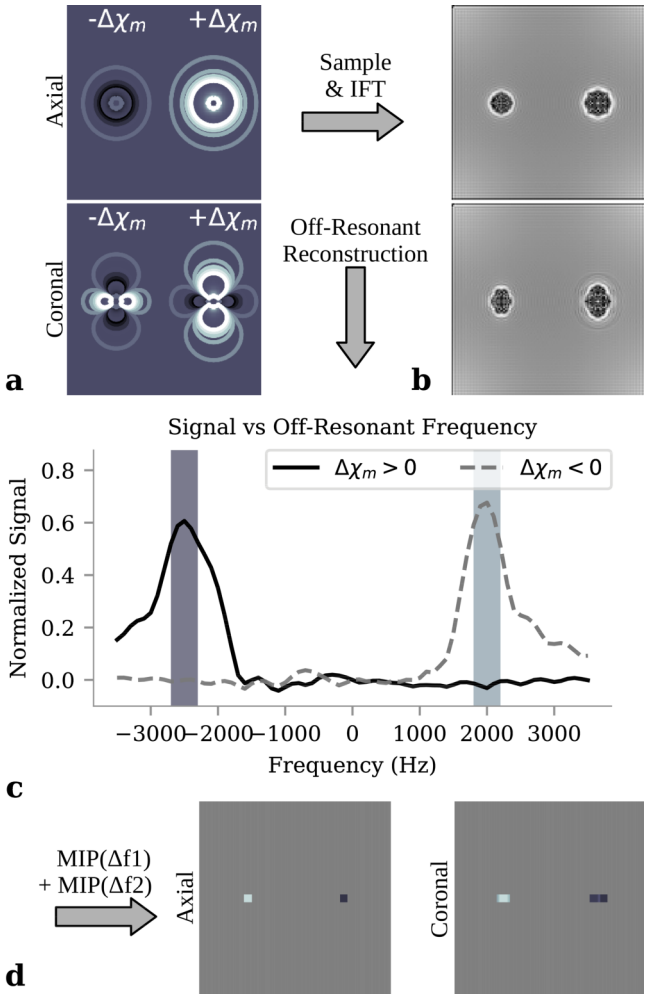

Figure 5.1: Field inhomogeneity with contour lines in two imaging planes of spherical perturbers with negative and positive susceptibility **(a)** and the subsequent co-RASOR image highlighting signal pileups symmetrically around the perturbers **(b)**. The centre pixel intensities in the axial plane are shown as a function of off-resonant frequency offset, where the signal maxima are located (light and dark shaded bandwidths) at distinct negative and positive offsets **(c)**. Performing a MIP over each of these bandwidths can visualize each perturber separately (light and dark overlays) at the geometric centre of the perturbers in each plane **(d)**.

can be isolated to unique positive and negative δf_i offsets. The positive and negative frequency filters have the following form:

$$H_N = rect\left(\frac{\delta f_i + \alpha_N}{\Delta f_{BW}}\right)$$

$$H_P = rect\left(\frac{\delta f_i - \alpha_P}{\Delta f_{BW}}\right) \tag{5.1}$$

where α_P and α_N were set to +2000 and -2500 Hz respectively. These values were chosen experimentally to preserve the largest off-resonant signal maxima, and suppress both the opposite half of the frequency offsets, and values closer to 0 Hz containing background signals. In both planes, localized positive contrast was maximal for the GFM at negative offsets and for the brachytherapy seed at positive offsets, depicted by arrows in Figure 5.2e. Finally, after the filter was applied element-wise to the i-images, a MIP followed by an image threshold (50%) was applied to visualize each seed as a negative-filtered image and positive-filtered image. The frequency filters are further shown in Figure 5.3. The positive and negative filters, followed by a MIP through the off-resonant frequencies are shown for the axial and coronal planes (Figs. 5.3a,b), and with a 50% threshold to create individual positive contrast of each seed (Figs. 5.3c,d), which were used for the colour overlays.

A 3D bSSFP (TE/TR = 1.3/3.5ms, bandwidth = 976 Hz/pixel, FOV = 12.0 cm^2, 256x256, thickness = 1.0mm, NEX = 2, $\alpha = 10°$) was used to image the entire volume of interest with T2/T1 contrast to clearly display both seeds with negative contrast with respect to background. The 2D dual-plane co-RASOR sequences (TE/TR = 2.7/25 ms; FOV = 16.0 cm; thickness = 3.0 mm; matrix = 256x804; bandwidth =

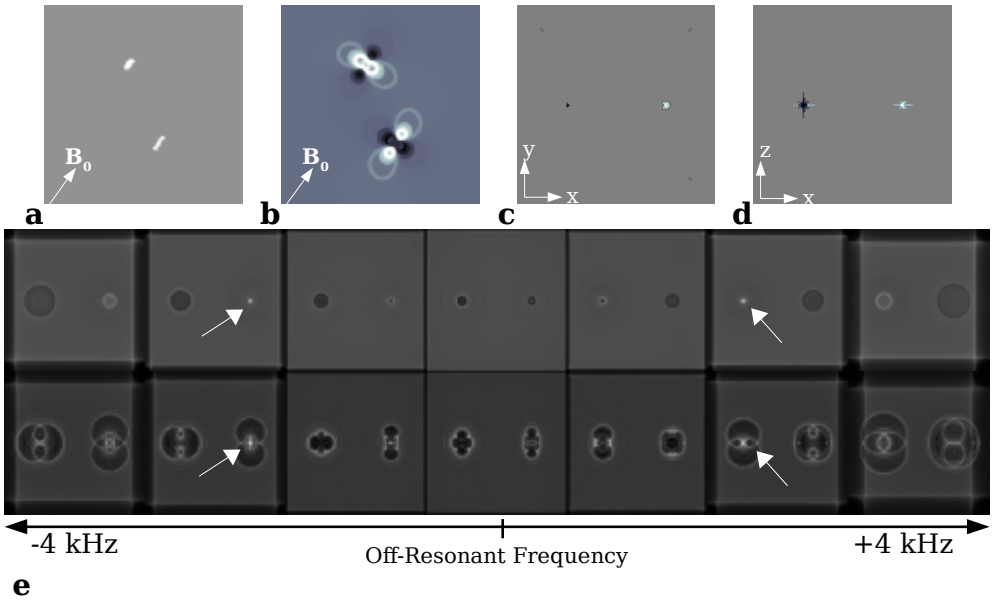

Figure 5.2: Viewpoint projections of a simulated LDR brachytherapy seed and a gold fiducial marker **(a)** and their respective field inhomogeneity patterns displaying opposite patterns **(b)** lying parallel to the B_0-field. Reconstructed dual-plane co-RASOR images using both a positive and negative off-resonant frequency filter displays each seed individually (light and dark overlays) in the axial **(c)** and coronal **(d)** planes. The opposite field inhomogeneity patterns cause the hyperintense signals of each seed (white arrows) to be maximal at negative and positive frequency positions **(e)**.

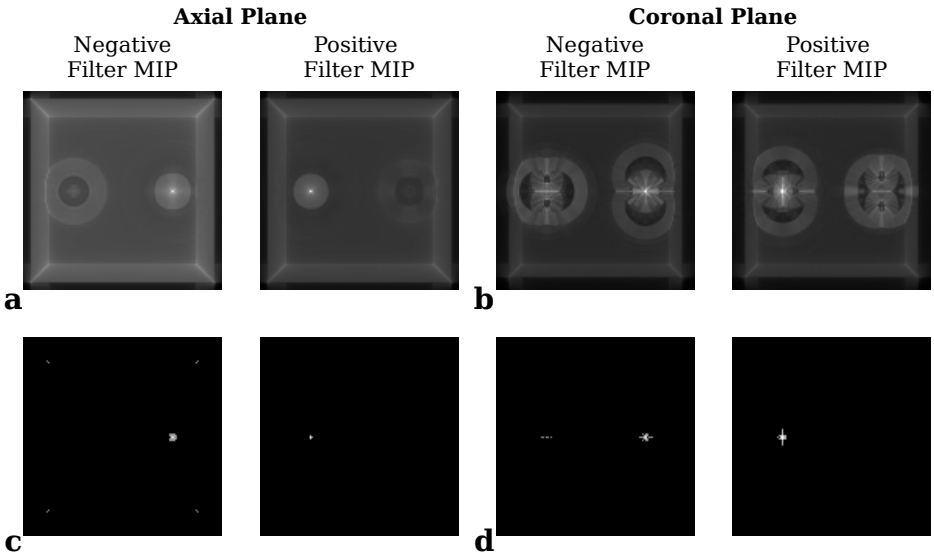

Figure 5.3: Maximum intensity projections through the off-resonant frequencies with the applied negative and positive filters from the numerical simulations in the axial **(a)** and coronal **(b)** planes. Positive contrast is seen surrounding each seed using a single filter. A 50% threshold was applied in both planes **(c-d)** to suppress background signals further.

244 Hz/pixel) were scanned orthogonal in the axial and coronal planes. Both planes were selected to intersect and cover the entire fiducial expected fiducial region of field inhomogeneity from each seed. Slice selection was performed with a one-cycle SINC pulse (transmit bandwidth = 4.4 kHz; duration = 900 μs) in order to minimize echo time and intravoxel dephasing. All co-RASOR data was acquired on-resonance, with linear phase ramps modulating each k-space spoke by δf_i prior to image reconstruction in 50 Hz increments.

The two seeds were first placed in a 3% agar phantom lying co-planar parallel to the B_0-field. The 3D bSSFP was scanned coronally with an extent of 8.4 cm and a scan time of 3:59. Dual-plane co-RASOR scans were performed with 5 axial slices covering 15 mm in the SI-direction and 6 coronal slices covering 18 mm in the AP-direction, for a scan time of 1:22 for each volume. Off-resonant reconstruction of both planes were performed over the range of -1300 to +1300 Hz and the off-resonant frequency filters were applied with α_P and α_N set to +/- 350 Hz, followed by MIPs through the positive and negative band-pass regions to visualize each seed individually. Contrast-to-noise (CNR) curves were calculated by two repeated scans using the average signal from a 2x2 pixel region encompassing the centre of each seed, as determined by the bSSFP and on-resonant co-RASOR scans, and subtracted by from the signal of a 3 mm shell surrounding this area. The signal difference was divided by the standard deviation of the noise within the 3 mm shell to obtain the CNR for each seed as a function of off-resonant frequency. The noise is derived from the difference of two successive scans [105]. The scans were repeated with seeds lying perpendicular to the B_0-field as this changes the field inhomogeneity pattern for each seed.

Finally, two seeds were injected into porcine muscle tissue, obtained from a local food market, with a needle and guiding wire and placed in a container with external fiducial markers, shown in Figure 5.4. The porcine tissue was imaged with seeds parallel to B_0 using a coronal bSSFP (20.0 cm x 9.6 cm, α=10°) for a scan time of 4:06. Dual-plane co-RASOR images were acquired undersampled (402 spokes) in the axial and coronal directions covering 18 and 15 mm respectively for a scan time of 0:43 each. The porcine sampled was then rotated with the seeds lying perpendicular to B_0 and the study was repeated, with 19 axial slices covering 57 mm in the SI-direction and 6 coronal slices covering 18 mm in the AP-direction, for a scan time of 1:24 and 0:43 respectively. The frequency filters and reconstruction ranges used were identical to the phantom experiment above.

5.3.3 Results

Images from the bSSFP, on-resonant 2D co-RASOR, and the frequency filtered masks in a phantom containing a LDR brachytherapy seed and GFM are shown in Figure 5.5. Orthogonal views are shown for each sequence, although the axial view for the bSSFP has been reformatted from a coronal acquisition. The frequency filtered images were obtained by applying the negative and positive frequency filters over the range of slices displaying field inhomogeneity patterns from the seeds, followed by maximum intensity projections, and global image threshold. Comparing bSSFP and on-resonant co-RASOR, the bSSFP displays non-specific negative contrast and severe banding artifacts when formatted in the coronal plane. Likewise, negative contrast was seen in the on-resonant 2D co-RASOR images, however the hyperintense signal pileups were evident around each marker (curved arrow LDR; straight arrow GFM)

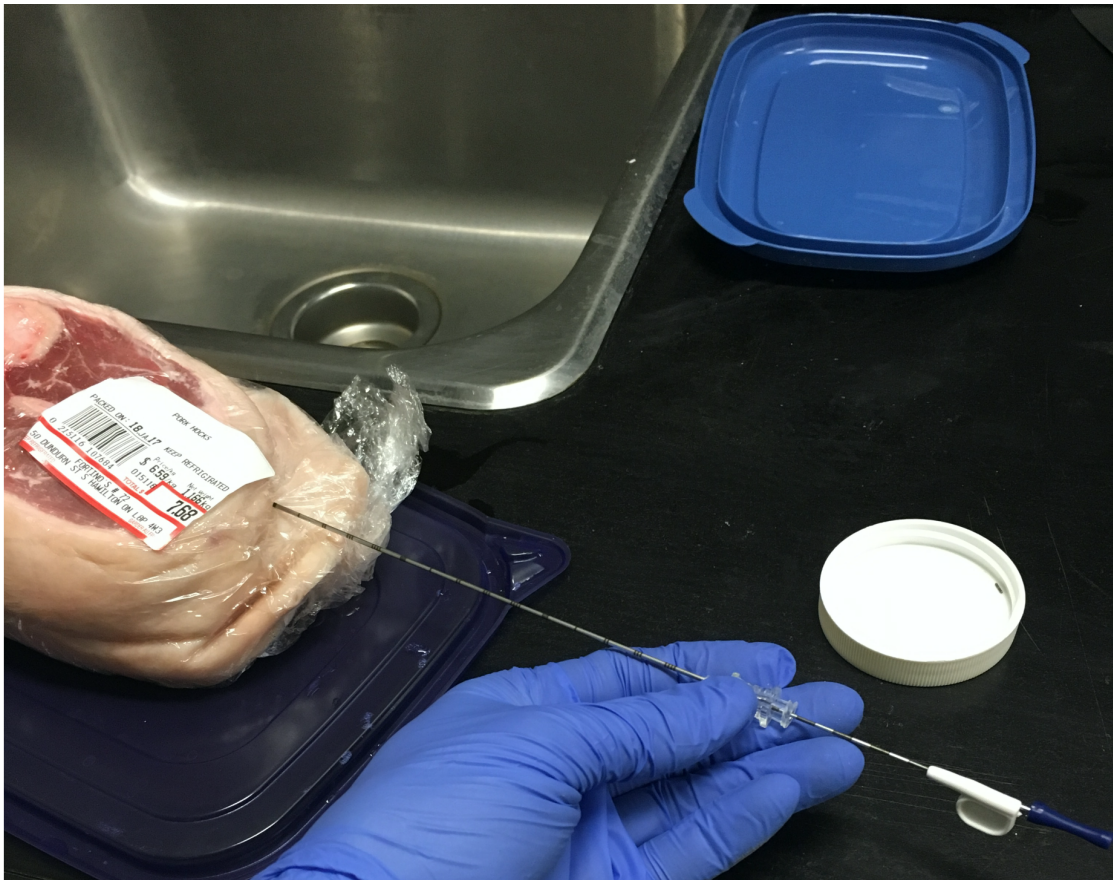

Figure 5.4: Needle Injection of a LDR brachytherapy seed and GFM into porcine tissue. Each seed was inserted approximately 5 cm into the distal end relative to the bone.

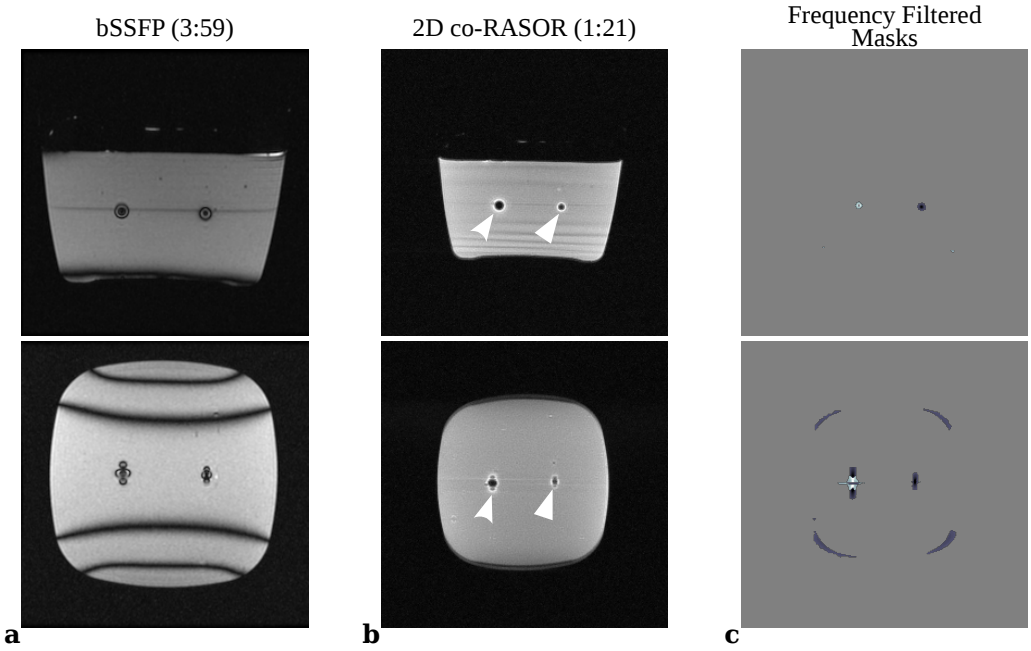

Figure 5.5: Comparisons of negative contrast bSSFP sequence **(a)**, on-resonance 2D co-RASOR displaying hyperintensities **(b)**, and the proposed frequency filtered masks that highlight a LDR brachytherapy seed and gold fiducial marker respectively **(c)**. The acquired planes are axial (top-row) and coronal (bottom-row) with each seed parallel to the B_0 field. The 3D bSSFP produces higher global SNR compared to 2D co-RASOR, but identifying unique seeds is difficult because the size of the signal void depends both on the size of the seed and its magnetic susceptibility. However, frequency filtered co-RASOR can produce superimposed masks of each seed.

which can be radially rewinded with negative and positive frequency filters to mask each individual seed.

The contrast mechanism for masking seeds based on opposite magnetic susceptibility is further explored in Figure 5.6, where CNR curves are displayed from the cross-sectional area of each seed (Fig. 5.6a,b), and the long-axis area (Fig. 5.6c,d) parallel and perpendicular to the B_0-field. Each CNR maximum occurs in the frequency band-pass region highlighted by the colour-coded shaded areas. MIPs can then be

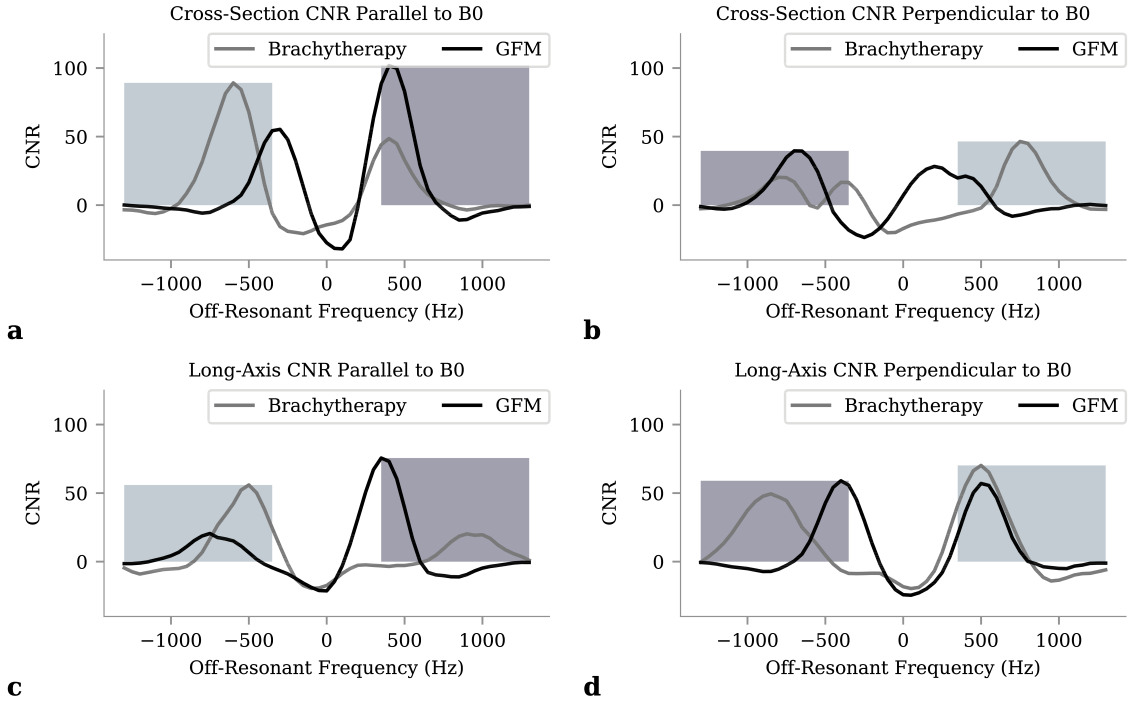

Figure 5.6: Contrast-to-noise curves centred on the cross-sectional area of the LDR brachytherapy seed (gray curve) and GFM (black curve) parallel **(a)** and perpendicular **(b)** to the B_0 field. Similarly, CNR curves centred on the long-axis of each seed both parallel **(c)** and perpendicular **(d)** to the B_0 field are displayed. The shaded regions correspond to the band-pass region of the applied negative and positive off-resonant filters, and their heights match the global maxima of each CNR curve, highlighting that the signal maxima are localized to their unique offset frequencies. Local maxima from the opposite seed were observable, however smaller in all cases.

taken across the band-pass range in the series of off-resonant images. Smaller, local maxima were also observed for each curve on the opposite off-resonant frequency region as the side lobes of the inhomogeneity match the opposite seed's main lobe. The relative CNR differences between the brachytherapy seed's maximum and local maxima in the displayed frequency regions were 1.64, 2.19, 2.72, and 1.23 for each of the seed orientations, respectively. Similarly, the relative differences between the GFM's signal maximum and local maxima were 2.09, 1.94, 3.73, and 1.19.

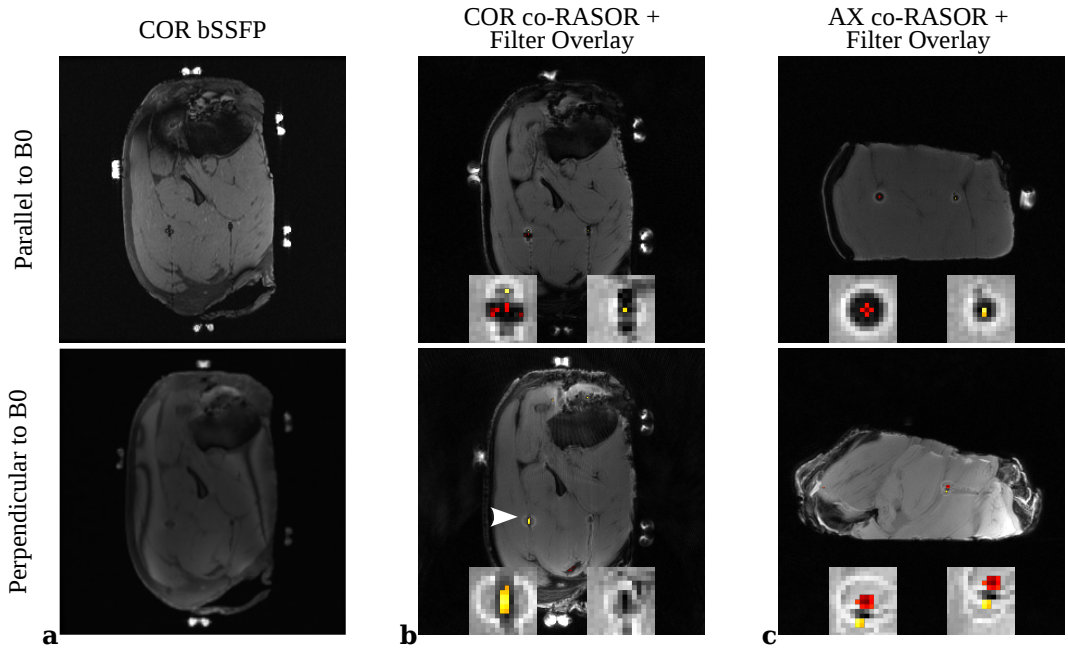

Figure 5.7: Comparisons of a negative contrast bSSFP sequence **(a)** with on-resonance 2D co-RASOR images with frequency filtered overlays in the coronal **(b)** and axial **(c)** directions. Both seeds are shown lying parallel (top-row) and perpendicular (bottom-row) to the B_0 field. The colour overlays represent the negative frequency MIP (red) and positive frequency MIP (yellow). The GFM displays an absence of positive contrast in the coronal plane when perpendicular to B_0 and the positive contrast is inverted for the LDR brachytherapy seed (highlighted by the white arrow).

Images from the porcine sample are displayed in Figure 5.7 including the bSSFP for negative contrast, and frequency filtered masks that are colour-coded and overlaid onto on-resonant co-RASOR from the slices containing the seeds. The bottom insets display zoomed colour-coded masks from negative and positive frequency filtered MIPs. These correctly identify each seed with the exception of the coronal plane perpendicular to B_0 as the GFM can no longer be differentiated due to the unequal and low signal hyperintensities. The bSSFP images also have negative contrast depending on acquired plane and orientation with appreciable contrast reduction and banding when imaged perpendicular to the B_0-field.

5.3.4 Discussion

Dual-plane co-RASOR can be used to selectively differentiate seeds with opposite polarity in their magnetic susceptibilities as their signal pileups rewind to the centre of each seed at off-resonant frequencies with opposite signs, which can be filtered with two band-pass filters described above. The multiple off-resonant filtered images can be combined into a single MIP, containing one seed, and colour-coded to visualize each seed individually. We have demonstrated this technique in phantoms containing two seeds with seed-specific positive contrast and compared that to a fully sampled 3D bSSFP sequence, which identified the seed locations with non-specific negative contrast. Additionally, this technique displays better temporal resolution by sacrificing total imaging depth by viewing only the in-plane location of the seeds. Quicker volume coverage was achieved by using thicker slices (>3 mm) as the localization is performed from orthogonal in-plane locations.

Previously, de Leeuw and colleagues [90] used 3D co-RASOR and iterative techniques to visualize LDR brachytherapy seeds and needles. The main difference between our approach and this previous work is prior application of filters to selectively group frequency regions for a particular seed, based on prior knowledge of the seed composition. As seen in phantom validation CNR curves (Fig. 5.6), the CNR from each seed, in all orientations, is maximal in opposing frequency regions, and there is a large enough contrast difference in each frequency region to separate the seeds. For example, while imaging the cross-section (Fig. 5.6a), the brachytherapy seed has global maxima at -600 Hz, but also displays a local maximum at 400 Hz, the same frequency where the GFM contrast is maximal. The difference between CNR is important, as the CNR of the GFM at this frequency is 102, while the brachytherapy seed is 48,

and a threshold can highlight the signals from just the GFM. This behaviour is seen for each orientation and imaging plane where the relative differences between global and local maxima in the same shaded band-pass region are between 1.19 – 3.73. The two worst cases correspond to the long-axis perpendicular to B_0 (Fig. 5.6d) where the relative difference is not as strong and makes thresholding more difficult. These plots also demonstrate that a single cut-off frequency, experimentally determined, is sufficient to isolate the unique frequency ranges.

The applied technique was also performed on a porcine sample where at least one imaging plane correctly differentiated the seeds (Fig. 5.7). When the seeds were imaged parallel to the B_0-field, the surrounding hyperintensities closely matched the symmetric patterns observed in our simulation and phantom studies. We previously demonstrated 2D localization displays plane-dependent hyperintensities about the seeds, either point symmetric or as a dipole pattern [126], and can be reconstructed to positive contrast points. Thus, both planes (top-row Fig. 5.7) are able to reconstruct the seeds at opposing frequency regions. Similarly, even when the seeds are perpendicular to the B_0-field (bottom-row Fig. 5.7), the axial plane also displays the point symmetric pattern that reconstruct to opposing frequency regions. The main difference occurs in the coronal plane where only the LDR brachytherapy seed display symmetric hyperintensities. The GFM hyperintensities occur unequally in the adjacent voxels and off-resonance reconstruction rewinds all points equally. This results in a low-signal smear when performing a MIP across frequency regions, and there is no longer a large positive contrast point. Furthermore, the orientations cannot be directly compared to each other as the LDR signal maxima occurs in the positive frequency MIP (white arrow Fig. 5.7), whereas in all other scans it occurs using a

negative frequency MIP. However, if one plane can correctly identify unique seeds, they can be differentiated as the second plane is used for localization purposes along the orthogonal direction.

While the additional filters to the co-RASOR reconstruction are easy to implement, several limitations should be considered. The SNR in the 2D dual-plane sequence is lower than its 3D version and reduction in contrast is heavily influenced by increased echo-time. Also, the number of acquisition parameters that may influence the degree of signal pileups, such as transmit/receive bandwidth, slice thickness, FOV, and resolution. We attempted to maximize the available transmit bandwidth to incorporate more off-resonance spins, however the remaining parameters still control the pixel shifts of the hyperintensities. Further experimentation to address how these parameters are selected and weighted would be beneficial to ensure pileups rewind to the small areas with high CNR. Our simulations take into account the objects field inhomogneity and shape, so a 3.0 mm cylinder with uniform field inhomogeneity would cause similar effects as a 3.0 mm gold fiducial. In practice, air could be introduced in the tissue during seed implantation. However, air/tissue interfaces are more difficult to simulate due to irregular shapes and non-stationary susceptibility differences. We observed air bubbles in the phantom in Figure 3, as well as an air interface along the needle path left behind in the porcine tissue in Figure 5, though they did not negatively influence the co-RASOR MIPs. We only anticipate issues with air/tissue interfaces if they are directly within the organ of interest and they contain the same flat edges that cause symmetric signal pileups in the image domain.

The choice of frequency cut-off also needs to be experimentally determined. The difference in the range of frequency offsets between our simulations and phantom

experiments is due to bandwidth per pixel. Both images were simulated (or acquired) using the same acquisition window, but the simulations use a FOV that is four times smaller (i.e., 4 cm compared to 16 cm). This implies that the 2000 Hz cut-off would be reduced to 500 Hz when increasing the FOV up to 16 cm. Differences between the realized cut-off of 350 Hz may be that the true susceptibility differences do not match the simulations, or that the signal pileups are blurred over adjacent voxels.

Positive contrast resolution and determining the number of possible seeds that can be visualized was not addressed in this study as the seeds are separated by >3 cm in both phantoms. Clinically, a separation of >1 cm is desired to avoid clustering, though positive contrast resolution is an ongoing area of research. Currently, determining the maximum number of detectable seeds and their spacing has not been explored, and this study restricted itself to viewing just one GFM and brachytherapy seed. This study did not compare against titanium surgical clips, however it may be useful in the future to address more clinical situations. Finally, each seed has a main lobe in its field inhomogeneity, but also contains two half-lobes of opposite sign (Fig. 5.2b) which would reconstruct in the opposing frequency region. This study included signals from these opposing regions which were successfully thresholded away (Fig. 5.6), however it necessitates the inclusion of a threshold that requires manual tuning.

The bSSFP images with negative contrast were also able to depict the seed locations (Figs. 5.5-5.7). Banding artifacts observed can be quite severe (Fig.5.5a, Fig. 5.7a), and depend on the acquisition plane. Our study chose the acquisition plane with the lowest acquisition time for each case. This 3D sequence was chosen as a comparison because of its sensitivity to T2/T1 changes [127] in the vicinity of the seeds to create sharper negative contrast. Furthermore, the use of a high readout

bandwidth attempts to limit the in-plane distortions caused by the seeds.

The proposed method acquires the same data used in conventional co-RASOR imaging, where the frequency filters were applied only during reconstruction. The primary objective of the sequence is to localize seeds with positive contrast, which has previously been explored. To apply this approach clinically, dual-plane co-RASOR can be positioned over the signal voids in orthogonal directions prior to any contrast enhancement studies. Care should be taken to position the planes so they intersect the field inhomogeneity areas created by all of the seeds, as both localization is required in two orthogonal planes for three-dimensional locations. The use of frequency information from each seed would then occur after localization in three dimensions due to the increased reconstruction time of so many off-resonant frequencies. Once accurate localization has been performed, the best imaging plane that displays symmetric hyperintensities about each seed can be used to colour-code the masks if their signal maxima occur in opposite frequency regions. The acquisition time for our sequence was less than the 3D bSSFP by imaging thicker (3.0 mm) orthogonal slices and limiting the through-plane extent to contain the seeds. Undersampled radial acquisitions are also possible beyond a reduction of two used for the porcine tissue in this paper. We expect a reduction factor of 4 to still contain reasonable CNR. This approach clearly aids in differentiating LDR brachytherapy seeds from GFMs.

5.3.5 Conclusion

We demonstrated that specific positive contrast is possible between paramagnetic LDR brachytherapy seeds and gold fiducial markers with a single co-RASOR sequence. The proposed method uses frequency offset filters, where positive contrast

maxima from each seed occur in frequency regions with opposite signs as their magnetic susceptibilities differ in sign. The proposed frequency filtering can create MIPs that display each seed separately, which can then be overlaid and colour-coded to differentiate implanted seeds. This is clinically useful in situations where MR-only simulation is used for combined brachytherapy and external beam radiation therapy.

Acknowledgments

This project was supported by an Ontario Graduate Scholarship (OGS) to EM. The authors also thank the financial contributions by Robert Dunsmore that made the work possible.

Chapter 6

Resolution and Registration in Dual-Plane co-RASOR MR

6.1 Context of Paper

In this study, undersampled 2D dual-plane co-RASOR images of gold fiducial markers were simulated and also acquired in order to measure their resolutions when displayed with positive contrast using off-resonant signal processing. These were then assessed as to whether the co-RASOR sequence or a conventional Cartesian-based 3D bSSFP sequence (currently used clinically to localize fiducials), displays a bias relative to CT as a ground truth. Finally, we attempted to measure the fiducial localization error of gold fiducial markers, by measuring their target registration error relative to a set of externally placed fiducial markers.

We hypothesized that using external fiducial markers to register MR and CT images would allow us to independently measure GFM as target points. As these metallic objects cause geometric distortions as a result of field inhomogeneity, their

locations cannot be assumed as truth, and a rigid body registration using the GFMs may be biased. We used a MR-compatible Lego phantom to assess any bias in localizing known target points, before measuring the unknown GFM locations. We discovered that the positive contrast resolution is on the order of 0.5 mm, which matches the total variance in MR to CT registration. Furthermore, we measured target registration error of GFMs to be <0.75 mm, which can be used as an indirect measurement of localization error when using GFMs for tracking and registration.

6.2 Declaration Statement

Evan McNabb acquired the data, performed the data analysis, interpreted results, and drafted the manuscript text. Additionally, he created the manuscript figures, and tables. The contributions by Evan McNabb warranted his name as first author.

Dr. Michael Noseworthy, as corresponding author, designed this project as multidisciplinary biomedical engineering project as part of his years of expertise in the field of Magnetic Resonance as well as developing engineering applications to serve clinical needs. He provided critical analysis of the methodology, interpretation of results, and manuscript revisions of the final article that he submitted for publication. Finally, he provided thorough guidance and helped secure funding resources.

Dr. Raimond Wong conceptualized the clinical rational for this project based on his expertise as an interventional oncologist. He provided the clinical materials used for research, provided guidance in tailoring the engineering principles to clinical outcomes. Finally, he also secured funding resources.

This paper has been submitted to Physics in Medicine and Biology, June 7, 2018.

6.3 Paper

Registration Accuracy and Resolution of Dual-Plane co-RASOR MRI

Evan McNabb[1], Raimond Wong[2-4], Michael D. Noseworthy[1,5-7*]

[1]McMaster School of Biomedical Engineering, McMaster University, Hamilton, Canada
[2]Juravinski Cancer Centre, Hamilton, Canada
[3]Department of Oncology, McMaster University, Hamilton, Canada
[4]Department of Medicine, McMaster University, Hamilton, Canada
[5]Imaging Research Centre, St. Joseph's Healthcare, Hamilton, Canada
[6]Department of Electrical and Computer Engineering, McMaster University, Hamilton, Canada
[7]Department of Radiology, McMaster University, Hamilton, Canada
[*]Corresponding author at: Department of Electrical and Computer Engineering, McMaster University, Engineering Technology Building, ETB-406, 1280 Main St. W, Hamilton, Ontario, Canada, L8S 4K1. Email: nosewor@mcmaster.ca

Abstract

Magnetic resonance imaging (MRI) has superior soft tissue contrast and lower interobserver variability compared to computed tomography and advances in equipment and pseudo-CT estimation have allowed for MR-only radiation therapy planning. Dedicated MR sequences have been used to localize paramagnetic structures with positive contrast, and most implanted seeds are gold fiducial markers (GFMs). We used a fast, dual-plane co-RASOR sequence to localize implanted GFMs with positive contrast in phantom and tissue to assess their resolution and registration accuracy of registration to CT. Off-resonant reconstructions of co-RASOR images were able to resolve GFMs down to 5 mm apart at 12 cm FOV. No systematic biases were observed by comparing registration of co-RASOR and bSSFP to CT images in an MR-compatible Lego phantom with a set of highly visible known points. The standard deviations

of the MR to CT distance errors were <0.5 mm in all directions. We separated the component due to registration by comparing the two MR sequences, which had a maximum standard deviation of 0.36 mm in the SI-direction. Registration using the positive contrast points in a porcine sample phantom showed increased errors, but co-RASOR still performs acceptably with a target registration error of <0.75 mm. The dual-plane co-RASOR sequence could then be used for both registration and image tracking when performing MR-only radiation therapy planning.

Key Words: positive contrast, localization, gold fiducial markers, co-RASOR, image registration, MR simulation

6.3.1 Introduction

The use of magnetic resonance imaging (MRI) with image guided radiation therapy reduces interobserver variability in delineating dominant lesions from organs at risk [74, 114, 128, 129]. Additionally, its superior soft tissue contrast over computed tomography (CT) and its functional information allows better targeted dose escalation, thus boosting therapeutic efficacy [130–132]. Misregistration of CT and MR images creates uncertainties that cascade throughout the planning procedure, which can be systematic and up to 2 mm [71–73]. Performing MR-only radiation therapy planning can remove the uncertainties of MR to CT registration, and new techniques such as using flat bed MR simulators (MRsim) with the patients in therapy position, coil advancements that conform to patient geometries, and atlases to create pseudo-CT images for electron densities, have allowed groups to fully implement MR-only planning [17–19].

Localizing implanted metallic devices with positive contrast has been explored to aid in MR-only therapy planning [88, 120]. Most positive contrast techniques have been compared using paramagnetic structures, e.g. brachytherapy seeds, or super-paramagnetic particles [89, 90, 119, 121, 122, 133, 134], whereas the implanted fiducial markers are composed of gold. However, several techniques have been explored to localize gold fiducial markers (GFMs), such as combined multi-parametric models [124], magnetic susceptibility models [125], and template matching algorithms [85, 87]. The geometric accuracy of the template matching and multi-parametric methods have also been assessed relative to CT as ground truth, with fiducial distances reported as <1 and 2 mm, respectively.

One advantage of the co-RASOR sequence is the ability to quickly acquire data on-resonance, and a single reconstruction parameter, the frequency offset, can be used to generate positive contrast by rewinding signal pileups from any magnitude of magnetic susceptibility [96]. Furthermore, we see areas of improvement in assessing the geometric accuracy of positive contrast techniques by comparing a set of points in MR and CT images that were not used as part of image registration, or relying on mutual information. We propose to use externally placed fiducial markers, visible in both CT and MRI, such that the implanted metallic fiducial markers are the measured targets. Reporting the distance errors of the points used for image registration, known as the fiducial registration error (FRE), is common in literature. However, these variances may be statistically independent to those derived from points not part of image registration, known as the target registration errors (TRE), [135].

The aim of this study was twofold: to assess the resolving capability of the dual-plane co-RASOR sequence of GFMs in order to determine how closely the fiducials

can be distributed, and to assess the geometric accuracy of the sequence. We attempt to measure any bias in two MR sequences, a 3D bSSFP and dual-plane co-RASOR, compared to CT. Finally, we measure the TRE of GFMs by using a set of known fiducial markers to create a rigid body transformation between imaging modalities, allowing us to estimate the localization error when using GFMs.

6.3.2 Materials and methods

6.3.2.1 Resolution Simulations

Field perturbers were simulated with diameter 1.0 mm, length 3.0 mm, and a magnetic susceptibility difference $\Delta\chi = -25$ ppm to approximate the physical properties of a GFM [125]. Three simulated GFMs and their field inhomogeneity patterns were shifted by $(-\delta_x, -\delta_y)$, $(+\delta_x, -\delta_y)$, and $(-\delta_x, +\delta_y)$ relative to the image centre, respectively. To separate them equidistant in the x- and y-directions, shift values were selected as $\delta_x = \delta_y$ in both the axial and coronal planes, as shown in Figure 6.1. The images were then Fourier encoded onto centre-out k-space (FOV = 4 cm, 10 slices, thickness = 4 mm, 128x128 matrix) with the ΔB_z errors included to simulate the mis-registered spins, appearing as hyperintensities. Image reconstructions were performed using a non-uniform Fast Fourier Transform (NUFFT) [103], implemented in MATLAB R2014b (The Mathworks Inc, Natick, MA). Images were then reconstructed off-resonant by multiplying each k-space readout by a linear phase ramp, with frequency offsets up to 1 kHz in 25 Hz increments. A single optimal frequency offset was selected by subtracting each off-resonant image by the on-resonant image for background suppression, followed a maximum intensity projection along the offset frequencies. The optimal offset was selected as the maximum value in the MIP. The

GFM shift values were chosen to display three cases: i) no overlap in the hyperintensities (Figures 6.1a,b), ii) marginal overlap in the hyperintensities (Figures 6.1c,d), and iii) severe overlap in hyperintensities (Figures 6.1e,f). These values were 7.5, 2.5, and 1.25 mm in the axial plane, and 10.0, 7.5, and 2.5 mm in the coronal plane. It's apparent that even with marginal overlap in the on-resonant images, there still exists a separation where the off-resonant images can correctly resolve the fiducials with positive contrast.

To further explore where positive contrast off-resonant images are no longer resolvable, simulations were also performed using FOV values of 4, 12, 16, and 20 cm corresponding to resolutions of $\Delta_x = 0.3125$, 0.9375, 1.25, and 1.5625 mm, respectively. GFMs were initially separated by 2 cm, and reduced up to, and including the point, where they were no longer resolvable. Images were reconstructed off-resonance, and a single optimal frequency offset was once again selected. A line profile was created in the x- and y-directions through the off-resonant images at the appropriate shift value, and a 50% threshold was applied to measure the FWHM of each GFM in both planes. The FWHM separation in each direction was measured if there were exactly two peaks, otherwise the separation was set to zero and reported as a failure to resolve each marker.

6.3.2.2 Resolution Experiments

MR images were acquired using a 3T GE Discovery MR750 (General Electric Healthcare, Milwaukee, WI) with maximum gradients of 50 mT/m and 200 T/m/s slew rate, using a 32-channel head coil. The gold seeds were diamagnetic GFMs (IZI Medical Products, MD, USA) with diameter 1.2 mm and length 3.0 mm. Three GFMs

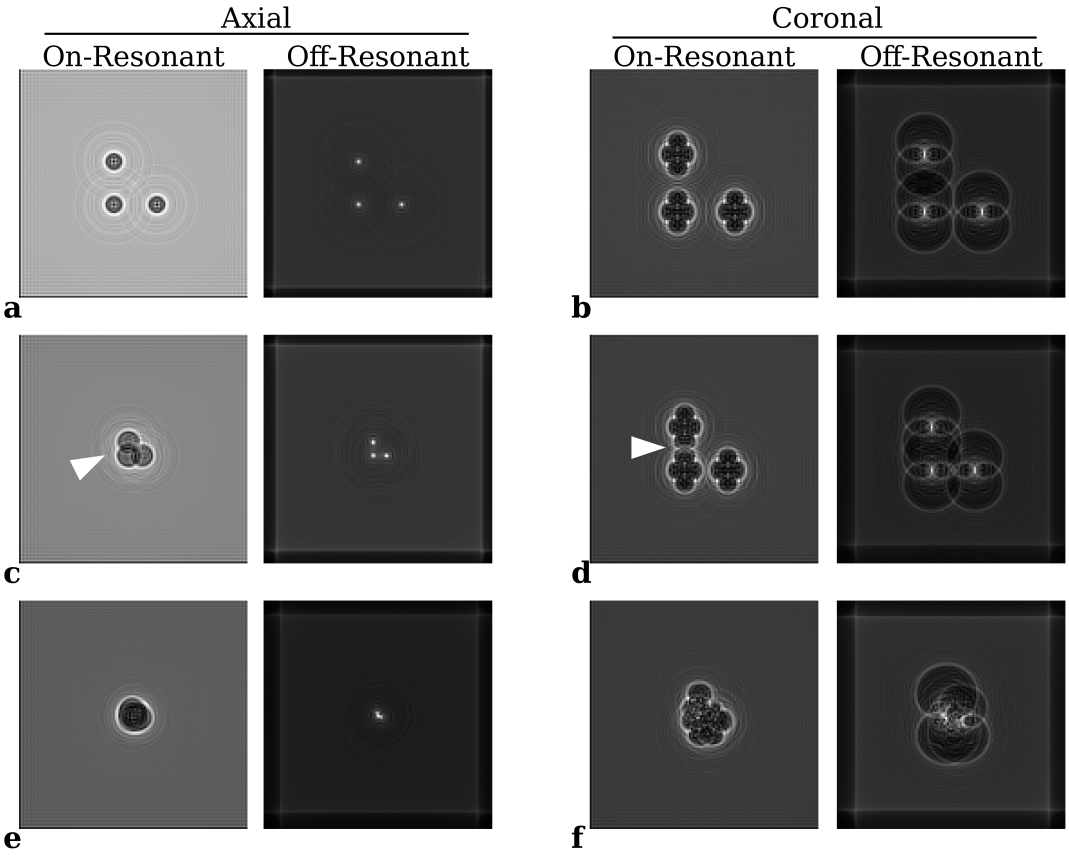

Figure 6.1: Simulated GFMs shifted equidistant in the x and y-directions (FOV = 4 cm). Three cases presented are: separations of 7.5 and 10 mm in the axial and coronal directions that display no overlap between hyperintensities **(a,b)**, 2.5 and 7.5 mm separations displaying marginal overlap between hyperintensities (denoted by white arrows) where GFMs are correctly resolvable in off-resonant images **(c,d)**, and 1.25 and 2.5 mm separations displaying severe overlap where GFMs are no longer resolvable **(e,f)**.

were placed in 3% gel phantoms, where the centre of the seeds were separated by 0.5, 1.0, and 2.0 cm in orthogonal directions, oriented parallel to the B_0-field. All seeds were imaged co-planar to each other, where the axial resolution was measured as the separation of the cross-sections of the seeds, and coronal resolution was measured as the separation of the longitudinal axis. A 3D bSSFP (TE/TR = 2.3 / 9.3 ms, bandwidth = 976 Hz/pixel, 256x256, 38 slices, thickness = 2.0 mm, NEX = 1, $\alpha = 35°$, acquisition time = 1:41) was used to image the entire volume of interest to depict the seeds with negative contrast with respect to background. The dual-plane co-RASOR sequences (TE/TR = 2.7 / 100 ms; thickness = 3.0 mm; 256x804 matrix; bandwidth = 244 Hz/pixel, acquisition time = 0:43 each) were scanned orthogonal in the axial and coronal planes. Slice selection was performed with a one-cycle SINC pulse (transmit bandwidth = 4.4 kHz; duration = 904 μs) in order to minimize echo time and intravoxel dephasing. Each phantom was imaged at 12, 16, and 20 cm FOV.

All co-RASOR data was acquired on-resonance, with linear phase ramps modulating each k-space spoke by δf prior to image reconstruction in 25 Hz increments. The ranges used were 0 - 1 kHz for the axial images and -650 to 650 Hz for the coronal images to ensure the hyperintensities rewind to the smallest areas possible. Maximum intensity projections were taken across the offset frequencies for visual identification of the seeds. Each image was masked by first removing all voxels below an image threshold that maximized interclass variance between background and foreground [136], followed by subtracting the on-resonance image from each frequency offset. Resolution was determined by thresholding by 50% of the image intensity and evaluating whether the three FWHM areas were uniquely visible.

6.3.2.3 Registration Experiments

The geometric accuracy and fiducial localization accuracy of the 3D bSSFP and dual-plane co-RASOR sequences were assessed by using CT as ground truth using an MR-compatible Lego phantom (ONDRI, Ontario, Canada), composed of 9.6 mm Lego pieces rigidly connected to an exterior cylindrical case. The phantom was oriented such that the Lego interfaces occur in the SI-direction. All CT images were acquired using a Siemens Biograph 16 PET/CT scanner (Siemens, Erlangen, Germany). The CT imaging protocol consisted of 3D axial images (FOV = 240 mm, 256x256 matrix, 256 slices, 120 kV, 200 mAs). MR imaging consisted of a 3D axial bSSFP (FOV = 24.0 cm, thickness = 1.0 mm, 192 slices, $\alpha = 30°$, acquisition time = 3:37) sequence and dual-plane co-RASOR (FOV = 24.0 cm; 256x804 matrix; 6 slices, $\alpha = 30°$, acquisition time = 1:21 each) sequence.

The phantom exterior was outfitted with four fiducial markers (Beekley Corporation, Bristol, CT, USA) that generate contrast in both imaging modalities, and were used to perform rigid body registration (Figure 6.2). The 3D coordinates of N=32 targets were selected in the CT images, with N=16 being located in each of the MR acquisitions. Each MR sequence was registered to the CT space by a rigid body transformation defined by the external fiducial markers. Target registration error (TRE) was assessed as the distance between CT coordinates and their respective transformed MR coordinates. To separate variance due CT - MR registration, we also compared the TRE between both MR sequences using a new set of N=16 points, as there was no motion between successive MR scans of the phantom. A t-test was performed on the TREs in X, Y, and Z-directions to determine whether the bSSFP or co-RASOR sequences display a non-zero mean relative to CT. Similarly, a

second t-test was performed on the difference between bSSFP and co-RASOR coordinates without registration in order to observe any bias and measure the variance in localizing the points within the MR images.

Finally, in a study approved by our local animal care committee, three GFMs were injected into porcine muscle tissue using a needle and guiding wire. The porcine tissue was obtained from a local food market. Each GFM was separated such that the shortest interseed distance was approximately 1 cm. The tissue was then placed in a container with external fiducial markers. The porcine sample phantom was imaged with seeds parallel to B_0, using an axial bSSFP (16.0 cm x 19.6 cm, α =10°) for a scan time of 6:37. The dual-plane co-RASOR images (FOV = 16.0 cm; thickness = 4mm) were acquired undersampled by a factor of 2 (402 spokes) in the axial and coronal directions, covering 32 and 28 mm respectively, for a scan time of 0:43 each. The bSSFP and co-RASOR images were registered to CT using a rigid body transformation between the external fiducial markers, located in the CT and bSSFP images. The GFMs were located in all three image sets, and the TREs were calculated between CT - bSSFP and CT - co-RASOR registrations.

6.3.3 Results

6.3.3.1 Resolution Experiments

Measured FWHM separations of simulated GFMs compared to known separations are shown in Figure 6.3. For the axial plane (Fig. 6.3a), the hyperintensities are point-symmetric and measurements are equal in both directions. Each FOV contains one failure point when the simulated separations were 1.25, 1.8, 2.5, and 3.125 mm for FOV values 4, 12, 16, and 20 cm respectively. These failures corresponds to pixel

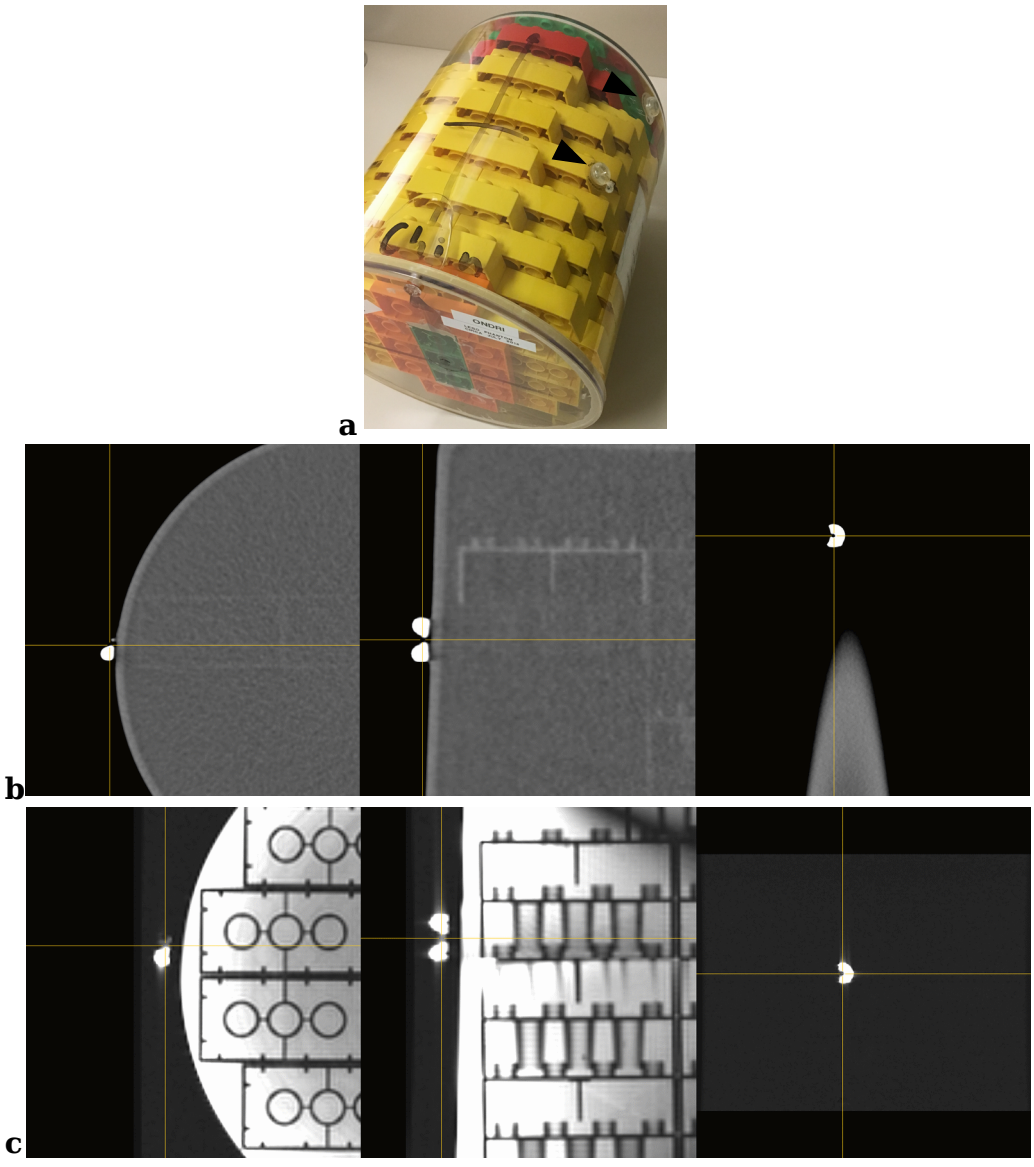

Figure 6.2: MR-compatible Lego phantom rigidly connected to cylindrical case used to assess geometric accuracy **(a)**. Attached to the surface are four external fiducial markers (two shown by black arrows) in order to perform a rigid body registration. The external fiducial markers are located in three planes in the CT **(b)** and MR **(c)** images.

shifts $4\Delta_x$ at FOV = 4 cm and $2\Delta_x$ for the rest, which is the minimum separation needed as each fiducial occupies three pixels at FOV = 4 cm, and one pixel at the other scales. The short axis x-direction in the coronal plane (Fig 6.3b) displays more failure points up to 5 and 6.2 mm for FOVs 16 and 20 cm. The long axis y-direction in the coronal plane (Fig 6.3c) contains one failure point at the 20 cm FOV. The shaded region corresponds to areas where GFMs were overlapping. Deviations away from the dashed line correspond to localization errors as the positive contrast points are measurable, but separated by incorrect distances.

Images from the axial and coronal co-RASOR MIPs of three GFMs separated by 0.5 - 2.0 cm are shown in Figures 6.4 and 6.5, respectively. Positive contrast for the GFMs are seen through the MIPs for each of the separations, and is most evident at the higher resolution images (FOV = 12 cm). For each of the separations, as the field of view increases towards 20 cm, the total extent of the hyperintensities increases, obscuring the visibility of the seeds at lower resolutions.

The contrast of the GFMs is explored further in Figure 6.6 at 0.5 cm separation for both planes. The 3D bSSFP images were acquired in two orthogonal planes, and the coronal acquisition displays reduced banding artifacts. Comparing axial bSSFP and co-RASOR, the bSSFP displays negative contrast and identifies all three seeds, and the co-RASOR images can be masked to display positive contrast at only the seed locations. Similarly, the coronal bSSFP images display negative contrast, however the signal voids have merged together in the SI (y)-direction. The co-RASOR masks, however, can display each of the seeds with positive contrast.

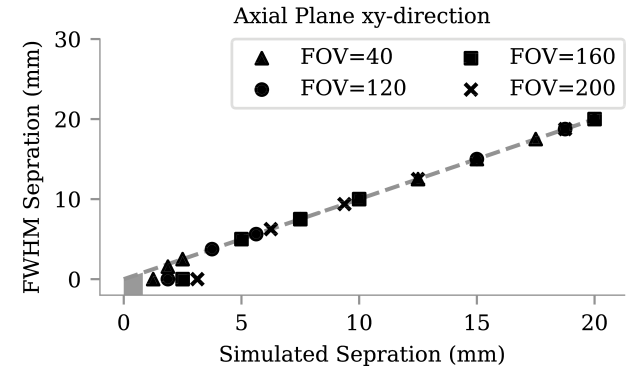

a

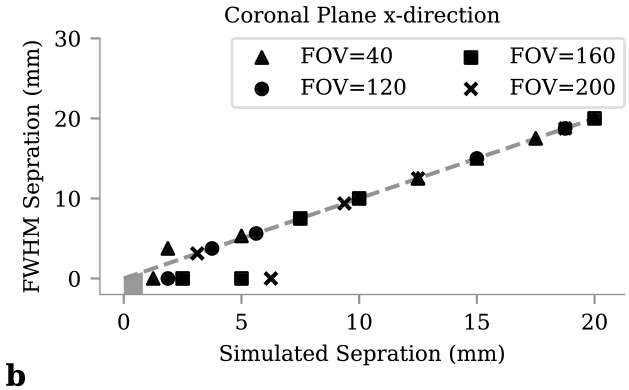

b

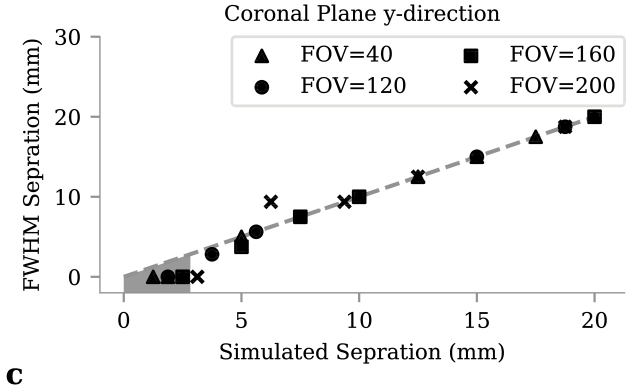

c

Figure 6.3: Measured FWHM separations of simulated GFMs at field of views 4, 12, 16, and 20 cm at shift values up to 2 cm for the axial **(a)**, coronal x-direction **(b)**, and coronal y-direction **(c)**. A FWHM separation reported as zero represents a failure to detect exactly two peaks along this direction. The shaded regions represent areas where the GFMs are overlapping and not possible to resolve.

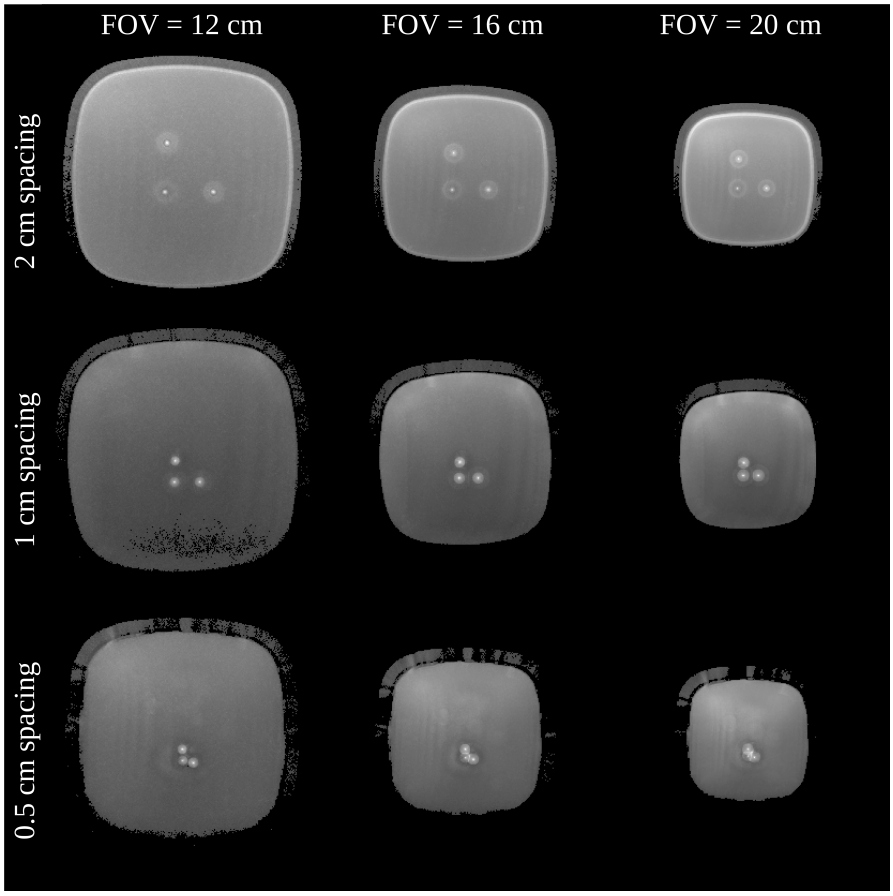

Figure 6.4: Axial 2D co-RASOR MIPs highlighting the positive contrast for GFMs at separations of 2 cm, 1 cm and 0.5 cm at field of views 12 cm, 16 cm, and 20 cm. Without masking, seeds are visible with positive contrast when separated by at least 1 cm.

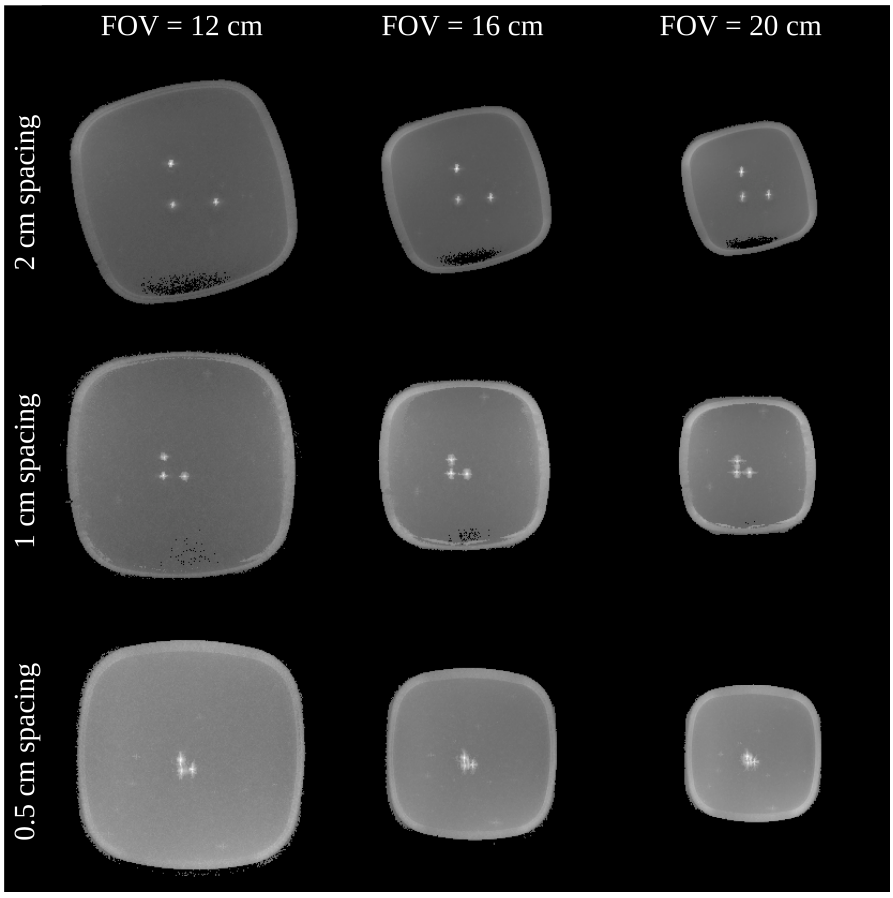

Figure 6.5: Coronal 2D co-RASOR MIPs highlighting the positive contrast for GFMs at separations of 2 cm, 1 cm and 0.5 cm at field of views 12 cm, 16 cm, and 20 cm.

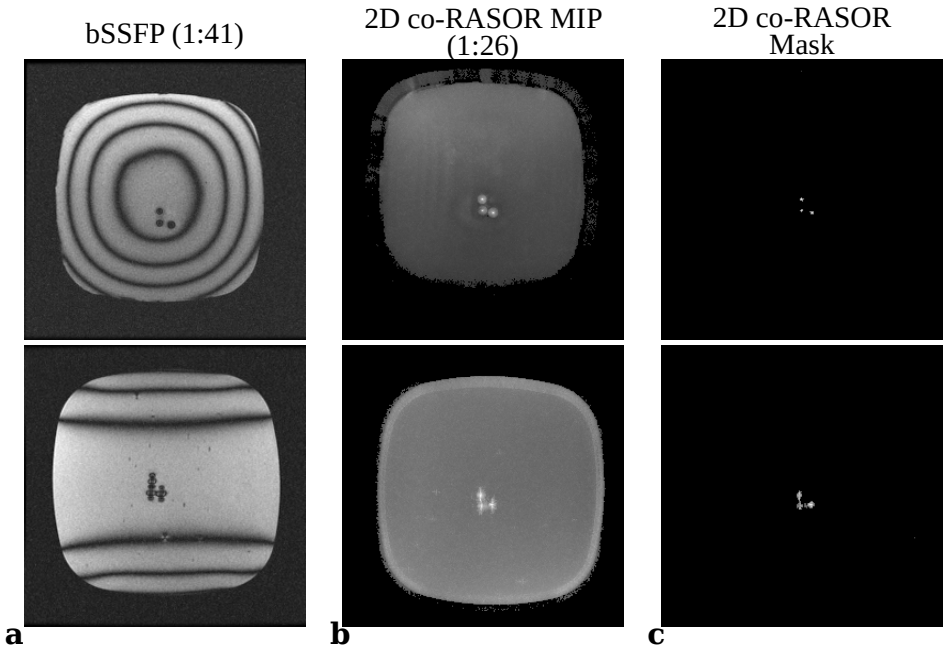

Figure 6.6: Comparisons between negative contrast bSSFP **(a)**, dual-plane co-RASOR MIPs **(b)**, and co-RASOR masks **(c)** of three GFMs that are separated by 5 mm in the RL and AP-directions (top-row, axial plane) and 5 mm in the RL and SI-directions (bottom-row, coronal plane). Masking and 50% threshold was able to detect all three GFMs in both planes.

6.3.3.2 Registration Results

All four external fiducial markers of the Lego phantom were located in both CT and the 3D bSSFP sequences and were used for registration of the subsequent MR images. MR coordinates were transformed to the CT coordinate space, and the following distance errors are reported using the Right-Anterior-Superior (RAS) coordinate system. The transform rotation parameters were $[\theta_x, \theta_y, \theta_z]^T = [0.36°, -1.04°, -0.98°]^T$, the median FRE values were -0.124, -0.026, and 0.084 mm, and RMSE of the FRE values were 0.131, 0.009, and 0.259 mm in the X, Y, and Z-directions, respectively. A total of N=16 targets were acquired for both sequences, with examples shown in Figures 6.7a,b, highlighting axial and coronal localization of the CT and MR images. Box plots of the TRE values are shown for the 3D bSSFP and co-RASOR sequences (Figures 6.7c,d). Statistics of the TREs are further detailed in Table 6.1. Comparisons of the mean, standard deviation, and RMSE reveal that each sequence has comparable errors, with the bSSFP targets ranging from -0.104 to 0.128 (std. 0.400 - 0.435) mm, and the co-RASOR targets ranging from 0.091 - 0.204 (std. 0.334 - 0.458) mm. A t-test of the TREs in each of the 3D directions demonstrated that there was no non-zero mean bias of the errors in any of the directions ($p > 0.05$). Table 6.2 shows the TRE between the bSSFP and co-RASOR sequences without any registration. The mean, standard deviation, and RMSE is reduced in all directions.

The three GFMs inserted into the porcine sample phantom were localized in the negative contrast bSSFP and positive contrast co-RASOR images, shown in Figure 6.8. A single GFM in the bSSFP is shown for both planes by the white arrow, where the contrast is more difficult to discern in the coronal plane. The positive contrast of each seed is evident in the MIP images through the frequency offsets

CT-MR Target Registration Errors

	CT - $\mathbf{T}(\mathrm{MR_{bSSFP}})$			CT - $\mathbf{T}(\mathrm{MR_{co\text{-}RASOR}})$		
	X	Y	Z	X	Y	Z
Mean	-0.104	0.128	-0.100	0.157	0.091	0.204
Std.	0.400	0.435	0.422	0.334	0.394	0.458
RMSE	0.400	0.440	0.425	0.359	0.392	0.488
p-value	0.313	0.258	0.356	0.079	0.371	0.095

p-value < 0.05 used for t-test in each direction.
$df = 15$

Table 6.1: Target registration error (TRE) statistics, reported in mm, of an MR compatible Lego phantom comparing the distance errors of CT coordinates to the transformed MR coordinates of bSSFP and dual-plane co-RASOR sequences.

(highlighted by the white box) in both planes. The transform rotation parameters were $[\theta_x, \theta_y, \theta_z]^T = [-3.03°, 1.76°, 0.42°]^T$, the median FRE values were -0.182, -0.036, and 0.078 mm, and RMSE of the FRE values were 0.267, 0.127, and 0.244 mm in the X, Y, and Z-directions, respectively. The seeds were selected in the CT images, and pairwise TREs between the CT to bSSFP, and CT to co-RASOR registrations are shown in Figure 6.9. The mean TRE values for the bSSFP registration were 0.307, -0.818, and 0.131 mm, and the values for the co-RASOR registrations were 0.026, -0.505, and 0.2596 mm, in X, Y, and Z-directions, respectively.

6.3.4 Discussion

This study assessed the resolution and registration of GFMs using the MR-based dual-plane co-RASOR sequence that relies on signal pileups in the vicinity of the seeds in centre-out radial acquired data, which can be rewinded into localized areas with high positive contrast. The sequence was compared to CT localization, as well as to MR-CT registrations involving a 3D bSSFP sequence. The resolution of three GFMs

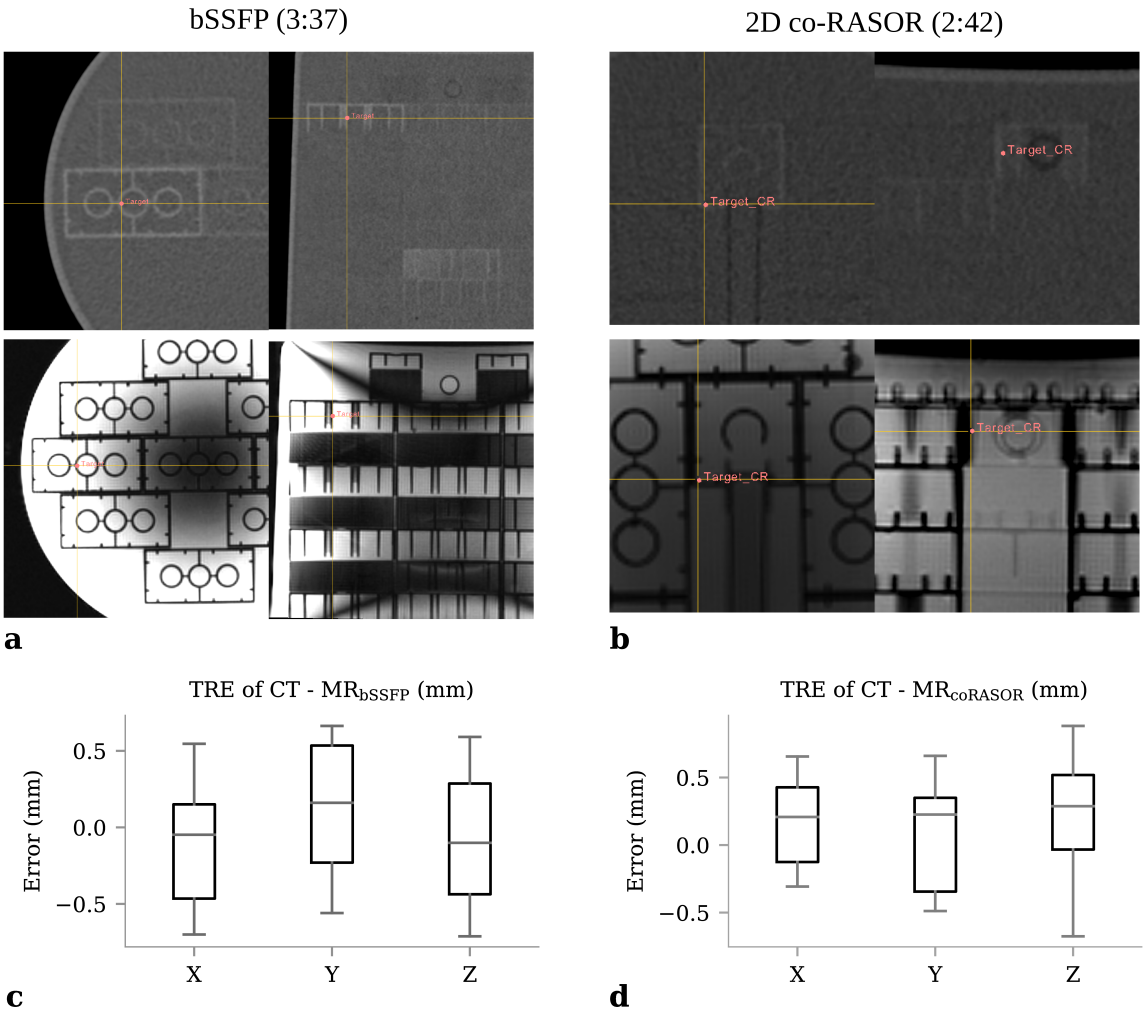

Figure 6.7: Target localization using the axial and coronal planes of Lego pieces comparing CT (top-row) and a bSSFP sequence **(a)** and dual-plane co-RASOR sequence **(b)**. Target registration errors (N=16 points) are shown for each of the X, Y, and Z-directions for the bSSFP **(c)** and dual-plane co-RASOR **(d)** sequences.

MR-MR Target Registration Errors

	MR_{bSSFP} - $MR_{co\text{-}RASOR}$		
	X	Y	Z
Mean	0.011	-0.134	0.146
Std.	0.219	0.271	0.3413
RMSE	0.213	0.263	0.361
p-value	0.842	0.845	0.111

p-value < 0.05 used for t-test in each direction.
$df = 15$

Table 6.2: Target registration error (TRE) statistics, reported in mm, comparing the distance errors of the bSSFP and dual-plane co-RASOR sequences.

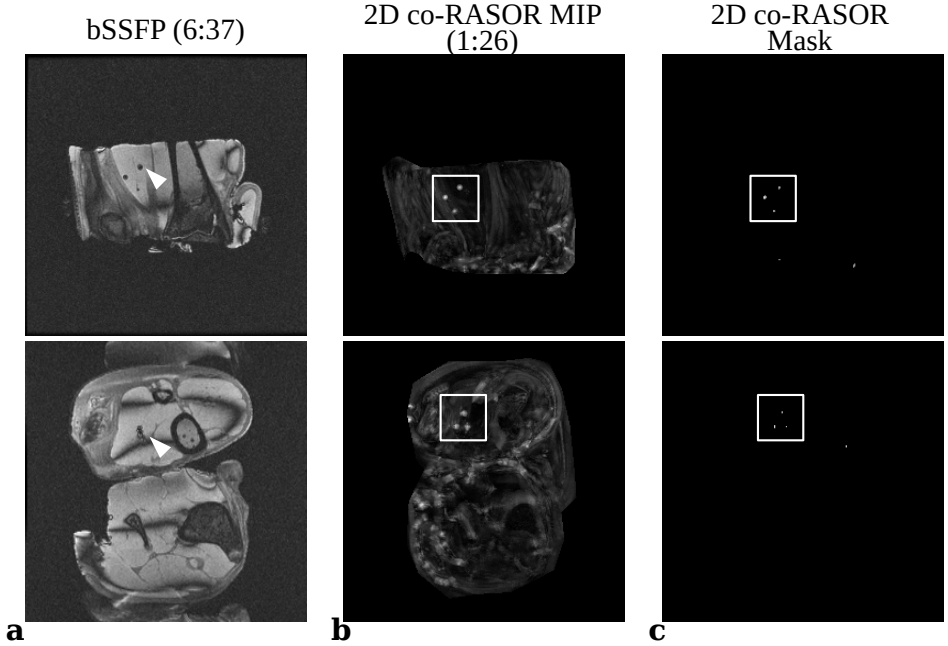

Figure 6.8: Comparisons between negative contrast bSSFP **(a)**, dual-plane co-RASOR MIPs **(b)**, and co-RASOR masks **(c)** of three GFMs inserted into a porcine sample phantom. The white arrows on the bSSFP correspond to the same GFM in both planes. The white box surrounding the GFMs in the co-RASOR images show the high positive contrast in both planes. Masking is able to identify each GFM at specific voxels.

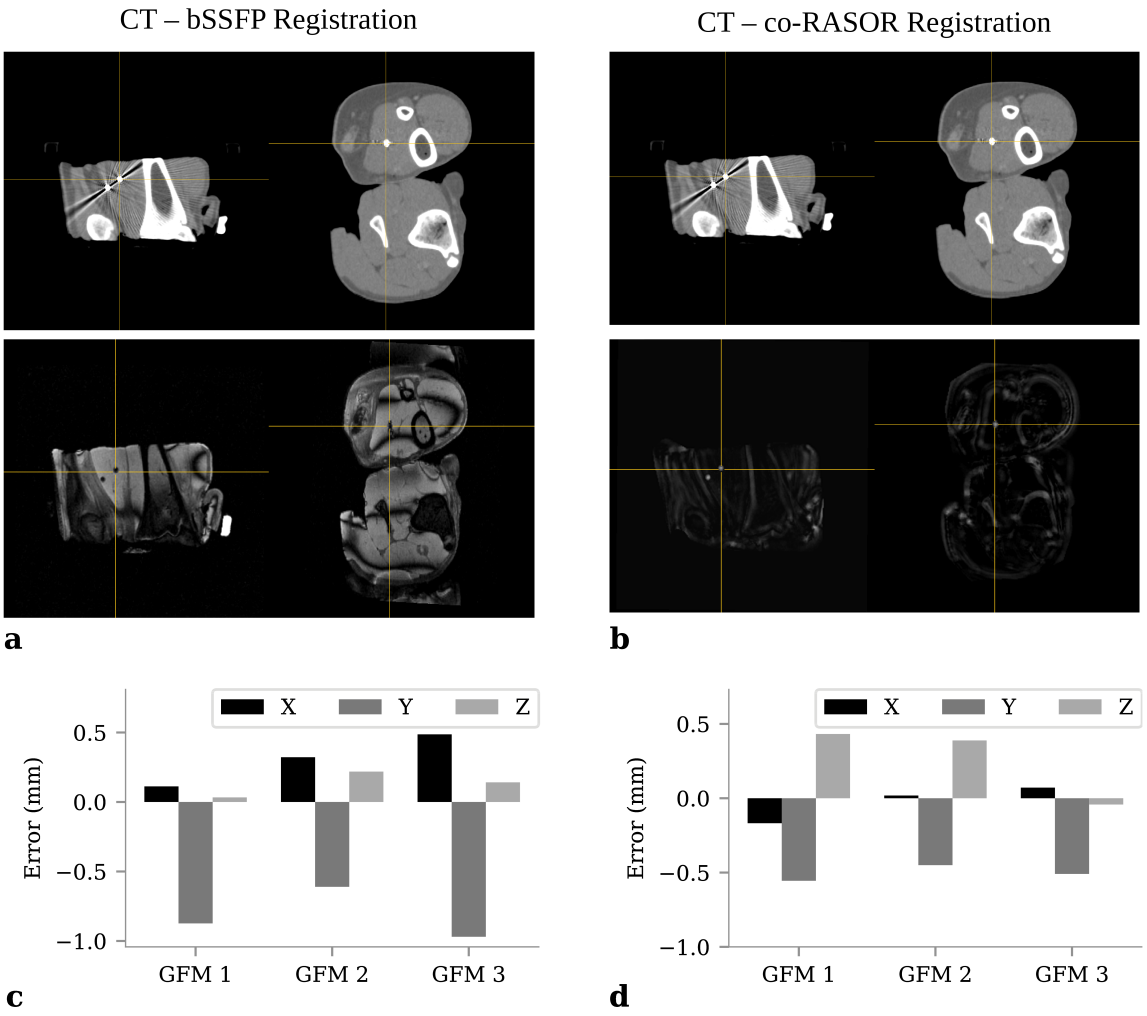

Figure 6.9: GFM localization using the axial and coronal planes of a porcine sample phantom CT (top-row) and a 3D bSSFP sequence **(a)** and dual-plane co-RASOR sequence **(b)**. Target registration errors of the three GMFs are shown for each of the X, Y, and Z-directions for the bSSFP **(c)** and dual-plane co-RASOR sequences **(d)**.

was measured by the FWHM separation in both the axial and coronal planes. The minimum resolvable GFM separations were 5 mm at a 12 cm FOV, and 1 cm at larger FOVs. The dual-plane co-RASOR and 3D bSSFP sequences displayed no systematic bias when compared to CT, with total TRE errors < 0.75 mm and not greater than 0.5 mm in any of the three directions of an MR-compatible Lego phantom. Additionally, there was no bias between each MR sequence. Finally, we assessed TRE of three GFMs in a porcine sample phantom, with TRE values < 0.75 mm. The uncertainties in these measurements relate to geometric distortions in MR imaging [137, 138], and in registration to CT [72, 73]. The biases were tested using known points inside the phantoms, and were registered to the CT images using high contrast external fiducial markers in order to reduce the initial registration uncertainties.

Generating positive contrast enhances the visibility of each marker relative to background, and also aids in masking voxels by simple thresholding. Some studies have looked at sequence independent parameters, such as $R2^*$and $|\Delta B_0|$ values, multi-echo GRE sequences, or parameter optimization of clinical sequences, to best visualize GFMs with negative contrast [139–141]. While markers are visible if their background has sufficiently high SNR, it typically takes manual observation over multiple sequences in order to visualize all markers present. Additionally, marker specificity requires larger signal voids thereby lowering resolution with other markers and nearby hypointense structures, and involves multiple trade-offs in parameter selection that may unavailable depending on the initial application.

This study was the first, to date, to apply the co-RASOR method to GFMs and assess how close markers can be placed before their positive contrast signals are no longer resolvable. Our simulations show that some degree of overlap in on-resonant

signal pileup artifacts can be resolved to unique points down to GFM separations of 5 mm (Figure 6.1), except in two cases when imaging the long-axis of the GFMs spaced at 5 and 6.25 mm for 16 and 20 cm FOVs (Figure 6.3). Phantom results corroborate the simulations, as GFMs are resolvable up to 5 mm using the smaller 12 cm FOV, but fail in the coronal plane at 16 and 20 cm respectively (Figures 6.4, 6.5). A comparison between the 3D bSSFP and dual-plane co-RASOR sequence at GFM separations of 5 mm (Figure 6.6) shows that positive contrast can be generated with co-RASOR MIPs, which display higher visibility compared to the 3D bSSFP. The fiducial locations can also be masked by thresholding the co-RASOR MIPs. The bSSFP sequence also shows appreciable banding artifacts, which can obscure the fiducial location near hypointense structures and would inhibit masking by image intensity alone. An second example of masking is shown in Figure 6.8 for a porcine sample phantom, where the GFMs are highly visible in the MIPs which leads to positive contrast masking. The GFMs used in this study, however, were larger at 1.0 mm diameter and 3.0 mm length compared to those reviewed by Gurney-Champion et al., and Tanaka et al., which compared varying marker shapes and sizes ranging from 0.28 - 0.6 mm and 0.35 - 0.5 mm diameters, respectively [139, 142]. Their results indicate that marker size plays a role in visibility, so co-RASOR would need to be tested on a larger set of GFMs in future studies.

Similar to Maspero et al., and Dinis Fernandes et al., we also compared localization error with respect to CT as the ground truth. The differences between our studies were that we used externally placed fiducial markers on the surfaces of our phantoms to perform rigid-body registration instead of using the GFMs as the fiducial point set, or using mutual information, respectively. These external fiducials are highly visible

in both modalities (Figure 6.2), and aid in reducing fiducial localization error. Using the GFMs as the point sets for registration, and measuring the distance errors of the coordinates, measures FRE instead of TRE and their variances may be independent [135]. For example, the FRE between CT and bSSFP MR images of the Lego phantom had lower RMSE values than any of the TREs described in Tables 6.1 and 6.2. Registration involving mutual information can also be problematic if the reduced contrast in CT limits the amount of information available to the metric. While this technique is comparable to fiducial-based registration for post-implant brachytherapy planning, as observed in Figure 6.7, not all of the Lego pieces are visible, which limits the principle benefit that mutual information offers in matching all local information [143].

To assess the geometric accuracy of the bSSFP and co-RASOR sequences, we first attempted to measure any biases in targeting points in both the bSSFP and co-RASOR sequences relative to CT. We used a phantom containing Lego, rigidly connected to an exterior cylindrical case in order to choose known points, not subject to any signal processing present in localizing GFMs. Gradient non-linearity will be present within both MR sequences, however, their differing sequence timings and gradient switching mean that geometric distortions due to eddy currents may differ between them. We selected N=16 unique points to measure the distance errors between corresponding pairs of points in CT and bSSFP, CT and co-RASOR, and bSSFP and co-RASOR images. Figure 6.7 shows an example of targeting a point using orthogonal views between CT and bSSFP and CT and co-RASOR, along with the box plot TRE errors for each CT - MR registration. Table 6.1 shows that TRE values range from -0.104 to 0.128 mm and 0.091 to 0.204 mm for the bSSFP and

co-RASOR registrations, respectively. A t-test was performed on the TRE values in each direction of the 16 points, and no significant differences from zero-mean were observed ($p > 0.05$). The standard deviation values in our study are less than 0.5 mm, which corresponds to the minimum resolvable marker. Similar values were observed in previous studies, that also found no bias between CT-MR registrations of markers and TREs were all less than 1.2 mm, respectively [87, 124]. One difference is that we used distance errors and not intermarker distances, as there is evidence of marker migration between fractions that will change this metric [81]. Additionally, we assessed target errors between MR-MR images to separate uncertainties from localizing pairs of points between a pairs of images, and from the uncertainties caused by registration misalignment. Table 6.2 shows these TRE statistics, where the standard deviation, ranging from 0.219 to 0.341 mm, thereby allowing an estimate of localizing known points.

We also assessed the geometric accuracy of three GFMs in a porcine sample phantom and found the median registration errors ranged from -0.873 to 0.322 mm for the bSSFP sequence and -0.509 to 0.389 for the co-RASOR sequence (Figure 6.9). These increased from the Lego phantom, despite comparable FRE between both external fiducial markers. The higher errors in the bSSFP sequence occur mainly in the AP-direction, which corresponds to the frequency encoding direction. The field inhomogeneity is known to cause pixel shifts in this direction. We used a high bandwidth sequence (> 900 Hz/pixel), and the co-RASOR frequency offset corresponded to about 600 Hz, which means we may experience approximately 70% pixel shift, or 0.450 mm displacements in the frequency encoding direction of the bSSFP sequence. The co-RASOR have lower error measurements, as the normalized error never exceeds

0.75 mm.

Several limitations should be reviewed for this study. First, we used only a single type of GFM throughout the study. The co-RASOR sequence is sensitive to field inhomogeneity causing signal pileups and can rewind them to smaller areas. This works best, however, if the signal pileups follow a symmetrical pattern, as the off-resonance frequency offsets rewind in the radial direction equally. GFMs that are curved or contain multiple materials (i.e, gold and titanium, or gold and platinum) may alter the field inhomogeneity patterns and appear non-symmetric, which will reduce CNR when rewinded. Secondly, the GFMs were always placed parallel to the B_0-field. Changing the orientation also changes the signal pileup patterns. However, similar patterns are expected when imaged perpendicular to B_0 and should not impact the ability to differentially resolve the seeds. Future studies should consider varying the orientations as this is expected in clinical placement of the GFMs. Another limitation is measuring any non-zero biases in the registration with only 16 points. The previous studies mentioned used a greater number of measured fiducials, however given the variances listed, there is enough power to measure separations past 0.5 mm ($1 - \beta > 0.99$) and 0.28 mm ($1 - \beta \approx 0.8$) with this sample size. While the registration errors were acceptable for the co-RASOR to CT registrations (< 0.75 mm), it's difficult to estimate the fiducial localization error without a larger set of points, which is of great interest as the GFMs themselves are used for image guided tracking and MR to CT registrations. The relative low TRE values can also be aided by smaller FOV values, where gradient nonlinearities are expected to be minimal. Further studies should include a larger set of measured target GFMs to build up variance measurements. Finally, co-RASOR is a dedicated pulse sequence that would

need to be added to clinical protocols. The timing to acquire the dual-planes was 1:26 min, however higher radial undersampling could be explored.

6.3.5 Conclusion

We used a fast, dual-plane co-RASOR sequence to localize implanted GFMs with positive contrast in phantom and tissue to assess their resolution and registration values. Simple image thresholding can create a series of co-RASOR mask, and GFMs are resolvable up to 0.5 mm with smaller FOVs. The artifact patterns created by the field inhomogeneity was the limiting factor in resolving each seed, and was greater than the resolution of the co-RASOR images. No systematic biases were observed by comparing co-RASOR to bSSFP and CT images in a Lego phantom with a set of highly visible known points. The standard deviation of MR to CT registrations was <0.5 mm, and was reduced when comparing the two MR sequences at 0.219 to 0.361 mm. Registration using the positive contrast points in a porcine sample phantom shows increased errors, but co-RASOR still performs acceptably with a median TRE of <0.75 mm. The co-RASOR sequence can be performed in approximately 90 seconds, and leads to accurate localization with high positive contrast that can be integrated into MR-only radiation therapy planning for registration and tracking purposes.

Acknowledgments

This project was supported by an Ontario Graduate Scholarship (OGS) to EM. The authors also thank the financial contributions by Robert Dunsmore that made the work possible.

Chapter 7

Dual-Plane co-RASOR Fiducial Masking

7.1 Introduction

Image reconstruction of non-Cartesian MR pulse sequences typically involves offline reconstruction, as direct Fourier inversion is not possible. This is because non-uniform FFT and iterative reconstructions both involve a regridding step to interpolate the acquired readout samples onto a Cartesian grid. This necessitates using external libraries written in C/MATLAB for each 2/3D k-space raw data, and combining multichannel images into a final magnitude image.

Compounding the complexity is the fact that offline image reconstruction may produce images that are not as geometrically accurate as online MR reconstruction. Vendors employ gradient warping correction, as the gradient nonlinearities are often the most dominant source of geometric distortion. For the purposes of fiducial localization, images reconstructed offline may display highly localized positive contrast,

but the objects may suffer from geometric distortion which may not be readily apparent since the co-RASOR images are reconstructed both off-resonance, changing the overall contrast over the entire image domain, and then post-processed to display only the fiducials.

Another source of complexity to fiducial localization comes from alternative sources of field inhomogeneity, such as chemical shifts and air/tissue interfaces. As the co-RASOR sequence is sensitive to off-resonant spins due to field inhomogeneity, and not imaging metal devices directly, these extra sources may display positive contrast in addition to fiducial markers. Maximum intensity projections are typically performed over the off-resonant frequencies and image slices for a pair of orthogonal masks. However, the intensity threshold is still a manual parameter for each reconstruction.

We attempted to address these challenges in a two-fold manner. First, by utilizing the gradient warping correction for offline Cartesian reconstruction. Secondly, as the dual-plane co-RASOR shares a common axis between two orthogonal planes hyperintensities from a set of N fiducials should share N positive contrast locations along this common axis. This may aid in masking the signals from only the fiducial markers and produce more consistent masks.

7.2 Materials and Methods

An example of maximum intensity thresholding through off-resonant frequencies for three simulated gold fiducial markers is shown in Figure 7.1 highlighting the offline reconstruction of co-RASOR images using off-resonant frequencies. The proposed modifications to the reconstruction pipelines are shown in Figures 7.2 and 7.3 for gradient warping correction and dual-plane fiducial localization techniques. In Figure

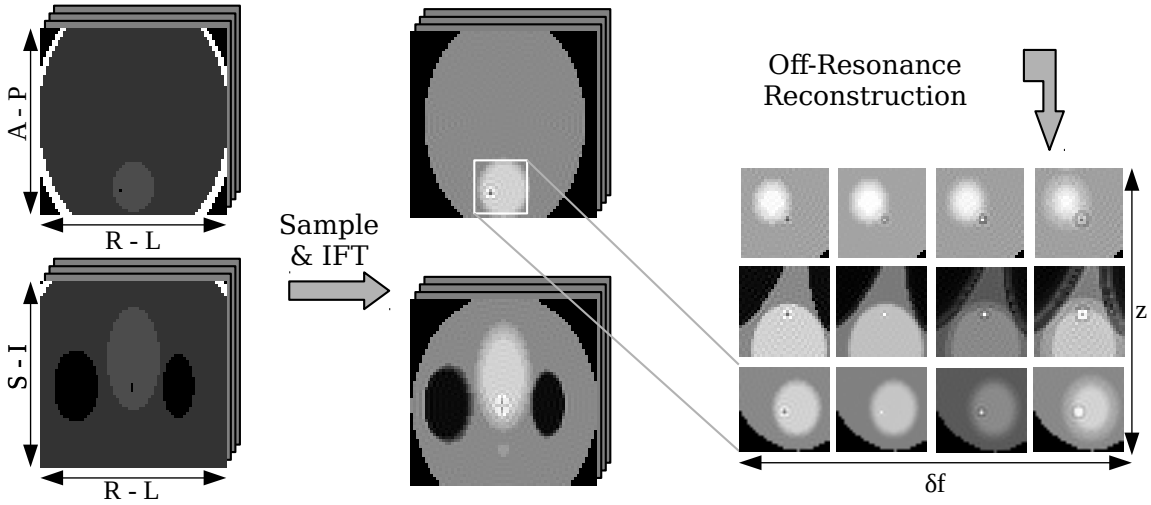

Figure 7.1: Three simulated GFMs in a digital phantom. Each slice contains a third dimension of off-resonant frequencies, where a maximum intensity threshold is applied once the on-resonant slice is subtracted to maximize signal from each fiducial.

7.2, the offline Cartesian reconstruction is shown in the left-most column. Gradient warping correction and image orientation (i.e., applying the physical locations to each voxel) was applied to each uncorrected image slice before producing a final image that is geometrically accurate and contains the correct physical coordinate system. The methods themselves use compiled libraries written by General Electric Healthcare and are scanner dependent. These methods would be applied to online reconstruction on the MR console before writing images to DICOM files. However, if raw data samples are radially acquired, the IFT step produces nonsensical images. We replaced these images with standard uncorrected co-RASOR images, and match the same slices. In this manner, each co-RASOR slice can take advantage of the gradient warping correction and have image orientations applied so that physical coordinates can be used in subsequent analysis.

In Figure 7.3, once the MIPs have been performed through the off-resonant frequencies and each slice, two masks are created. Off-resonant effects near the edges

of objects can also appear, and the choice of threshold parameter requires careful tuning to avoid these areas. To avoid this limitation, we performed a separate MIP along the SI-direction in the axial case, and AP-direction in the coronal case to see a set of two line profiles that share the common RL-direction as their axis. In this manner, data was shared between each orthogonal view along a common axis, and point matching could thus be performed. This helped to eliminate points not common between axis, and create a common set of hyperintense point locations. Finally, the co-RASOR masks were enhanced by backprojecting only the RL-locations along the SI- and AP-directions, respectfully.

The proposed method was tested using three GFMs that were injected into porcine muscle tissue, obtained from a local food market, with a needle and guiding wire and were approximately separated such that the shortest interseed distance was approximately 1 cm. The porcine sample phantom was imaged with seeds parallel to B_0 using a dual-plane co-RASOR sequence (FOV = 16.0 cm; thickness = 4mm). co-RASOR images were acquired undersampled (402 spokes) in the axial and coronal directions, covering 32 and 28 mm respectively, for a scan time of 0:43 each.

7.3 Results

Off-resonant reconstruction was performed on the axial and coronal co-RASOR sequences of the porcine tissue sample phantom and is shown in Figure 7.4a. The typical intensity masks with a colour overlay, and their respective masks are shown in Figures 7.4b,c and show increased areas of hyperintensities around the edges that cannot be removed by simple intensity thresholding, without removing the fiducial markers as well.

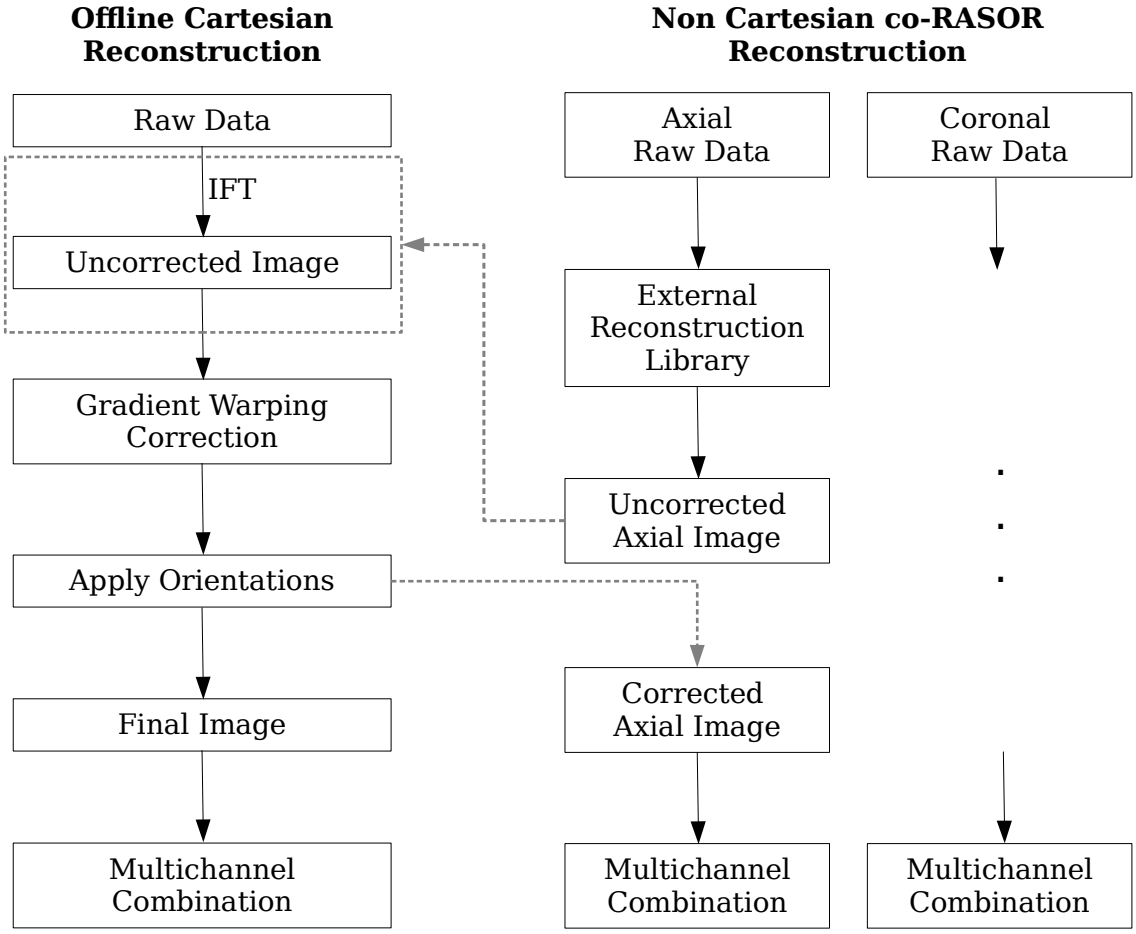

Figure 7.2: Gradient warping correction applied to Non-Cartesian reconstruction. Each process was performed independently, however the dashed lines show where image replacements were done. The external reconstruction library step is not a fixed library, it can be projection reconstruction, NUFFT, or iterative methods.

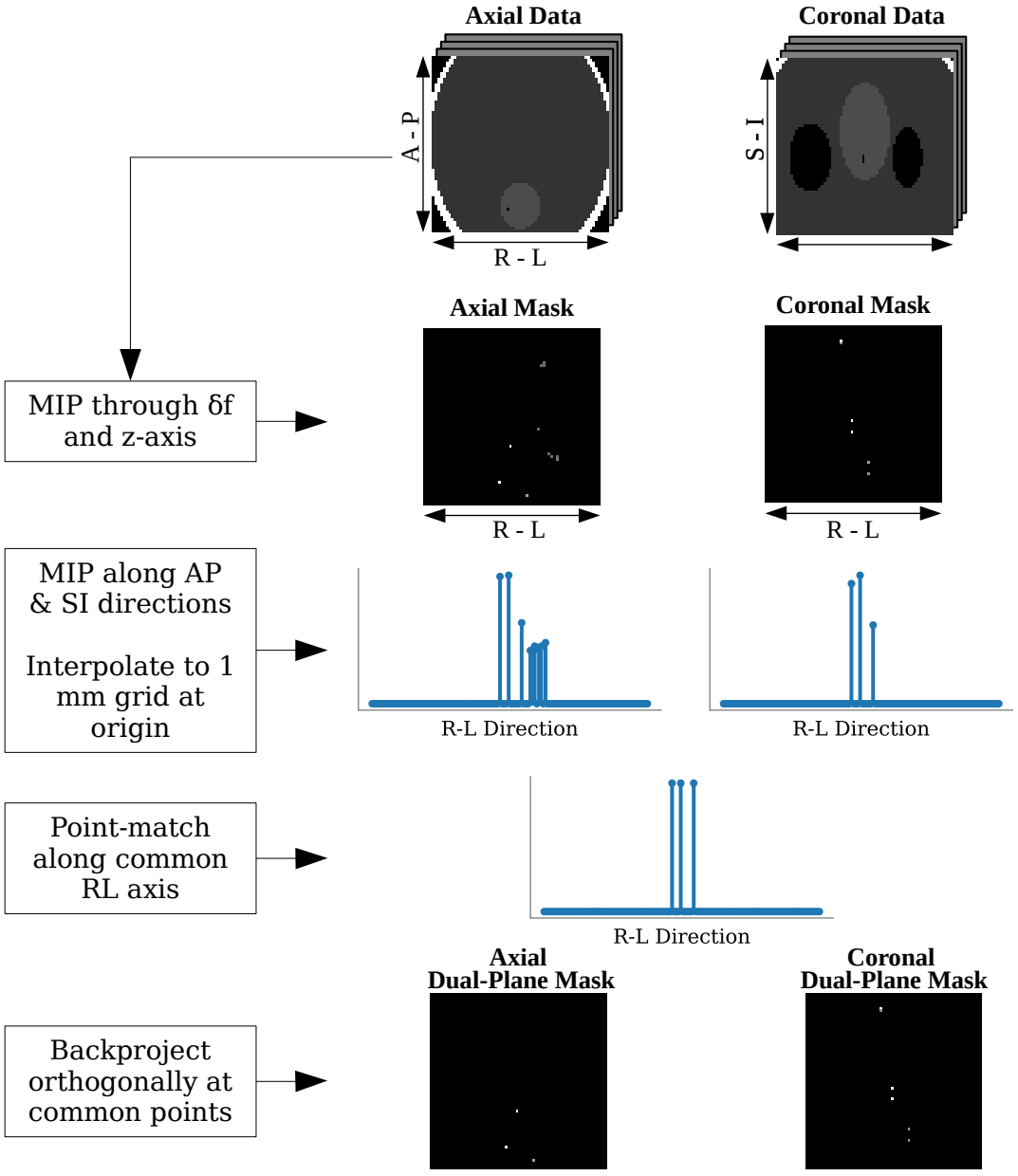

Figure 7.3: Fiducial localization masking utilizing a common axis between orthogonal planes. Separate MIPs were performed over each mask that have hyperintensities along a common axis. This information was used to enhance the original co-RASOR masks along only points that are shared between both RL-axis.

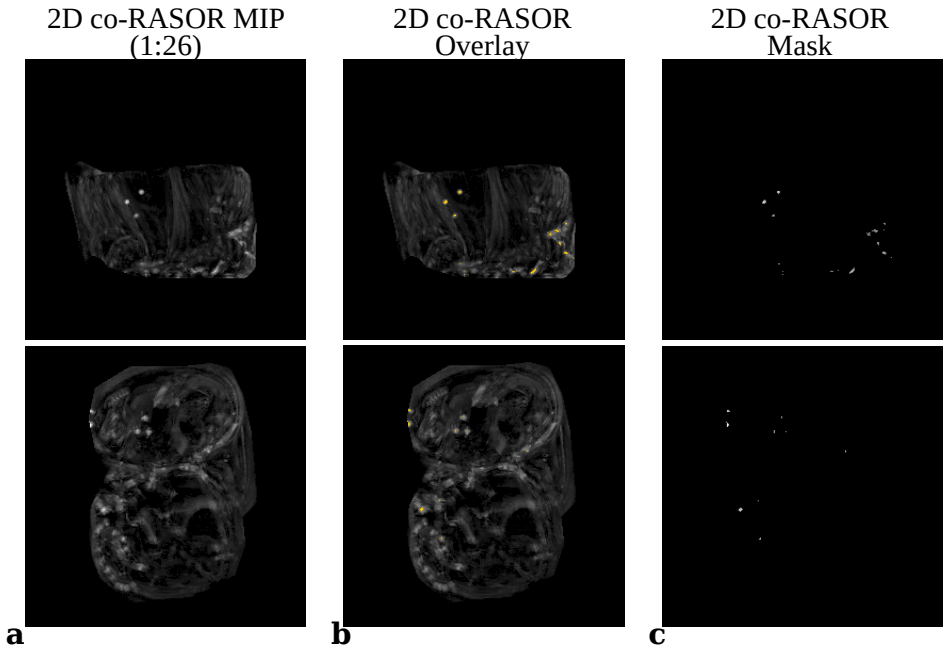

Figure 7.4: co-RASOR MIP through the frequency offsets and z-direction in the axial (top-row) and coronal (bottom-row) planes of a porcine tissue sample with three implanted GFMs **(a)**. An intensity based threshold overlay is shown **(b)** along with the corresponding 50% threshold mask **(c)**.

The MIP in the SI-direction for the axial co-RASOR image, and AP-direction for the coronal co-RASOR image create line profiles that share a common RL-axis, shown in Figures 7.5a,b. The GFM hyperintensities were located at approximately -20 mm relative to the MR origin. An overlapping region showed a reduction in edge effects, as the number of overlapping voxels was much less compared to each individual direction.

The final colour overlays of the proposed method using dual-plane masks are shown in Figure 7.6. There are some edge effects remaining in the axial case, however the number has been reduced relative to the intensity masks. Similarly, the coronal case shows the location of each of the GFMs (highlighted by the zoomed inlet) as well as a single remaining hyperintensity along the edge.

7.4 Discussion

The proposed method applies geometric correction and applies the image orientation positions in order to create DICOM files that are similar to online reconstruction from the MR console, only applied to Non-Cartesian acquisition. The physical coordinates are then used in a second algorithm to perform MIPs orthogonal to the common axis shared by each of the dual-plane co-RASOR sequence. In this manner, only shared hyperintensities are reconstructed to the final output masks.

We applied the algorithms to a numerical simulation of three GFMs and to a porcine tissue sample phantom in Figure 7.3 and Figures 7.4-7.6 respectively. The numerical example was thresholded at 25% of the image intensity to include hyperintense areas along the edge in the axial case, and a MIP was performed over the SI-direction to make a line profile. The coronal image shows each of the three fiducial

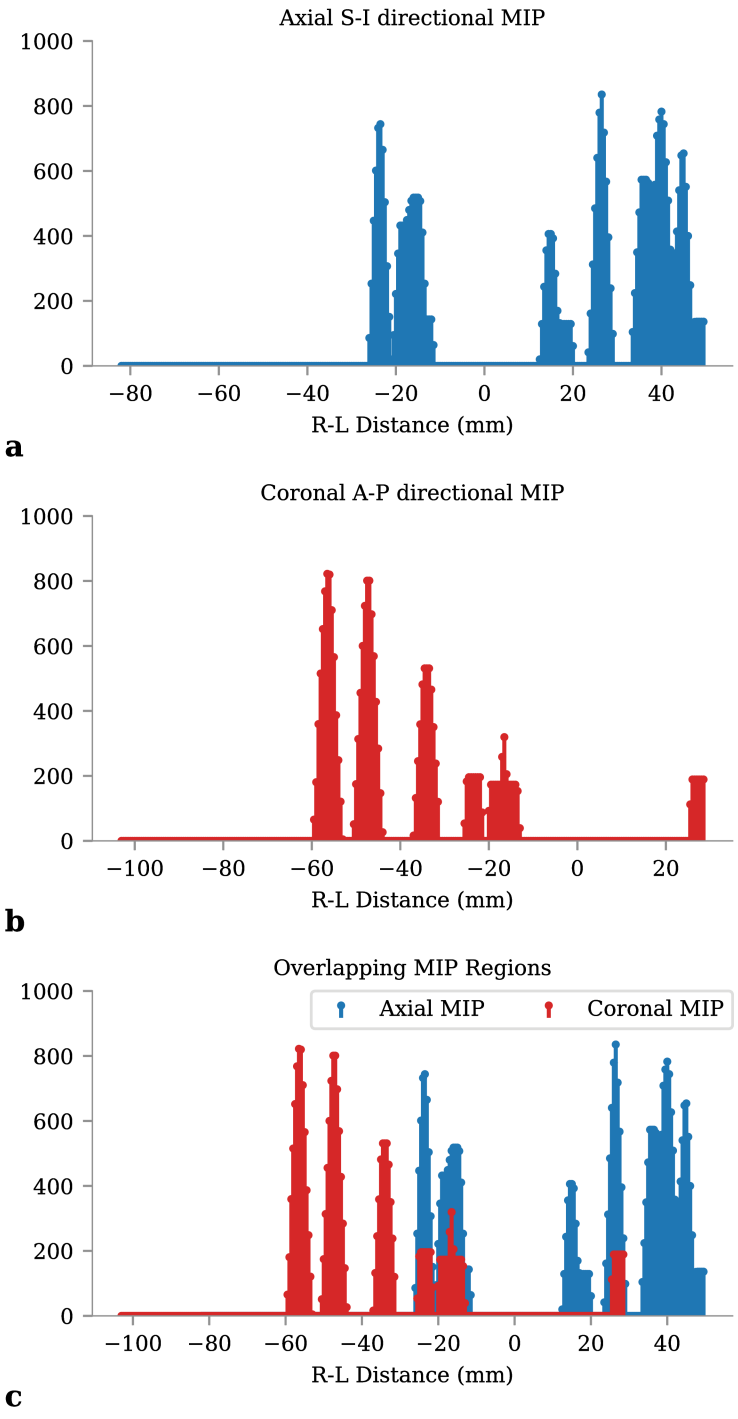

Figure 7.5: MIPs in the SI-direction **(a)**, AP-direction **(b)** in physical coordinate locations along the RL-axis. The areas overlapping hyperintensities **(c)** correspond to common positive contrast points in the dual-plane co-RASOR MIPs and are kept in the final masks.

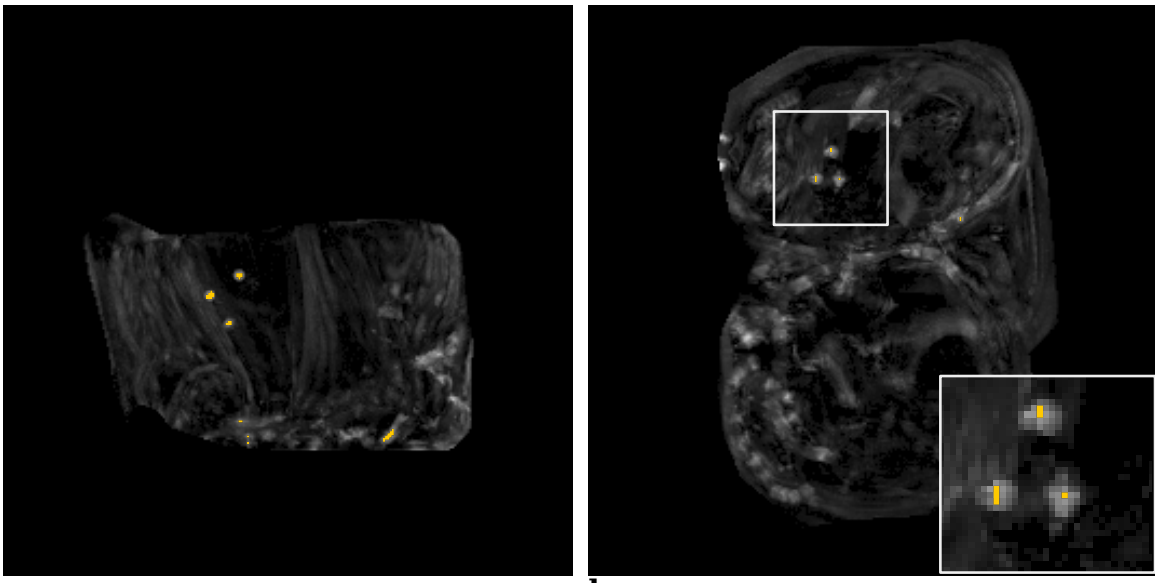

Figure 7.6: Axial **(a)** and coronal **(b)** colour overlays of the same porcine tissue sample with the proposed method to correct for geometric distortion and dual-plane co-RASOR masks of common RL-direction locations.

markers, and a MIP over the AP-direction shows the RL coordinates of the three fiducials. We then used the physical locations along the RL-axis and backprojected these areas to the original axial mask to exclude hyperintensities that were not along orthogonal lines in the SI-direction. This process was applied to the tissue phantom, however the threshold was increased to 50% of the image intensity for the original masks in Figure 7.4. When we performed MIPs in each direction shown in Figure 7.5a,b, there were hyperintensies along the RL axis. The fiducials themselves occupy only a small area, centred about -20 mm. When the plots were overlapped in Figure 7.5c, the number of positive contrast points in the axial line profile was reduced from 91 points to 33 points, and the number of positive contrast points in the coronal line profile was reduced from 71 to 26 points. This is approximately a reduction of 2.75x in each plane, and the remaining positive contrast points mainly come from just the

fiducial markers, as shown in Figure 7.6.

One limitation of this technique is that if there are hyperintensities in the original masks that occur above or below the fiducials in the SI- and AP-directions. Since these common areas are backprojected along lines at specific RL coordinates, they are still included in the final masks. This is seen in the axial case of the tissue phantom in Figure 7.6a, where there is positive contrast point along the edge below the three fiducial markers. Since it occurs in the same RL-location it could not be excluded. A way to address this problem would be to include the through-plane information from each dual-plane acquisition instead of performing a MIP over the z-directions. For example, a 3 mm slice in the axial plane corresponds to a 3mm area in-plane when viewing coronal images. However, the complexity of this approach increases with imaging extent as far more point matching comparisons need to be performed.

In conclusion, we can increase the specificity of dual-plane co-RASOR masks by matching positive contrast points along the in-plane shared axis between axial and coronal views of an object. As the acquired axial and coronal planes share a common RL-axis, the positive contrast points are limited to only those matching spatial locations along the RL-direction. Three fiducial markers were inserted into a tissue phantom, and the positive contrast masks maintain the fiducial locations, but significantly reduce the number of positive contrast points along the edges, which are also sensitive to off-resonant effects.

Chapter 8

Conclusions and Future Directions

8.1 General Remarks

A dual-plane co-RASOR sequence based on radial signal pileups that can be rewinded to the field perturbing objects provides positive contrast between gold fiducial markers and surrounding areas. Field inhomogeneity due to the magnetic susceptibility differences between metal and tissue causes ^{1}H spins to resonate at incorrect frequencies, mis-registering the locations of the reconstructed spins to similar spatial locations, causing signal pileups around these markers. This signal model can take advantage of some key properties. Firstly, the modified sampling scheme over Cartesian imaging means the centre of k-space, the Fourier conjugate of the image domain, is sampled more densely and requires less spokes to define a good approximation of the object. Secondly, with addition of prior knowledge regarding composition of the implanted seeds, the off-resonant frequency offset appears to be an indicator of the sign and magnitude of different magnetic susceptibilities.

Currently, MR localization of fiducials relies on multiple sequences that display

negative contrast of the seeds over volumes much larger than the size of the seed. The experiments in this thesis show that a single MR acquisition can be used for localized positive contrast, and scalable frequency offsets can be used to tune the contrast without relying on multiple acquisitions, or information from prior sequences or template libraries. In these studies, the reconstruction techniques, susceptibility encoding into the signal, resolution of multiple fiducials, and their registration accuracy were all explored.

8.2 Main Findings

The co-RASOR sequence can successfully be implemented using an undersampled acquisition, resulting in fewer spokes and TR-cycles. In addition, 2D encoding can take advantage of time between the data readout and the end of TR-cycle, and perform encoding on a range of slices, reducing acquisition time. We found that high positive contrast can be achieved in as little as 6 seconds per slice for a single fiducial, or using multiple slices with an effective encoding of 1.4 s/slice. Higher resolutions were performed compared to similar 3D co-RASOR studies, and we exceeded the temporal resolution while imaging at the expense of total coverage. This is a reasonable strategy because an isotropic 3D k-space matrix is not required in 2D imaging, and thicker slices can be used to localize only the in-plane locations with high CNR. As the hyperintensity patterns change relative to the acquisition plane, it was expected that the difference planes will have different CNRs. This was indeed the case, as measured in simulations and phantoms, with the coronal plane displaying a 10% reduction in contrast. We also found that NUFFT, which simply combines the undersampled

reconstructions of each coil channel, had reduced CNR compared to the iterative techniques using a TGV2 penalty and CG-SENSE. An important result, however, followed that increasing the CNR can be achieved at the cost of blurring. CG-SENSE had the highest CNR for most undersampling factors, but displayed higher FWHM areas which would cause blurring of the localized fiducial, and in some cases the FWHM areas were nearly double the fully sampled areas. Experiments using undersampled co-RASOR should avoid CG-SENSE due to the blurring effect, and if CNR is a limiting factor, the TGV2 penalty displayed higher CNR values compared to NUFFT, without large increases in the positive contrast area.

Applying the co-RASOR sequence to different compositions of metallic seeds was explored. We found that signals at the geometric centres of seeds were maximal using opposite signed frequency offsets, in the cases that the seeds were diamagnetic and paramagnetic, respectively. Numerical simulations showed that a colour coded mask can be overlayed onto the typical co-RASOR MIP images to display each seed individually, without additional acquired information. Simple frequency filters were applied to mask out the signal from each seed, which was localized into one half of the frequency offset range for both acquisition planes, and two different orientations with respect to the B_0-field. A seed sometimes produced a local maximum from a different offset range, which may interfere with the contrast mechanism. We found that the relative difference between the global maxima in each frequency range, compared to a local maxima from other seeds were between 1.19 – 3.73 using CNR measurements. The contrast mechanism was applied to phantoms and tissue samples, highlighting each seed individually.

We also explored the differentiable resolvability of the co-RASOR sequence to determine how close together seeds can be placed before they are no longer uniquely resolvable. An important result was found through simulations that the seeds were not uniquely resolvable at their minimum separations, and in all cases needed at least one pixel spacing between them. This limited the minimum separations to approximately 5 mm, although in some FOVs the minimum separation was 6.25 mm. We corroborated these results in phantoms, where the seeds were moved closer together from 2 cm to 0.5 cm. We found that at smaller FOVs, 5 mm separation is capable of resolving all three seeds. However, at FOVs of 16 cm and greater, this was not possible, and the minimum separation is between 5 mm and 1 cm. The registration accuracy of the co-RASOR sequence was also assessed using external fiducial markers placed around a MR-compatible phantom to perform a rigid body transformation between CT and MRI sequences. Target registration errors, measured as the distance between CT and transformed MR coordinates ranged from -0.104 to 0.128 mm and 0.091 to 0.204 mm for the bSSFP and co-RASOR sequences, respectively. No significant differences from zero-mean were observed for either sequence. Following this, the registration accuracy of positive contrast fiducials was assessed, and co-RASOR outperformed a 3D bSSFP sequence, where the normalized TRE does not exceed 0.75 mm. co-RASOR appears to be a high contrast sequence to localize fiducials with standard deviations in geometric accuracy on the order of 0.5 mm. This approximately matches its resolving capability.

8.3 Limitations

The main limitation of these studies in translating results to MR simulation comes from the lack of human participants available. The methodology works very well in simulations and phantoms, though there is more difficulty in separating positive contrast signals due to implanted fiducials and other off-resonant sources when there is tissue heterogeneity. While standard intensity thresholds using a range of off-resonant frequencies was an adequate approach, there are more areas of field inhomogeneity in human participants. There is also the requirement of larger FOVs required for abdominal imaging. Phantom studies in this work mainly used FOVs of 16 - 20 cm, and the geometric accuracy was assessed up to 24 cm. Abdominal imaging in humans, however, typically requires larger FOVs, and gradient nonlinearities thus become more problematic. Readout oversampling in radial imaging can image larger FOVs with smaller aliasing patterns, but geometric accuracy and the co-RASOR signal effects should be studied in human participants. Additionally, human subjects also introduce motion into the acquired signals. Fully sampled radial acquisitions are more insensitive to motion, but undersampling reduces this effect. The benefit of undersampling exploits the density in the centre k-space locations, and reduced data collection in this region may begin to amplify the motion artifacts and cause more coherent noise patterns. This may limit the degree of undersampling, and thus the temporal efficiencies gained.

8.4 Contribution and Future Directions

To our knowledge, the use of dual-plane co-RASOR has not been previously applied to varied undersampling reconstructions, nor the multidimensional simulations that were performed. Furthermore, the use of the TGV2 penalty has not been studied in cases where highly localized signals are present. Although the co-RASOR sequence was first applied in 3D, and in dual-plane to LDR brachytherapy seeds, paramagnetic needles, and SPIO particles, the use of fiducial localization has not been reported. The simulated effect has been previously reported for a line phantom to highlight the capability to rewind hyperintensities. We further extended this to display images, which we feel is an important extension since there is a plane-dependent pattern of the observed signals, and contrast differs between acquired planes. A line phantom displays symmetric hyperintensities since the line through the field inhomogeneity is symmetric. However, this does not extend to two dimensions, where clear differences between point-symmetric and dipole patterns were observed.

In this work, we first attempted to use a single MR imaging sequence to differentiate gold fiducials from brachytherapy seeds. In centres performing MR-only simulation, the use of a single negative contrast sequence has not been adequate to perform this differentiation, and CT has been relied upon in an attempt to achieve this. Finally, to our knowledge we are the first to assess both the geometric accuracy and target registration error between dedicated MR sequences for positive contrast, and CT. Previous studies rely on calculating the registration error between the same set of points used for the registration, which have uncorrelated mean squared distance errors between CT and registered MR coordinates. We feel this choice enables us to use the information from the fiducial target registration error and use this as an

estimate of the fiducial localization error in a real world situation where implanted fiducials define the transformation, and the organs are the targets of interest.

Future directions should address imaging human subjects. Dedicated MR sequences to localize fiducials in vivo have been verified using CT, with true positive detection rates in the range of 38 - 77%. Combining parameters from multiple sequences can improve detection rates to 90%. Using prior template models and matching to the signal voids of acquired MR sequences further improve detection rates. These strategies rely on multiple finely tuned machine learning algorithms and/or multiple imaging sequences that require parameter optimization. We feel that a similar template model using positive contrast, as opposed to signal voids, based on the simulated framework in this thesis, could be incorporated in a similar manner. The benefit would be that both the acquired data and templates would display positive contrast natively, and be better suited to create masks of each fiducial.

Finally, in order to introduce such a sequence into MR-only simulation, retrospective analysis involving image guided tracking should be performed. A set of daily adjustments using cone beam CT or portal imaging can be compared to the nominal MR simulated scans, as well as the co-RASOR scans. In this manner, accuracy over the entire fraction length can be reported. Over a patient population, systematic and random errors may also be reported, aiding in defining potentially reduced CTV margins.

8.5 Concluding Statement

MR integrated simulation and therapy planning is steadily increasing due to the numerous benefits MR offers in cancer staging, and tissue contrast for defining organ

margins. Image guidance is also related to improved tumour control and lower toxicity, improving the quality of life after therapy. Still, the use of MR varies considerably between treatment sites. Several areas of improvement are actively being researched, and involve multidisciplinary techniques and expertise. It is our hope that the methods and results reported here can lead to better MR simulated images which may improve the registrations between simulated and daily images. Above all else, we hope that interest in this field continues to grow, as the potential for adaptive image guidance and MR-based LINACs may be the next generation for IGRT.

Appendix A

Summary of Publications and Software

A.1 Publications, Abstracts, and Conferences

Publications

1. (2017) Localizing Implanted Fiducial Markers using Undersampled co-RASOR MR Imaging. *Magnetic Resonance Imaging.* First Listed Author. Accepted: December 2017.

   Refereed?: Yes. Number of Contributors: 3

2. (2018) Differentiating Platinum Coated Brachytherapy Seeds and Gold Fiducial Markers using co-RASOR MRI. *Magnetic Resonance in Medicine* First Listed Author. Submitted: February 2018.

   Refereed?: Yes. Number of Contributors: 3

Conference Publications

1. (2018) Differentiating Brachytherapy Seeds and Gold Fiducial Markers using co-RASOR MRI. *International Society for Magnetic Resonance in Medicine (ISMRM).* First Listed Author. Paris, France.
   Refereed?: Yes. Number of Contributors: 3

2. (2016) Localizing Implanted Gold Fiducial Markers using Undersampled co-RASOR MR Imaging. *European Society for Magnetic Resonance in Medicine and Biology (ESMRMB).* First Listed Author. Vienna, Austria.
   Refereed?: Yes. Number of Contributors: 3

3. (2015) Localizing Implanted Gold Fiducial Markers using Phase of Echo Planar Imaging. *European Society for Magnetic Resonance in Medicine and Biology (ESMRMB).* First Listed Author. Toulouse, France.
   Refereed?: Yes. Number of Contributors: 3

4. (2012) Evaluation of Resting-State BOLD in Locally Advanced Breast Cancer. *European Society for Magnetic Resonance in Medicine and Biology (ESMRMB).* First Listed Author. Lisbon, Portugal.
   Refereed?: Yes. Number of Contributors: 3

National and International Presentations

1. (2017) Localizing Implanted Fiducial Markers using Undersampled co-RASOR MR Imaging. McMaster School of Biomedical Engineering Symposium 2017, Hamilton, Ontario, Canada.
   Main Audience: Knowledge User

2. (2016) Localizing Implanted Fiducial Markers using Undersampled co-RASOR MR Imaging. European Society of Magnetic Resonance in Biology and Medicine, 2016 Proceedings, Vienna, Austria.

   Main Audience: Knowledge User. Invited? Yes. Competitive? Yes

3. (2016) Localizing Implanted Fiducial Markers using co-RASOR MR Imaging with Total Variation (TV). Hamilton Radiology Research Day 2016, Hamilton, Ontario, Canada.

   Main Audience: Knowledge User. Invited? Yes. Competitive? Yes

4. (2016) Localizing Implanted Fiducial Markers using co-RASOR MR Imaging with Total Variation (TV). Imaging Network Ontario 2016, Toronto, Ontario, Canada.

   Main Audience: Knowledge User. Invited? Yes. Competitive? Yes

5. (2014) A Discussion of Image Co-Registration. McMaster Museum of History Workshop, Hamilton, Ontario, Canada.

   Main Audience: General Public. Invited? Yes

6. (2013) Localizing Implanted Gold Fiducial Markers using Phase of Echo Planar Imaging. European Society of Magnetic Resonance in Biology and Medicine, 2013 Proceedings, Toulouse, France.

   Main Audience: Knowledge User. Invited? Yes. Competitive? Yes

7. (2012) Evaluation of Resting-State BOLD in Locally Advanced Breast Cancer. European Society of Magnetic Resonance in Biology and Medicine, 2012 Proceedings, Lisbon, Portugal.

   Main Audience: Knowledge User. Invited? Yes. Competitive? Yes

8. (2012) Fat Suppression Techniques for BOLD imaging in Locally Advanced Breast Cancer. Hamilton Radiology Research Day 2012, Hamilton, Ontario, Canada.

   Main Audience: Knowledge User. Invited? Yes. Competitive? Yes

A.2 Software

The software repository PSD Tools (https://bitbucket.org/evanmcnabb/psd) was written entirely by this author in order to create a suite of tools that can simulate and reconstruct MR data. This is written Python (with some bindings to MATLAB). The repository contains a python package and a set of binary files:

```
"psd package" modules:
   bloch.py
   Module contains functions for implementing Bloch et al. 2011
   for correcting gradient timing mismatch, as well as reporting
   their measured values.

   corasor.py
   Module for Centre-Out Radial Acquisition using
   off-resonance reception

   filter.py
   Module contains functions for filtering kspace data and
   the temporal gradient-encoded signals

   kspace.py
   Module containing functions related to kspace trajectories
   and transforming MR gradients to their spatial frequency
```

```
   domain.

   psdio.py
   Module contains functions related to input and output

   recon.py
   Module contains functions for saving data to disk and
   calling the Image Reconstruction Toolkit (IRT) which
   needs to run in the MATLAB environment.

Binary Files:
usage: crsim.py generate [-h] [-s filename] [-c <num-coils>] [-e <echo-time>]
                         [-u <factor>] [-t <size>]
                         filename

positional arguments:
  filename              Image file with field inhomogeneity data.

optional arguments:
  -h, --help            show this help message and exit
  -s filename, --save filename
                        Save simulated fourier data
  -c <num-coils>, --coils <num-coils>
                        Number of receiver coils for simulation (default: 1)
  -e <echo-time>, --echo <echo-time>
                        Echo time in ms (default 0.0 ms)
  -u <factor>, --undersample <factor>
                        Integer undersampling factor (default: 1)
  -t <size>, --thickness <size>
```

```
                        Slice thickness in mm (default: 1.0 mm)


usage: rasor.py sweep [-h] [-o [filename]] [-p <plane>] [-l <freq-val>]
                      [-u <freq-val>] [-s <freq-val>] [-r] [-d]
                      pfile

positional arguments:
  pfile                 pfile to reconstruct

optional arguments:
  -h, --help            show this help message and exit
  -o [filename], --output [filename]
                        Output reconstructed image with optional filename
  -p <plane>, --plane <plane>
                        Reconstruction Plane (default: None)
  -l <freq-val>, --lower-frequency <freq-val>
                        Lower frequency boundary in Hz (default: -8000 Hz)
  -u <freq-val>, --upper-frequency <freq-val>
                        Upper frequency boundary in Hz (default: +8000 Hz)
  -s <freq-val>, --step-size <freq-val>
                        Step size in Hz (default: 100 Hz)
  -r, --rotate          Flag to rotate output image (default: false)
  -d, --dir             Flag to sweep from a directory intead of pfile


usage: rasor.py recon [-h] [-o [filename]] [-f <freq-val>] [-p <plane>]
                      [-m <method>] [-r]
                      pfile
```

```
positional arguments:
  pfile                 pfile to reconstruct

optional arguments:
  -h, --help            show this help message and exit
  -o [filename], --output [filename]
                        Output reconstructed image with optional filename
  -f <freq-val>, --frequency <freq-val>
                        Off-resonance recon frequency in Hz (default: 0 Hz)
  -p <plane>, --plane <plane>
                        Reconstruction Plane (default: None)
  -m <method>, --method <method>
                        Reconstruction Method (default: NUFFT)
  -r, --rotate          Flag to rotate output image (default: false)


usage: fiducial.py [-h] [-N <matrix-size>] [-s [filename]] [-z <num-slices>]
                   [-f <FOV in-plane>] [-x <susceptibility>] [-d <diameter>]
                   [-l <length>] [-t <FOV through-plane>] [-p <polar-angle>]
                   [-a <azimuth-angle>] [-o {axial,coronal}]

Simulate fiducial marker and field inhomogeneity.

optional arguments:
  -h, --help            show this help message and exit
  -N <matrix-size>, --size <matrix-size>
                        NxN matrix size (default: 256)
  -s [filename], --save [filename]
```

```
                        Save simulated data file
  -z <num-slices>, --slices <num-slices>
                        Number of slices (default: 64)
  -f <FOV in-plane>, --fov <FOV in-plane>
                        In-plane FOV in cm (default: 20)
  -x <susceptibility>, --chi <susceptibility>
                        susceptibility in ppm (default: 4)
  -d <diameter>, --diameter <diameter>
                        diameter of fiducial in mm (default: 1.0)
  -l <length>, --length <length>
                        length of fiducial in mm (default: 1.0)
  -t <FOV through-plane>, --through <FOV through-plane>
                        Through-plane FOV in cm (default: 20)
  -p <polar-angle>, --polar <polar-angle>
                        Polar angle of fiducial in degrees (default: 0)
  -a <azimuth-angle>, --azimuth <azimuth-angle>
                        Azimuth angle of fiducial in degrees (default: 0)
  -o {axial,coronal}, --orientation {axial,coronal}
                        Imaging Plane (default: axial)
```

Two other software repositories were used, though written by other authors, which are the Image Reconstruction Toolkit [103], and TGV toolkit [100], both written in MATLAB. Python/MATLAB bindings were developed and incorporated into both of these toolkits so they can communicate with the PSD Tools package to perform various image reconstructions.

Finally, the simulations performed by the binary crsim.py file contains some assumptions which should be addressed. First, the simulated data is performed via a

2D discrete radial Fourier Transform:

$$S[p,q] = \sum_{n=0}^{N-1}\sum_{m=0}^{N-1} \rho[n,m] e^{-j2(\zeta_x n + \zeta_y m)} \times e^{-j\gamma \Delta B_z[n,m](p\Delta t + T_E)} \tag{A.1}$$

$$\begin{cases} \zeta_x = \frac{\pi p}{N_k} \cos\left(2\pi q/N\right), & p = 0,\ ...,\ N-1 \\ \zeta_y = \frac{\pi p}{N_k} \sin\left(2\pi q/N\right) & q = 0,\ ...\ N-1 \end{cases} \tag{A.2}$$

The assumption here is that the discrete Fourier Transform is able to generate the k-space samples at radial locations based entirely on the simulated phantom and supplied field inhomogeneity. A more accurate method to generate k-space samples would be to simulate the Bloch Equations in Equation 2.6, which would take into account both the applied magnetic field pulses and the relaxation. This simulation neglects the relaxation, which will increase spatial resolution. A simple explanation for this is that relaxation modulates k-space samples by an exponentially decreasing time constant. In the image domain, this is the same as convolving the image by the IFT of the exponential, which is a Lorentzian function. The longer the signal takes to decay, the sharper the Fourier inverse Lorentzian function, and better image resolution.

Bibliography

[1] Maria A Schmidt and Geoffrey S Payne. Radiotherapy planning using MRI. *Phys. Med. Biol.*, 60(22):R323–R361, nov 2015.

[2] Statistics Canada. Canadian Cancer Statistics - Special topic: Pancreatic cancer. pages 1–114, 2017.

[3] L Kachuri, P De, L F Ellison, et al. Cancer incidence, mortality and survival trends in Canada, 1970-2007. *Chronic Dis. Inj. Can.*, 33(2):69–80, mar 2013.

[4] Robert K Nam and Laurence H Klotz. Does screening for prostate cancer reduce prostate cancer mortality? *Can. Urol. Assoc. J.*, 3(3):187–188, jun 2009.

[5] Maxwell V Meng, Gary D Grossfeld, Natalia Sadetsky, et al. Contemporary patterns of androgen deprivation therapy use for newly diagnosed prostate cancer. *Urology*, 60(3):7–11, sep 2002.

[6] Linda C. Harlan, Jeffrey Abrams, Joan L. Warren, et al. Adjuvant Therapy for Breast Cancer: Practice Patterns of Community Physicians. *J. Clin. Oncol.*, 20(7):1809–1817, apr 2002.

[7] A. Mariotto. Trends in Use of Adjuvant Multi-Agent Chemotherapy and Tamoxifen for Breast Cancer in the United States: 1975-1999. *CancerSpectrum Knowl. Environ.*, 94(21):1626–1634, nov 2002.

[8] Ivo G. Schoots, Neophytos Petrides, Francesco Giganti, et al. Magnetic Resonance Imaging in Active Surveillance of Prostate Cancer: A Systematic Review. *Eur. Urol.*, 67(4):627–636, apr 2015.

[9] Brenda K. Edwards, Martin L. Brown, Phyllis A. Wingo, et al. Annual Report to the Nation on the Status of Cancer, 1975 to 2002, Featuring Population-Based Trends in Cancer Treatment. *JNCI J. Natl. Cancer Inst.*, 97(19):1407–1427, oct 2005.

[10] K. E. Pengel, C. E. Loo, H. J. Teertstra, et al. The impact of preoperative MRI on breast-conserving surgery of invasive cancer: a comparative cohort study. *Breast Cancer Res. Treat.*, 116(1):161–169, jul 2009.

[11] Rick G. Pleijhuis, Maurits Graafland, Jakob de Vries, et al. Obtaining Adequate Surgical Margins in Breast-Conserving Therapy for Patients with Early-Stage Breast Cancer: Current Modalities and Future Directions. *Ann. Surg. Oncol.*, 16(10):2717–2730, oct 2009.

[12] Patrick A Kupelian, Jeffrey C Buchsbaum, Mohamed A Elshaikh, et al. Improvement in relapse-free survival throughout the PSA era in patients with localized prostate cancer treated with definitive radiotherapy: Year of treatment an independent predictor of outcome. *Int. J. Radiat. Oncol.*, 57(3):629–634, nov 2003.

[13] Rebecca Siegel, Carol DeSantis, Katherine Virgo, et al. Cancer treatment and survivorship statistics, 2012. *CA. Cancer J. Clin.*, 62(4):220–241, jul 2012.

[14] E. M. Horwitz and G. E. Hanks. External beam radiation therapy for prostate cancer. *CA. Cancer J. Clin.*, 50(6):349–375, nov 2000.

[15] Neil G. Burnet. Defining the tumour and target volumes for radiotherapy. *Cancer Imaging*, 4(2):153–161, 2004.

[16] Christopher Lim, Shawn C Malone, Leonard Avruch, et al. Magnetic resonance for radiotherapy management and treatment planning in prostatic carcinoma. *Br. J. Radiol.*, 88(1054):20150507, oct 2015.

[17] Mika Kapanen, Juhani Collan, Annette Beule, et al. Commissioning of MRI-only based treatment planning procedure for external beam radiotherapy of prostate. *Magn. Reson. Med.*, 70(1):127–135, jul 2013.

[18] Neelam Tyagi, Sandra Fontenla, Michael Zelefsky, et al. Clinical workflow for MR-only simulation and planning in prostate. *Radiat. Oncol.*, 12(1):119, dec 2017.

[19] Neelam Tyagi, Sandra Fontenla, Jing Zhang, et al. Dosimetric and workflow evaluation of first commercial synthetic CT software for clinical use in pelvis. *Phys. Med. Biol.*, 62(8):2961–2975, apr 2017.

[20] Mika Kapanen and Mikko Tenhunen. T1/T2*-weighted MRI provides clinically relevant pseudo-CT density data for the pelvic bones in MRI-only based radiotherapy treatment planning. *Acta Oncol. (Madr).*, 52(3):612–618, 2013.

[21] Jason A. Dowling, Jidi Sun, Peter Pichler, et al. Automatic Substitute Computed Tomography Generation and Contouring for Magnetic Resonance Imaging (MRI)-Alone External Beam Radiation Therapy From Standard MRI Sequences. *Int. J. Radiat. Oncol.*, 93(5):1144–1153, dec 2015.

[22] B. G. Fallone, B. Murray, S. Rathee, et al. First MR images obtained during megavoltage photon irradiation from a prototype integrated linac-MR system. *Med. Phys.*, 36(6Part1):2084–2088, may 2009.

[23] Sasa Mutic and James F. Dempsey. The ViewRay System Magnetic Resonance Guided and Controlled Radiotherapy. *Semin. Radiat. Oncol.*, 24(3):196–199, jul 2014.

[24] Jan J.W. Lagendijk, Bas W. Raaymakers, Alexander J.E. Raaijmakers, et al. MRI/linac integration. *Radiother. Oncol.*, 86(1):25–29, 2008.

[25] A L Boyer and C X Yu. Intensity modulated radiation therapy with dynamic multileaf collimators. *Semin. Radiat. Oncol.*, 9(1):48–59, jan 1999.

[26] Arthur Frazier, Maria Du, John Wong, et al. Dosimetric evaluation of the conformation of the multileaf collimator to irregularly shaped fields. *Int. J. Radiat. Oncol.*, 33(5):1229–1238, dec 1995.

[27] A. Taylor. Intensity modulated radiotherapy - what is it? *Cancer Imaging*, 4(2):68–73, 2004.

[28] John D. Fenwick, Wolfgang A. Tomé, Emilie T. Soisson, et al. Tomotherapy and Other Innovative IMRT Delivery Systems. *Semin. Radiat. Oncol.*, 16(4):199–208, oct 2006.

[29] Michael Baumann, Mechthild Krause, Jens Overgaard, et al. Radiation oncology in the era of precision medicine. *Nat. Rev. Cancer*, 16(4):234–49, 2016.

[30] Shin-ei Noda, Tim Lautenschlaeger, Michael R. Siedow, et al. Technological Advances in Radiation Oncology for Central Nervous System Tumors. *Semin. Radiat. Oncol.*, 19(3):179–186, jul 2009.

[31] Brian D. Kavanagh and Robert D. Timmerman. Stereotactic Radiosurgery and Stereotactic Body Radiation Therapy: An Overview of Technical Considerations and Clinical Applications. *Hematol. Oncol. Clin. North Am.*, 20(1):87–95, feb 2006.

[32] È Coste-Manière, D Olender, W Kilby, et al. Robotic whole body stereotactic radiosurgery: clinical advantages of the Cyberknife® integrated system. *Int. J. Med. Robot. Comput. Assist. Surg.*, 1(2):28–39, jan 2005.

[33] Martin J. Murphy. Fiducial-based targeting accuracy for external-beam radiotherapy. *Med. Phys.*, 29(3):334–344, feb 2002.

[34] Douglas J. Moseley, Elizabeth A. White, Kirsty L. Wiltshire, et al. Comparison of localization performance with implanted fiducial markers and cone-beam computed tomography for on-line image-guided radiotherapy of the prostate. *Int. J. Radiat. Oncol.*, 67(3):942–953, mar 2007.

[35] Walter G. Park, Brian M. Yan, Devin Schellenberg, et al. EUS-guided gold fiducial insertion for image-guided radiation therapy of pancreatic cancer: 50 successful cases without fluoroscopy. *Gastrointest. Endosc.*, 71(3):513–518, mar 2010.

[36] Nishita Kothary, Jeremy J. Heit, John D. Louie, et al. Safety and Efficacy of Percutaneous Fiducial Marker Implantation for Image-guided Radiation Therapy. *J. Vasc. Interv. Radiol.*, 20(2):235–239, feb 2009.

[37] Alexis N.T.J. Kotte, Pieter Hofman, Jan J.W. Lagendijk, et al. Intrafraction Motion of the Prostate During External-Beam Radiation Therapy: Analysis of 427 Patients with Implanted Fiducial Markers. *Int. J. Radiat. Oncol.*, 69(2):419–425, oct 2007.

[38] Daniel C. Schiffner, Alexander R. Gottschalk, Michael Lometti, et al. Daily electronic portal imaging of implanted gold seed fiducials in patients undergoing radiotherapy after radical prostatectomy. *Int. J. Radiat. Oncol.*, 67(2):610–619, feb 2007.

[39] Homan Dehnad, Aart J Nederveen, Uulke A van der Heide, et al. Clinical feasibility study for the use of implanted gold seeds in the prostate as reliable positioning markers during megavoltage irradiation. *Radiother. Oncol.*, 67(3):295–302, jun 2003.

[40] D.W. Eggert, A. Lorusso, and R.B. Fisher. Estimating 3-D rigid body transformations: a comparison of four major algorithms. *Mach. Vis. Appl.*, 9(5-6):272–290, mar 1997.

[41] Rakesh R. Patel and Douglas W. Arthur. The Emergence of Advanced Brachytherapy Techniques for Common Malignancies. *Hematol. Oncol. Clin. North Am.*, 20(1):97–118, feb 2006.

[42] A.L. Creak, A. Tree, and F. Saran. Radiotherapy Planning in High-grade

Gliomas: a Survey of Current UK Practice. *Clin. Oncol.*, 23(3):189–198, apr 2011.

[43] R. M. Mann, C. K. Kuhl, K. Kinkel, et al. Breast MRI: guidelines from the European Society of Breast Imaging. *Eur. Radiol.*, 18(7):1307–1318, jul 2008.

[44] Maciej Pech, Konrad Mohnike, Gero Wieners, et al. Radiotherapy of Liver Metastases. *Strahlentherapie und Onkol.*, 184(5):256–261, may 2008.

[45] Louise Dickinson, Hashim U. Ahmed, Clare Allen, et al. Magnetic Resonance Imaging for the Detection, Localisation, and Characterisation of Prostate Cancer: Recommendations from a European Consensus Meeting. *Eur. Urol.*, 59(4):477–494, apr 2011.

[46] Johannes C.A. Dimopoulos, Peter Petrow, Kari Tanderup, et al. Recommendations from Gynaecological (GYN) GEC-ESTRO Working Group (IV): Basic principles and parameters for MR imaging within the frame of image based adaptive cervix cancer brachytherapy. *Radiother. Oncol.*, 103(1):113–122, apr 2012.

[47] K Newbold, M Partridge, G Cook, et al. Advanced imaging applied to radiotherapy planning in head and neck cancer: a clinical review. *Br. J. Radiol.*, 79(943):554–561, jul 2006.

[48] Steven A. Bigler, Robert E. Deering, and Michael K. Brawer. Comparison of microscopic vascularity in benign and malignant prostate tissue. *Hum. Pathol.*, 24(2):220–226, feb 1993.

[49] Christiane Kuhl. The Current Status of Breast MR Imaging Part I. Choice of Technique, Image Interpretation, Diagnostic Accuracy, and Transfer to Clinical Practice. *Radiology*, 244(2):356–378, aug 2007.

[50] Sadhna Verma, Baris Turkbey, Naira Muradyan, et al. Overview of Dynamic Contrast-Enhanced MRI in Prostate Cancer Diagnosis and Management. *Am. J. Roentgenol.*, 198(6):1277–1288, jun 2012.

[51] EA Morris, CE Comstock, CH Lee, et al. *ACR BI-RADS Magnetic Resonance Imaging. In: ACR BI-RADS Atlas, Breast Imaging Reporting and Data System.* Reston, VA, American College of Radiology, 5 edition, 2013.

[52] E Henderson, B K Rutt, and T Y Lee. Temporal sampling requirements for the tracer kinetics modeling of breast disease. *Magn. Reson. Imaging*, 16(9):1057–73, nov 1998.

[53] C K Kuhl, P Mielcareck, S Klaschik, et al. Dynamic breast MR imaging: are signal intensity time course data useful for differential diagnosis of enhancing lesions? *Radiology*, 211(1):101–10, apr 1999.

[54] P S Tofts, G Brix, D L Buckley, et al. Estimating kinetic parameters from dynamic contrast-enhanced T(1)-weighted MRI of a diffusable tracer: standardized quantities and symbols. *J. Magn. Reson. Imaging*, 10(3):223–32, sep 1999.

[55] Elizabeth A Morris, Laura Liberman, Douglas J Ballon, et al. MRI of occult breast carcinoma in a high-risk population. *AJR. Am. J. Roentgenol.*, 181(3):619–26, sep 2003.

[56] A S N JACKSON, S A REINSBERG, S A SOHAIB, et al. Dynamic contrast-enhanced MRI for prostate cancer localization. *Br. J. Radiol.*, 82(974):148–156, feb 2009.

[57] Jurgen J. Fütterer, Stijn W. T. P. J. Heijmink, Tom W. J. Scheenen, et al. Prostate Cancer Localization with Dynamic Contrast-enhanced MR Imaging and Proton MR Spectroscopic Imaging. *Radiology*, 241(2):449–458, nov 2006.

[58] E. O. Stejskal and J. E. Tanner. Spin Diffusion Measurements: Spin Echoes in the Presence of a Time Dependent Field Gradient. *J. Chem. Phys.*, 42(1):288–292, jan 1965.

[59] MA Bernstein, KF King, and XJ Zhou. *Handbook of MRI Pulse Sequences*. Elsevier Inc., 2004.

[60] Thomas Hambrock, Diederik M. Somford, Henkjan J. Huisman, et al. Relationship between Apparent Diffusion Coefficients at 3.0-T MR Imaging and Gleason Grade in Peripheral Zone Prostate Cancer. *Radiology*, 259(2):453–461, may 2011.

[61] Baris Turkbey, Vijay P. Shah, Yuxi Pang, et al. Is Apparent Diffusion Coefficient Associated with Clinical Risk Scores for Prostate Cancers that Are Visible on 3-T MR Images? *Radiology*, 258(2):488–495, feb 2011.

[62] Bashar Zelhof, Martin Pickles, Gary Liney, et al. Correlation of diffusion-weighted magnetic resonance data with cellularity in prostate cancer. *BJU Int.*, 103(7):883–8, apr 2009.

[63] Alexey Surov, Hans Jonas Meyer, and Andreas Wienke. Correlation between apparent diffusion coefficient (ADC) and cellularity is different in several tumors: a meta-analysis. *Oncotarget*, 8(35), aug 2017.

[64] F. Bloch. Nuclear Induction. *Phys. Rev.*, 70(7-8):460–474, oct 1946.

[65] J.I. Jackson, C.H. Meyer, D.G. Nishimura, et al. Selection of a convolution function for Fourier inversion using gridding (computerised tomography application). *IEEE Trans. Med. Imaging*, 10(3):473–478, 1991.

[66] Katherine L. Wright, Jesse I. Hamilton, Mark A. Griswold, et al. Non-Cartesian parallel imaging reconstruction. *J. Magn. Reson. Imaging*, 40(5):1022–1040, nov 2014.

[67] RW Brown, YN Cheng, EM Haacke, et al. *Magnetic Resonance Imaging Physical Principles and Sequence Design*. 2 edition, 2014.

[68] Akihiro Tanimoto, Jun Nakashima, Hidaka Kohno, et al. Prostate cancer screening: The clinical value of diffusion-weighted imaging and dynamic MR imaging in combination with T2-weighted imaging. *J. Magn. Reson. Imaging*, 25(1):146–152, jan 2007.

[69] Kazuhiro Kitajima, Yasushi Kaji, Yoshitatsu Fukabori, et al. Prostate cancer detection with 3 T MRI: Comparison of diffusion-weighted imaging and dynamic contrast-enhanced MRI in combination with T2-weighted imaging. *J. Magn. Reson. Imaging*, 31(3):625–631, mar 2010.

[70] T. Yoshizako, A. Wada, T. Hayashi, et al. Usefulness of diffusion-weighted imaging and dynamic contrast-enhanced magnetic resonance imaging in the

diagnosis of prostate transition-zone cancer. *Acta radiol.*, 49(10):1207–1213, dec 2008.

[71] C Parker. Magnetic resonance imaging in the radiation treatment planning of localized prostate cancer using intra-prostatic fiducial markers for computed tomography co-registration. *Radiother. Oncol.*, 66(2):217–224, feb 2003.

[72] Peter L. Roberson, P. William McLaughlin, Vrinda Narayana, et al. Use and uncertainties of mutual information for computed tomography/magnetic resonance (CT/MR) registration post permanent implant of the prostate. *Med. Phys.*, 32(2):473–482, jan 2005.

[73] Tufve Nyholm, Morgan Nyberg, Magnus G Karlsson, et al. Systematisation of spatial uncertainties for comparison between a MR and a CT-based radiotherapy workflow for prostate treatments. *Radiat. Oncol.*, 4(1):54, 2009.

[74] D F Dubois, B R Prestidge, L A Hotchkiss, et al. Intraobserver and interobserver variability of MR imaging- and CT-derived prostate volumes after transperineal interstitial permanent prostate brachytherapy. *Radiology*, 207(3):785–789, jun 1998.

[75] M Debois, R Oyen, F Maes, et al. The contribution of magnetic resonance imaging to the three-dimensional treatment planning of localized prostate cancer. *Int. J. Radiat. Oncol. Biol. Phys.*, 45(4):857–65, nov 1999.

[76] J A Antolak and I I Rosen. Planning target volumes for radiotherapy: how much margin is needed? *Int. J. Radiat. Oncol. Biol. Phys.*, 44(5):1165–70, jul 1999.

[77] Marcel van Herk. Errors and margins in radiotherapy. *Semin. Radiat. Oncol.*, 14(1):52–64, jan 2004.

[78] Patrick A. Kupelian, Katja M. Langen, Twyla R. Willoughby, et al. Image-Guided Radiotherapy for Localized Prostate Cancer: Treating a Moving Target. *Semin. Radiat. Oncol.*, 18(1):58–66, jan 2008.

[79] Michael J. Zelefsky, Marisa Kollmeier, Brett Cox, et al. Improved Clinical Outcomes With High-Dose Image Guided Radiotherapy Compared With Non-IGRT for the Treatment of Clinically Localized Prostate Cancer. *Int. J. Radiat. Oncol.*, 84(1):125–129, sep 2012.

[80] Elisa Ålander, Harri Visapää, Mauri Kouri, et al. Gold seed fiducials in analysis of linear and rotational displacement of the prostate bed. *Radiother. Oncol.*, 110(2):256–260, feb 2014.

[81] Alan M. Nichol, Kristy K. Brock, Gina A. Lockwood, et al. A magnetic resonance imaging study of prostate deformation relative to implanted gold fiducial markers. *Int. J. Radiat. Oncol.*, 67(1):48–56, jan 2007.

[82] Matthew M Poggi, Dean A Gant, Wilfred Sewchand, et al. Marker seed migration in prostate localization. *Int. J. Radiat. Oncol.*, 56(5):1248–1251, 2003.

[83] Patrick A. Kupelian, Twyla R. Willoughby, Sanford L. Meeks, et al. Intraprostatic fiducials for localization of the prostate gland: Monitoring intermarker distances during radiation therapy to test for marker stability. *Int. J. Radiat. Oncol.*, 62(5):1291–1296, aug 2005.

[84] Gary P. Liney and Marinus A. Moerland. Magnetic Resonance Imaging Acquisition Techniques for Radiotherapy Planning. *Semin. Radiat. Oncol.*, 24(3):160–168, jul 2014.

[85] Soumya Ghose, Jhimli Mitra, David Rivest-Hénault, et al. MRI-alone radiation therapy planning for prostate cancer: Automatic fiducial marker detection. *Med. Phys.*, 43(5):2218–2228, apr 2016.

[86] Christian Gustafsson, Juha Korhonen, Emilia Persson, et al. Registration free automatic identification of gold fiducial markers in MRI target delineation images for prostate radiotherapy. *Med. Phys.*, 44(11):5563–5574, nov 2017.

[87] Matteo Maspero, Cornelis A T van den Berg, Frank Zijlstra, et al. Evaluation of an automatic MR-based gold fiducial marker localisation method for MR-only prostate radiotherapy. *Phys. Med. Biol.*, 62(20):7981–8002, oct 2017.

[88] Evert-jan P.A. Vonken, Michael Schär, Jing Yu, et al. Direct in vitro comparison of six three-dimensional positive contrast methods for susceptibility marker imaging. *J. Magn. Reson. Imaging*, 38(2):344–357, 2013.

[89] Peter R Seevinck, Hendrik de Leeuw, Clemens Bos, et al. Highly localized positive contrast of small paramagnetic objects using 3D center-out radial sampling with off-resonance reception. *Magn. Reson. Med.*, 65(1):146–56, 2011.

[90] H. De Leeuw, P. R. Seevinck, and C. J G Bakker. Center-out radial sampling with off-resonant reconstruction for efficient and accurate localization of punctate and elongated paramagnetic structures. *Magn. Reson. Med.*, 69(6):1611–1622, 2013.

[91] Jonathan Lambert, Peter B. Greer, Fred Menk, et al. MRI-guided prostate radiation therapy planning: Investigation of dosimetric accuracy of MRI-based dose planning. *Radiother. Oncol.*, 98(3):330–334, 2011.

[92] Jason A. Dowling, Jonathan Lambert, Joel Parker, et al. An Atlas-Based Electron Density Mapping Method for Magnetic Resonance Imaging (MRI)-Alone Treatment Planning and Adaptive MRI-Based Prostate Radiation Therapy. *Int. J. Radiat. Oncol.*, 83(1):e5–e11, 2012.

[93] P Metcalfe. The Potential for an Enhanced Role For MRI in Radiation-therapy Treatment Planning. *Technol. Cancer Res. Treat.*, 2013.

[94] Eric S. Paulson, Beth Erickson, Chris Schultz, et al. Comprehensive MRI simulation methodology using a dedicated MRI scanner in radiation oncology for external beam radiation treatment planning. *Med. Phys.*, 42(1):28–39, 2014.

[95] Jan-Henry Seppenwoolde, Max A. Viergever, and Chris J.G. Bakker. Passive tracking exploiting local signal conservation: The white marker phenomenon. *Magn. Reson. Med.*, 50(4):784–790, 2003.

[96] Hendrik de Leeuw, Marinus a Moerland, Marco van Vulpen, et al. A dual-plane co-RASOR technique for accurate and rapid tracking and position verification of an Ir-192 source for single fraction HDR brachytherapy. *Phys. Med. Biol.*, 58(21):7829–39, 2013.

[97] Klaus Scheffler and Jiirgen Hennig. Properties of the Polar Point Spread Function. *Magn. Reson. Med.*, 40(3):474–480, 1998.

[98] Kai Tobias Block, Martin Uecker, and Jens Frahm. Undersampled radial MRI with multiple coils. Iterative image reconstruction using a total variation constraint. *Magn. Reson. Med.*, 57(6):1086–98, 2007.

[99] Florian Knoll, Kristian Bredies, Thomas Pock, et al. Second order total generalized variation (TGV) for MRI. *Magn. Reson. Med.*, 65(2):480–491, 2011.

[100] Florian Knoll, Christian Clason, Kristian Bredies, et al. Parallel imaging with nonlinear reconstruction using variational penalties. *Magn. Reson. Med.*, 67(1):34–41, 2012.

[101] Peter M. Jakob, Mark A. Grisowld, Robert R. Edelman, et al. AUTO-SMASH: A self-calibrating technique for SMASH imaging. *Magma Magn. Reson. Mater. Physics, Biol. Med.*, 7(1):42–54, 1998.

[102] Mark A. Griswold, Peter M. Jakob, Robin M. Heidemann, et al. Generalized autocalibrating partially parallel acquisitions (GRAPPA). *Magn. Reson. Med.*, 47(6):1202–1210, 2002.

[103] Jeffrey A. Fessler and Bradley P. Sutton. Nonuniform fast Fourier transforms using min-max interpolation. *IEEE Trans. Signal Process.*, 51(2):560–574, 2003.

[104] K P Pruessmann, M Weiger, P Börnert, et al. Advances in sensitivity encoding with arbitrary k-space trajectories. *Magn. Reson. Med.*, 46(4):638–51, 2001.

[105] Olaf Dietrich, José G. Raya, Scott B. Reeder, et al. Measurement of signal-to-noise ratios in MR images: Influence of multichannel coils, parallel imaging, and reconstruction filters. *J. Magn. Reson. Imaging*, 26(2):375–385, 2007.

[106] Harold Levene. In Contributions to Probability and Statistics: Essays in Honor of Harold Hotelling, I. Olkin et al. eds. *Stanford Univ. Press*, pages 278–292, 1960.

[107] John F. Schenck. The role of magnetic susceptibility in magnetic resonance imaging: MRI magnetic compatibility of the first and second kinds. *Med. Phys.*, 23(6):815–850, 1996.

[108] Brian A. Hargreaves, Valentina Taviani, Daniel V. Litwiller, et al. 2d multi-spectral imaging for fast mri near metal. *Magnetic Resonance in Medicine*, 2017.

[109] P. R. Seevinck, H. De Leeuw, M. A. Moerland, et al. Fast and reliable localization of brachytherapy seeds using undersampled co-RASOR. *Proc. 19th Annu. Meet. Int. Soc. Magn. Reson. Med.*, 19, 2011.

[110] Clemens Diwoky, Daniel Liebmann, Bernhard Neumayer, et al. Positive contrast of SPIO-labeled cells by off-resonant reconstruction of 3D radial half-echo bSSFP. *NMR Biomed.*, pages 79–88, 2014.

[111] K P Pruessmann, M Weiger, M B Scheidegger, et al. SENSE: sensitivity encoding for fast MRI. *Magn. Reson. Med.*, 42(5):952–62, 1999.

[112] Felix A. Breuer, Stephan A.R. Kannengiesser, Martin Blaimer, et al. General formulation for quantitative G-factor calculation in GRAPPA reconstructions. *Magn. Reson. Med.*, 62(3):739–746, 2009.

[113] F Breuer, N Seiberlich, M Blaimer, et al. Quantitative g-factors for radial

GRAPPA. *Proc. 17th Sci. Meet. Int. Soc. Magn. Reson. Med.*, Honolulu:2712, 2009.

[114] Geert M. Villeirs, Koen Van Vaerenbergh, Luc Vakaet, et al. Interobserver Delineation Variation Using CT versus Combined CT and MRI in Intensity-Modulated Radiotherapy for Prostate Cancer. *Strahlentherapie und Onkol.*, 181(7):424–430, jul 2005.

[115] Joshua Kim, Carri Glide-Hurst, Anthony Doemer, et al. Implementation of a Novel Algorithm For Generating Synthetic CT Images From Magnetic Resonance Imaging Data Sets for Prostate Cancer Radiation Therapy. *Int. J. Radiat. Oncol.*, 91(1):39–47, jan 2015.

[116] Juha Korhonen, Mika Kapanen, Jani Keyriläinen, et al. A dual model HU conversion from MRI intensity values within and outside of bone segment for MRI-based radiotherapy treatment planning of prostate cancer. *Med. Phys.*, 41(1):011704, dec 2013.

[117] X. Artaechevarria, A. Munoz-Barrutia, and C. Ortiz-de Solorzano. Combination Strategies in Multi-Atlas Image Segmentation: Application to Brain MR Data. *IEEE Trans. Med. Imaging*, 28(8):1266–1277, aug 2009.

[118] M Mcjury, A O'Neill, M Lawson, et al. Assessing the image quality of pelvic MR images acquired with a flat couch for radiotherapy treatment planning. *Br. J. Radiol.*, 84(1004):750–755, aug 2011.

[119] Gopal Varma, Rachel E. Clough, Peter Acher, et al. Positive visualization

of implanted devices with susceptibility gradient mapping using the original resolution. *Magn. Reson. Med.*, 65(5):1483–1490, may 2011.

[120] Gopal Varma, Steen Fjord Pedersen, Matthias Taupitz, et al. Utilizing different methods for visualizing susceptibility from a single multi-gradient echo dataset. *Magn. Reson. Mater. Physics, Biol. Med.*, 22(5):297–308, oct 2009.

[121] S. Delangre, Q.L. Vuong, C. Po, et al. Improvement of the Off-Resonance Saturation, an MRI sequence for positive contrast with SPM particles: Theoretical and experimental study. *J. Magn. Reson.*, 265:99–107, apr 2016.

[122] Ying Dong, Zheng Chang, Guoxi Xie, et al. Susceptibility-based positive contrast MRI of brachytherapy seeds. *Magn. Reson. Med.*, 74(3):716–726, sep 2015.

[123] Frank Zijlstra, Marinus A. Moerland, Jochem R.N. van der Voort van Zyp, et al. Challenges in MR-only seed localization for postimplant dosimetry in permanent prostate brachytherapy. *Med. Phys.*, 44(10):5051–5060, oct 2017.

[124] Catarina Dinis Fernandes, Cuong V. Dinh, Marcel J. Steggerda, et al. Prostate fiducial marker detection with the use of multi-parametric magnetic resonance imaging. *Phys. Imaging Radiat. Oncol.*, 1:14–20, jan 2017.

[125] Joakim H. Jonsson, Anders Garpebring, Magnus G. Karlsson, et al. Internal Fiducial Markers and Susceptibility Effects in MRI-Simulation and Measurement of Spatial Accuracy. *Int. J. Radiat. Oncol.*, 82(5):1612–1618, apr 2012.

[126] Evan McNabb, Raimond Wong, and Michael D. Noseworthy. Localizing implanted fiducial markers using undersampled co-RASOR MR imaging. *Magn. Reson. Imaging*, 48:1–9, may 2018.

[127] Klaus Scheffler and Stefan Lehnhardt. Principles and applications of balanced SSFP techniques. *Eur. Radiol.*, 13(11):2409–2418, nov 2003.

[128] Marjory Jolicoeur, Marie-Lynn Racine, Isabelle Trop, et al. Localization of the surgical bed using supine magnetic resonance and computed tomography scan fusion for planification of breast interstitial brachytherapy. *Radiother. Oncol.*, 100(3):480–484, sep 2011.

[129] Marina Giezen, Erik Kouwenhoven, Astrid N. Scholten, et al. MRI- Versus CT-Based Volume Delineation of Lumpectomy Cavity in Supine Position in Breast-Conserving Therapy: An Exploratory Study. *Int. J. Radiat. Oncol.*, 82(4):1332–1340, mar 2012.

[130] Emile N.J.T. van Lin, Jurgen J. Fütterer, Stijn W.T.P.J. Heijmink, et al. IMRT boost dose planning on dominant intraprostatic lesions: Gold marker-based three-dimensional fusion of CT with dynamic contrast-enhanced and 1H-spectroscopic MRI. *Int. J. Radiat. Oncol.*, 65(1):291–303, may 2006.

[131] Anurag K Singh, Peter Guion, Nancy Sears-Crouse, et al. Simultaneous integrated boost of biopsy proven, MRI defined dominant intra-prostatic lesions to 95 Gray with IMRT: early results of a phase I NCI study. *Radiat. Oncol.*, 2(1):36, 2007.

[132] Valérie Fonteyne, Geert Villeirs, Bruno Speleers, et al. Intensity-Modulated Radiotherapy as Primary Therapy for Prostate Cancer: Report on Acute Toxicity After Dose Escalation With Simultaneous Integrated Boost to Intraprostatic Lesion. *Int. J. Radiat. Oncol.*, 72(3):799–807, nov 2008.

[133] Evert-jan P.A. Vonken, Michael Schär, and Matthias Stuber. Positive contrast visualization of nitinol devices using susceptibility gradient mapping. *Magn. Reson. Med.*, 60(3):588–594, sep 2008.

[134] Kirsten R. Henken, Peter R. Seevinck, Jenny Dankelman, et al. Manually controlled steerable needle for MRI-guided percutaneous interventions. *Med. Biol. Eng. Comput.*, 55(2):235–244, feb 2017.

[135] J. Michael Fitzpatrick. Fiducial registration error and target registration error are uncorrelated. page 726102, feb 2009.

[136] Nobuyuki Otsu. A Threshold Selection Method from Gray-Level Histograms. *IEEE Trans. Syst. Man. Cybern.*, 9(1):62–66, jan 1979.

[137] Deming Wang, Wendy Strugnell, Gary Cowin, et al. Geometric distortion in clinical MRI systems. *Magn. Reson. Imaging*, 22(9):1211–1221, nov 2004.

[138] Lesley N. Baldwin, Keith Wachowicz, Steven D. Thomas, et al. Characterization, prediction, and correction of geometric distortion in 3T MR images. *Med. Phys.*, 34(2):388–399, jan 2007.

[139] Oliver J. Gurney-Champion, Eelco Lens, Astrid van der Horst, et al. Visibility and artifacts of gold fiducial markers used for image guided radiation therapy of pancreatic cancer on MRI. *Med. Phys.*, 42(5):2638–2647, may 2015.

[140] Tze Yee Lim, Rajat J. Kudchadker, Jihong Wang, et al. Effect of pulse sequence parameter selection on signal strength in positive-contrast MRI markers for MRI-based prostate postimplant assessment. *Med. Phys.*, 43(7):4312–4322, jun 2016.

[141] Nicola Schieda, Leonard Avruch, Wael M. Shabana, et al. Multi-echo gradient recalled echo imaging of the pelvis for improved depiction of brachytherapy seeds and fiducial markers facilitating radiotherapy planning and treatment of prostatic carcinoma. *J. Magn. Reson. Imaging*, 41(3):715–720, mar 2015.

[142] Osamu Tanaka, Hisao Komeda, Takayoshi Iida, et al. Fiducial marker for prostate radiotherapy: comparison of 0.35- and 0.5-mm-diameter computed tomography and magnetic resonance images. *Radiol. Med.*, 122(3):204–207, mar 2017.

[143] Patrick W. McLaughlin, Vrinda Narayana, Marc Kessler, et al. The use of mutual information in registration of CT and MRI datasets post permanent implant. *Brachytherapy*, 3(2):61–70, jan 2004.